

MODELING AND SIMULATION OF THE BOILING CRISIS
WITHIN PWR AT CFD SCALE

LUC FAVRE

Improving the Modeling of Wall Boiling for Multiphase CFD Simulations

Paris, December 2022

test

ABSTRACT

To write!

PUBLICATIONS

Some ideas and figures have appeared previously in the following publications:

Put your publications from the thesis here. The packages `multibib` or `bibtopic` etc. can be used to handle multiple different bibliographies in your document.

*We have seen that computer programming is an art,
because it applies accumulated knowledge to the world,
because it requires skill and ingenuity, and especially
because it produces objects of beauty.*

— knuth:1974 [knuth:1974]

ACKNOWLEDGEMENTS

Put your acknowledgements here.

Many thanks to everybody who already sent me a postcard!

Regarding the typography and other help, many thanks go to Marco Kuhlmann, Philipp Lehman, Lothar Schlesier, Jim Young, Lorenzo Pantieri and Enrico Gregorio¹, Jörg Sommer, Joachim Köstler, Daniel Gottschlag, Denis Aydin, Paride Legovini, Steffen Prochnow, Nicolas Repp, Hinrich Harms, Roland Winkler, and the whole L^AT_EX-community for support, ideas and some great software.

Regarding LyX: The LyX port was initially done by Nicholas Mariette in March 2009 and continued by Ivo Pletikosić in 2011. Thank you very much for your work and the contributions to the original style.

¹ Members of GuIT (Gruppo Italiano Utilizzatori di T_EX e L^AT_EX)

CONTENTS

I	INTRODUCTION	1
II	MODELING AND SIMULATION OF BOILING FLOWS USING CFD	2
1	NEPTUNE_CFD CODE	3
1.1	The NEPTUNE_CFD code and physical modeling	3
1.1.1	Simulation framework	3
1.1.2	Governing equations for turbulent boiling bubbly flows	3
1.1.3	Interfacial transfers closure laws	4
1.1.4	Turbulence modeling	5
1.1.5	Wall boiling model	5
1.1.6	Wall function for dispersed boiling flows	6
2	DEBORA CASES	7
2.1	Boiling freon in a simple tube : DEBORA experiments	7
2.1.1	Description of the experiment	7
2.1.2	NEPTUNE_CFD simulations of DEBORA cases	8
2.1.3	Investigating the nucleation site density modeling N_{sit}	8
III	DEVELOPMENT OF A NEW WALL HEAT FLUX PARTITIONING MODEL	11
3	EXISTING HEAT FLUX PARTITIONING MODELS	12
3.1	Kurul & Podowski (1990)	12
3.2	Basu (2000)	13
3.2.1	Case 1 : Bubble sliding, $D_d < s$	14
3.2.2	Case 2 : Bubble coalescence without sliding, $D_d \geq s$	16
3.3	Gilman (2017)	16
3.4	Zhou (2020)	18
3.5	Closure Laws for Remaining Parameters	19
3.5.1	Nucleation Site Density : N_{sit}	19
3.5.2	Bubble Departure Frequency f , Growth Time t_g and Wait Time t_w	20
4	BOILING BUBBLE DYNAMICS	21
4.1	Force Balance Modeling	21
4.2	Establishment of the force balance for a bubble on a vertical wall	22
4.2.1	Bubble shape : Geometrical definitions	22
4.2.2	Buoyancy force	23
4.2.3	Contact Pressure force	24
4.2.4	Capillary force	24
4.2.5	Added Mass force of a growing bubble	24
4.2.6	Added Mass from Duhar <i>et al.</i>	28
4.2.7	Lift and drag forces	28
4.3	Force Balance Modeling	30
4.3.1	General Considerations	30
4.3.2	Buoyancy Force	31
4.3.3	Capillary Force	32
4.3.4	Contact Pressure Force	32
4.3.5	Drag and Lift Forces	32
4.3.6	Inertia Force	33
4.3.7	Force Balance Summary	36
4.3.8	Bubble Growth	36

4.3.9	Liquid Velocity	37
4.4	Departure by Sliding	38
4.4.1	Non-Dimensional Analysis	38
4.4.2	Application to Experimental Data	39
4.4.3	Departure Diameter Prediction	42
4.4.4	Discussion and accounting for parameters uncertainties	44
4.5	Sliding phase	47
4.5.1	Modeling	47
4.5.2	Low Pressure Sliding	47
4.5.3	High Pressure Sliding	48
4.6	Conclusion	48
5	ASSEMBLING OF A NEW HEAT FLUX PARTITIONING MODEL	53
5.1	New model	53
5.2	General description of the model	53
5.2.1	Convective heat fluxes	54
5.2.2	Boiling heat flux	54
5.2.3	Quenching heat flux	54
5.2.4	Needed closure relationships	54
5.2.5	Single Bubble Quenching Area	55
5.2.6	Bubble Growth Time	55
5.2.7	Bubble Wait Time	55
5.2.8	Nucleation Site Density	55
5.2.9	Considerations on bubble interaction and nucleation sites deactivation	55
5.2.10	Nucleation Sites and Bubbles Interactions	57
IV	TOWARDS THE INDUSTRIAL GEOMETRY	60
6	PROMOTEUR	61
6.1	Boiling freon in a tube with mixing vanes : DEBORA-Promoteur experiments	61
6.1.1	Description of the experiment	61
6.1.2	NEPTUNE_CFD simulations of DEBORA-Promoteur cases	62
6.2	Liquid water flow in a tube with mixing vanes : AGATE-PROMOTEUR experiment	62
6.2.1	Description of the experiment	63
6.2.2	NEPTUNE_CFD simulations of AGATE-Promoteur case	63
V	CONCLUSION	65
VI	APPENDIX	66
A	DETAILS ON THE BUBBLE FORCE BALANCE	67
A.1	Appendix Section Test	68
A.2	Another Appendix Section Test	68
BIBLIOGRAPHY		70

LIST OF FIGURES

Figure 2.1 NCFD (lines) vs. Exp. (circles) - T_L and T_w - Cases C8G2P26W16Te44.9, Te49.6, Te66.6 and Te70.3 - Simulations using two meshes M1 (coarse) and M2 (fine).	8
Figure 2.2 NCFD (lines) vs. Exp. (circles) - α , d_G and $U_{G,z}$ - Cases C30G2P26W16Te66.6 and Te70.6 - Simulations using two meshes M1 (coarse) and M2 (fine).	9
Figure 2.3 N_{sit} correlations of Lemmert & Chawla (left) and Hibiki & Ishii (right) vs. exp. data from literature. Operation pressures are displayed. $\pm 50\%$ error bars are drawn in black.	9
Figure 2.4 NCFD results for α , T_L and T_w using Lemmert & Chawla and Hibiki & Ishii correlation. Cases 8G2P26W23Te66.6 and Te70.3, 30G2P26W23Te66.6 and 70.6.	10
Figure 3.1 Sketch of the heat transfers zones considered by Basu <i>et al.</i> . (Adapted from [Basu2005])	14
Figure 3.2 Sliding bubble behavior considered by Basu <i>et al.</i> . (Adapted from [Basu2005])	15
Figure 4.1 Sketch of the supposed bubble shape with (right) and without inclination (left).	22
Figure 4.2 Representation of the shape functions	23
Figure 4.3 Sketch of the forces applied to the bubble facing an upward flow \bar{U}_L and sliding at velocity \bar{U}_b	31
Figure 4.4 Drag correction from Shi <i>et al.</i> [shi_drag_2021].	34
Figure 4.5 Dominance map regarding departure by sliding. Boundaries plotted for water at 1 bar and $D_d = 0.5\text{mm}$. ($K = 2$)	39
Figure 4.6 Examples of qualitative analysis using the non-dimensional regime map	40
Figure 4.7 Dominance maps for each water data sets from Table 4.3.	42
Figure 4.8 Predicted bubble departure diameters	45
Figure 4.9 Initially assumed, real and reassessed bubble shape for Sugrue cases (picture adapted from [sugrue_experimental_2014]).	46
Figure 4.10 Proposed model performance while accounting for contact angle uncertainties	46
Figure 4.11 Bubble sliding velocity predictions on Maity cases	49
Figure 4.12 Bubble sliding length predictions on Kossolapov cases - $P = 20\text{ bar}$	50
Figure 4.13 Bubble sliding length predictions on Kossolapov cases - $P = 40\text{ bar}$	51
Figure 5.1 Sketch of the considered HFP A terminer, je dois ajouter des flèches pour indiquer les flux !	53
Figure 5.2 Model from Lemmert & Chawla	56
Figure 5.3 Model from Hibiki & Ishii	56
Figure 5.4 Model from Li <i>et al.</i>	56
Figure 5.5 Model from Zhou <i>et al.</i>	56
Figure 6.1 Picture of the mixing device (left) and its fine meshing (right).	61
Figure 6.2 NCFD (lines) vs. Exp. (circles) - α profiles for two MV positions ($23.5D_h$ in blue, $10D_h$ in orange) - $T_{in} = 65^\circ\text{C}$ (left), $T_{in} = 69^\circ\text{C}$ (middle), $T_{in} = 75^\circ\text{C}$ (right) - Simulations using two meshes M1 (coarse) and M2 (fine) for $T_{in} = 69^\circ\text{C}$	62
Figure 6.3 NCFD vs. Exp. - Top & Middle : Radial velocity and turbulent RMS ($z = 30\text{mm}$ & $z = 440\text{mm}$) - Bottom : Axial velocity and turbulent RMS ($z = 440\text{mm}$).	63

LIST OF TABLES

Table 2.1	Water/R12 scaling (from Garnier <i>et al.</i> [Garnier2001], $D_h = 19.2\text{mm}$ for We)	7
Table 4.1	Variables used by Shi <i>et al.</i>	29
Table 4.2	Summary of different force-balance mechanistic approaches.	36
Table 4.3	Bubble departure diameters data sets in vertical flow boiling	41
Table 4.4	Average relative error reached by the models.	47
Table A.1	Autem usu id	69

LISTINGS

NOMENCLATURE

Acronyms

BC	Boiling Crisis
CHF	Critical Heat Flux
DNS	Direct Numerical Simulations
HFP	Heat Flux Partitioning
PWR	Pressurized Water Reactor
RPE	Rayleigh-Plesset Equation
SMR	Small Modular Reactor

Greek symbols

η	Thermal diffusivity [m ² /s]
γ	Shear rate [s ⁻¹]
λ	Thermal conductivity [W/m/K]
μ	Dynamic viscosity [J.s/m ⁻³]
ν	Kinematic viscosity [m ² /s]
ϕ	Heat flux [J/m ² /s]
ρ	Density [kg/m ³]
σ	Surface tension [J/m ²]
$\theta, d\theta$	Contact angle and half-hysteresis [° or rad]
θ_i	Bubble inclination angle [° or rad]

Latin symbols

C	Force coefficient [-]
D	Bubble diameter [m]
D_h	Hydraulic diameter [m]
E	Kinetic energy [J]
F	Force [N]
G	Mass flux [kg/m ² /s]
g	Gravity acceleration [m ² /s]
h_{LV}	Latent heat of vaporization [J/kg]
K	Bubble growth constant [-]

$L_c = \sqrt{\frac{\sigma}{(\rho_L - \rho_V)g}}$	Capillary length [m]
l_{sl}	Bubble sliding length [m]
R	Bubble radius [m]
R_c	Bubble curvature radius [m]
r_w	Bubble foot radius [m]
T	Temperature [K]
U	Velocity [m/s]
U_τ	Wall friction velocity [m/s]
$U_{rel} = U_L - U_b$	Relative velocity [m/s]
V	Volume [m^3]

Non-dimensional numbers

$\text{Ca} = \frac{\mu_L U_L}{\sigma}$	Capillary number [-]
$\text{Eo} = \frac{(\rho_L - \rho_V) g R^2}{\sigma}$	Eotvos number [-]
$\text{Fr} = \frac{\rho_L U_L^2}{(\rho_L - \rho_V) g R}$	Froude number [-]
$\text{Ja} = \frac{\rho_L c_{P,L} T - T_{sat} }{\rho_V h_{LV}}$	Jakob number [-]
$\text{Pr} = \frac{\nu}{\eta}$	Prandtl number [-]
$\text{Re}_b = \frac{U_{rel} D_b}{\nu_L}$	Bubble Reynolds number [-]
$\text{Re}_{D_h} = \frac{G_L D_h}{\mu_L}$	Liquid bulk Reynolds number [-]
$\text{Sr} = \frac{2\gamma R}{ U_{rel} }$	Non-dimensional shear rate [-]
$y^+ = \frac{y U_\tau}{\nu_L}$	Non-dimensional wall distance [-]

Subscripts

AM	Added-Mass
b	Bubble
D	Drag
d	Departure or Downstream
L	Lift
L	Liquid
lo	Lift-off

<i>sat</i>	Saturation
<i>u</i>	upstream
<i>V</i>	Vapor
<i>w</i>	Wall

ACRONYMS

CFD	Computational Fluid Dynamics
CMFD	Computational Multi-Fluid Dynamics
NCFD	NEPTUNE_CFD
DNS	Direct Numerical Simulation
NSD	Nucleation Site Density

NOMENCLATURE

$N_{sit,0}$ Nucleation Site Density computed by correlation [m⁻²]

Part I
INTRODUCTION

Part II

MODELING AND SIMULATION OF BOILING FLOWS USING CFD

I

NEPTUNE_CFD CODE

1.1 THE NEPTUNE_CFD CODE AND PHYSICAL MODELING

1.1.1 *Simulation framework*

NEPTUNE_CFD is an eulerian multiphase CFD solver co-developed by EDF, CEA, IRSN and Framatome mostly for nuclear reactor applications. The code consists of a local three-dimensional modeling based on a two-fluid one pressure approach combined with mass, momentum and energy conservation equations for each phase[**Guelfi2007**].

The constitutive equations are solved using a pressure correction, and is based on a finite-volume discretization along with a collocated arrangement of the variables. Moreover, NEPTUNE_CFD allows the use of all type of meshes (hexahedra, tetrahedra, pyramids, etc.), even non-conforming ones, thanks to its face-based data structure. Finally, the code is well-suited for parallel computing, widening its computing capacity to very large meshes.

1.1.2 *Governing equations for turbulent boiling bubbly flows*

To simulate two-phase dispersed boiling flows, NEPTUNE_CFD solves the ensemble-averaged equations of mass conservation, momentum balance and energy conservation for each phase (total of 6 equations) :

Mass conservation :

$$\frac{\partial \alpha_k \rho_k}{\partial t} + \bar{\nabla} \cdot (\alpha_k \rho_k \bar{U}_k) = \Gamma_k \quad (1.1)$$

Where α_k , ρ_k , \bar{U}_k are the time fraction, average density and velocity of phase k ; $\Gamma_k = \Gamma_{k,i} + \Gamma_{k,w}$ the interfacial mass transfer term per unit of volume and time splitted between bulk and wall contribution. Subscripts $k = L$ or G denotes the liquid or gas phase, i the interfacial quantities and w the wall contribution.

Momentum balance :

$$\frac{\partial \alpha_k \rho_k \bar{U}_k}{\partial t} + \bar{\nabla} \cdot (\alpha_k \rho_k \bar{U}_k \otimes \bar{U}_k) = -\alpha_k \bar{\nabla} (P) + \bar{F}_{k,i} + \Gamma_k \bar{U}_{k,i} + \alpha_k \rho_k \bar{g} + \bar{\nabla} \cdot (\alpha_k (\bar{\tau}_{k,m} + \bar{\tau}_{k,T})) \quad (1.2)$$

Where P is the pressure, \bar{g} the gravity, $\bar{F}_{k,i}$ the interfacial forces accounting for momentum transfer between phases per unit of volume and time, $\bar{U}_{k,i}$ the interfacial velocity, $\bar{\tau}_{k,m}$ and $\bar{\tau}_{k,T}$ respectively the viscous and turbulent (or Reynolds) stress tensor. Subscript m and T respectively denote the molecular (or laminar) and turbulent terms.

Energy conservation :

$$\begin{aligned} \frac{\partial \alpha_k \rho_k H_k}{\partial t} + \bar{\nabla} \cdot (\alpha_k \rho_k H_k \bar{U}_k) = & \frac{\partial \alpha_k P}{\partial t} + \Gamma_k H_{k,i} + \bar{F}_{k,i} \cdot \bar{U}_k + Q_{k,I} + \bar{\nabla} \cdot (\alpha_k (\bar{\tau}_k + \bar{\tau}_{k,T}) \cdot \bar{U}_k) \\ & + \bar{\nabla} \cdot (\alpha_k (-(\lambda_{k,m} + \lambda_{k,T}) \bar{\nabla} (T_k))) + \alpha_k \rho_k \bar{g} \cdot \bar{U}_k + Q_{k,w} \end{aligned} \quad (1.3)$$

Where $H_k = e_k + \frac{U_k^2}{2} + \frac{P}{\rho_k} = h_k + \frac{U_k^2}{2}$ is the total enthalpy of phase k , $H_{k,i}$ the interfacial-averaged enthalpy, $Q_{k,i}$ the interfacial heat flux per unit of volume and time, $\lambda_{k,m}$ and $\lambda_{k,T}$ respectively being

the laminar and turbulent thermal conductivity, T_k the temperature, $Q_{k,w}$ the heat flux from the wall to phase k per unit of volume and time.

However, this ensemble-average approach requires a given number of closure laws since this operation removes most of the information about smaller scales physics such as interfacial exchanges between phases or wall-fluid interaction. Terms for which this modeling effort is needed are colored in orange in equations 1.1, 1.2 and 1.3. The chosen expressions for those terms are detailed in subsections 1.1.3, 1.1.4 and 1.1.5.

1.1.3 Interfacial transfers closure laws

The interfacial transfers of mass, momentum and energy are respectively noted in equations 1.1, 1.2 and 1.3 : Γ_k , $\overline{F_{k,i}}$ and $Q_{k,i}$.

Heat and mass transfers :

The mass transfer term, can be written as : $\Gamma_{L,i} + \Gamma_{G,i} = 0$, $\Gamma_{L,w} + \Gamma_{G,w} = 0$ with $\Gamma_{G,w} \geq 0$ in the case of boiling flows. This finally gives $\Gamma_L = -\Gamma_G$.

The interfacial heat flux $Q_{k,i}$ can be rewritten in terms of interfacial area concentration a_i : $Q_{k,i} = q''_{k,i} a_i$. Neglecting the mechanical contribution compared to the thermal terms, the energy jump condition can then be expressed as :

$$\sum_{k=L,G} \left(\Gamma_{k,i} h_{k,i} + q''_{k,i} a_i \right) = 0 \quad (1.4)$$

The estimation of $h_{k,i}$ is not straightforward since it can either be supposed to be the saturation enthalpy of phase k at the system pressure (H1) or $h_{k,i}$ can be identified to the phase-averaged enthalpy (H2). In NEPTUNE_CFD, the assumption H2 is chosen, thus giving the bulk condensation rate :

$$\Gamma_{L,i} = \frac{a_i (q''_{L,i} + q''_{G,i})}{h_{G,sat} - h_{L,sat}} \quad (1.5)$$

The interfacial heat flux densities $q''_{k,i}$ and interfacial area concentration a_i are expressed as $q''_{k,i} = C_{k,i} (T_{sat}(P) - T_k)$ and $a_i = 6\alpha_G/d_G$, d_G being the gas phase Sauter mean bubble diameter. The interfacial area is computed using the transport equation of RUYER & SEILER [Ruyer2009].

For subcooled liquid, the following heat transfer coefficient is used [Manon2000]:

$$C_{L,i} = \frac{Nu_L \lambda_L}{d_G} \text{ and } Nu_L = 2 + 0.6 Re^{1/2} Pr_L^{1/3} \quad (1.6)$$

Where Re is the bubble Reynolds number $Re = ||\overline{U_G} - \overline{U_L}|| d_G / \nu_L$ and Pr_L the liquid Prandtl number $Pr_L = \nu_L / \eta_L$ with ν_L and η_L respectively being the liquid kinematic viscosity and thermal diffusivity. On the other hand, if the liquid is overheated, the maximum of three heat transfer coefficients accounting for different heat tranfer mechanisms is taken [Berne1983]:

$$C_{L,i} = \max (C_{L,i,1}; C_{L,i,2}; C_{L,i,3}) \quad (1.7)$$

With $C_{L,i,n} = \lambda_L Nu_{L,n} / d_G$ and :

$$Nu_1 = \sqrt{\frac{4}{\pi} Pe} ; Nu_2 = 2 ; Nu_3 = \frac{12}{\pi} Ja \quad (1.8)$$

where $Pe = ||\overline{U_G} - \overline{U_L}|| d_G / \eta_L$ is the Peclet number and $Ja = \rho_L c_{p,L} |T_{sat} - T_L| / (\rho_g h_{lg})$ the Jakob number, with h_{lg} the latent heat of vaporization. Those three Nusselt numbers respectively correspond to convection heat transfer, stationnary conduction and transient conduction.

For the gas phase, a simple law that ensures that the vapor temperature remains close to the saturation temperature is used (which is expected for small bubbles, e. g. in a PWR) :

$$C_{G,i} a_i = \frac{\alpha_G \rho_v c_{p,G}}{t_c} \quad (1.9)$$

where $c_{p,G}$ is the gas heat capacity at constant pressure, and t_c a characteristic (relaxation) time given by the user (default value being $t_c = 0.01\text{s}$) .

Interfacial forces :

The interfacial momentum transfer (excluding transfer associated to transfer of mass Γ_k) is assumed to be composed of 4 different forces being the, drag D , the added mass AM , the lift L and the turbulent dispersion TD :

$$\overline{F_{k,i}} = \overline{F_{k,D}} + \overline{F_{k,AM}} + \overline{F_{k,L}} + \overline{F_{k,TD}} \quad (1.10)$$

The turbulent dispersion force $\overline{F_{k,TD}}$ originates from the averaging operation conducted on the three other forces' expressions, detailed in equations 1.11, 1.12, 1.13 and 1.14.

$$\overline{F_{G,D}} = -\overline{F_{L,D}} = -\frac{1}{8}a_i\rho_L C_D \left| \left| \overline{U_G} - \overline{U_L} \right| \right| (\overline{U_G} - \overline{U_L}) \quad (1.11)$$

$$\begin{aligned} \overline{F_{G,AM}} = -\overline{F_{L,AM}} &= -C_{AM} \frac{1+2\alpha_G}{1-\alpha_G} \alpha_G \rho_L \\ &\times \left[\left(\frac{\partial \overline{U_G}}{\partial t} + \bar{\nabla}(\overline{U_G}) \cdot \overline{U_G} \right) - \left(\frac{\partial \overline{U_L}}{\partial t} + \bar{\nabla}(\overline{U_L}) \cdot \overline{U_L} \right) \right] \end{aligned} \quad (1.12)$$

$$\overline{F_{G,L}} = -\overline{F_{L,L}} = -C_L \alpha_G \rho_L (\overline{U_G} - \overline{U_L}) \wedge (\bar{\nabla} \wedge \overline{U_L}) \quad (1.13)$$

$$\overline{F_{G,TD}} = -\overline{F_{L,TD}} = -\frac{2}{3}\alpha_L \alpha_G C_{TD} \bar{\nabla}(\alpha_G) \quad (1.14)$$

with C_D , C_{AM} , C_L and C_{TD} the associated forces coefficients, respectively taken from ISHII [**Ishii1967**], ZUBER [**Zuber1964**], TOMIYAMA [**Tomiyama2002**] and the Generalized Turbulent Dispersion model (GTD) from LAVIEVILLE *et al.* [**Lavieville2017**].

1.1.4 *Turbulence modeling*

For bubbly flow simulations, only liquid phase turbulence is taken into account. The prescribed model is the Reynolds Stress Model (RSM) $R_{ij} - \varepsilon SSG$ from SPEZIALE, SARKAR and GATSKI [**Speziale1991**] adapted to two-phase boiling flows by MIMOUNI *et al.* [**Mimouni2011**].

1.1.5 *Wall boiling model*

The modeling of the heterogeneous boiling phenomenon at the wall is based on a Heat Flux Partitioning (HFP) model, inspired by KURUL & PODOWSKI original work [**Kurul1990**] who divided the wall heat flux density ϕ_w in three terms :

- A single phase convective heat flux $\phi_{c,L}$ heating the liquid through the fraction of the wall area unaffected by the vapor bubbles
- A vaporization heat flux ϕ_e which accounts for the generation of vapor through heterogeneous nucleation
- A quenching heat flux ϕ_q to represent the thermal impact of bubbles departing from the wall and being replaced by cool liquid

A fourth flux is added to this HFP in NEPTUNE_CFD, following MIMOUNI *et al.* [**Mimouni2016**] who consider a convective heat flux heating the vapour $\phi_{c,G}$ when the wall area is covered by a dense accumulation of bubbles.

The model thus gives Equation 5.1 :

$$\phi_w = \phi_{c,L} + \phi_e + \phi_q + \phi_{c,G} \quad (1.15)$$

The convective heat fluxes are expressed as $\phi_{c,k} = A_k h_{k,log} (T_w - T_k)$ with $h_{k,log} = \rho_k c_{p,k} u^* / T_L^+$; where A_k the fraction of the wall area facing phase k , T_w the wall temperature and $h_{k,log}$ the wall logarithmic convective heat transfer coefficient to phase k based on the wall functions for friction velocity u^* and non-dimensional liquid temperature T_L^+ described in 1.1.6.

The vaporization heat flux is computed following $\phi_e = N_{sit} f \rho_G h_{lg} \pi d_d^2 / 6$ with :

- N_{sit} the nucleation site density modeled as [Lemmert1977] : $N_{sit} = [210 (T_w - T_{sat})]^{1.8}$
- f the bubble detachment frequency expressed as [Cole1960] : $f = \sqrt{\frac{4}{3} \frac{g |\rho_v - \rho_l|}{\rho_l d_d}}$
- d_d the bubble detachment diameter given by Unal correlation[Unal1976] corrected by Borée *et al.* [ref] (Equation 1.16)

$$d_d = 2.42 \times 10^{-5} P^{0.709} \frac{a}{\sqrt{b\varphi}} \text{ with } a = \frac{(T_w - T_{sat}) \lambda_w}{2\rho_G h_{lg} \sqrt{\pi \eta_w}} \text{ and } b = \begin{cases} \frac{T_{sat} - T_L}{2(1 - \rho_G/\rho_L)}, & \text{if } St \leq 0.0065 \\ \frac{1}{2(1 - \rho_G/\rho_L)} \frac{\phi_{c,L} + \phi_e + \phi_q}{0.0065 \rho_L c_{p,L} ||\bar{U}_L||}, & \text{if } St > 0.0065 \end{cases} \quad (1.16)$$

where λ_w and η_w are the wall thermal conductivity and diffusivity, $St = \frac{\phi_{c,L} + \phi_e + \phi_q}{\rho_L c_{p,L} ||\bar{U}_L|| (T_{sat} - T_L)}$ is the Stanton number and $\varphi = \max \left(1; \left(\frac{||\bar{U}_L||}{U_0} \right)^{0.47} \right)$ with $U_0 = 0.61 \text{ m/s}$

Finally, the quenching heat flux follows the approach of DEL VALLE & KENNING[DelValle1985] supposing that it follows a semi-infinite transient conduction regime : $\phi_q = A_G t_q f \frac{2\lambda_L (T_w - T_L)}{\sqrt{\pi \eta_L t_q}}$ where t_q is the quenching time, supposed to be equal to $1/f$.

1.1.6 Wall function for dispersed boiling flows

In boiling flows, the formation of bubbles at the wall may disturb the liquid velocity profile in the boundary layer. To take this phenomena into account, MIMOUNI *et al.* [Mimouni2016] proposed a wall function for boiling flows which tends to the single-phase formulation when $\alpha_G \rightarrow 0$ and depends on the bubble diameter and density at the wall :

$$u^+ = \frac{1}{\kappa} \ln(y^+) + B - \Delta u^+ \text{ with } \Delta u^+ = \begin{cases} 0 & \text{if } k_r^+ \leq 11.3 \\ \frac{1}{\kappa} \ln(1 + C_{kr} k_r^+) & \text{if } k_r^+ > 11.3 \end{cases} \quad (1.17)$$

where $\kappa=0.41$ is the Von Karman constant, $B = 5.3$ the standard single-phase logarithmic law constant. Δu^+ represents the offset of u^+ due to the wall roughness induced by the presence of bubble. We have $C_{kr} = 0.5$ and $k_r = \frac{k_r \sqrt{u^* u_T}}{\nu_L}$ the "roughness Reynolds number" with $u_T = C_\mu^{1/4} \sqrt{k_L}$ defined from the $k - \varepsilon$ constant $C_\mu = 0.09$ and k_L the liquid turbulent kinetic energy. Finally, $k_r = \alpha_G d_G$.

The non-dimensional wall liquid temperature T_L^+ is modeled according to LEDUC[Leduc1995]:

$$T_L^+ = \begin{cases} Pr_L y^+, & \text{if } y^+ \leq 13.2 \\ 8.67 Pr_{L,T} \left(\frac{Pr_L}{Pr_{L,T}} - 1 \right) \left(\frac{Pr_{L,T}}{Pr_L} \right)^{0.25} + \frac{Pr_{L,T}}{\kappa} \ln(E y^+) & \text{if } y^+ > 13.2 \end{cases} \quad (1.18)$$

With $Pr_{L,T} = 0.9$ the turbulent liquid Prandtl number, and $E = 7.76$ a constant for smooth walls.

2

DEBORA CASES

2.1 BOILING FREON IN A SIMPLE TUBE : DEBORA EXPERIMENTS

In this section, we simulate upward boiling flows of R12 in a vertical tube and compare the NEP-TUNE_CFD (NCFD) results with experimental measurements conducted by CEA & EDF on the DEBORA test facility.

2.1.1 Description of the experiment

In the end of 1990's, CEA and EDF built a test facility called DEBORA which goal was to conduct series of experiments and measurements to establish a database for boiling flows of freon R12. The choice of freon is justified because of its use as a simulating fluid for water in PWR conditions (very close phase density ratio, Weber number We, Boiling number Bo and thermodynamic flow quality x_{eq}). Table 2.1 sums up the flow conditions scaling between R12 and water.

Table 2.1: Water/R12 scaling (from Garnier *et al.* [Garnier2001], $D_h = 19.2\text{mm}$ for We)

Fluid	Water	Freon R12
Pressure P (bar)	100 - 180	14 - 30
Mass velocity G ($\text{kg}/\text{m}^2/\text{s}$)	1000 - 5000	1000 - 5000
Wall heat flux ϕ_w (MW/m^2)	0.5 - 6	0.05 - 0.65
Thermodynamic flow quality x_{eq} (-)	(-0.4) - (+0.4)	(-0.4) - (+0.4)
Density ratio ρ_G/ρ_L (-)	0.08 - 0.25	0.07 - 0.22
Weber number We (-)	2374 - 368 579	3319 - 438 966
Boiling number Bo (-)	3.67×10^{-5} - 2.39×10^{-3}	2.65×10^{-5} - 1.74×10^{-3}

The DEBORA experiment consists of an upward subcooled boiling flow of R12 in a 4m length pipe uniformly heated over 3.5m with an hydraulic diameter $D_h = 19.2\text{mm}$. Measurements of void fraction (α), interfacial velocity (*i.e.* axial gas velocity $U_{g,z}$), bubble diameter (d_G), liquid temperature (T_L) and wall temperature (T_w) at the end of the heating length were conducted through different series of tests. Experimental apparatus is detailed in Garnier *et al.* [Garnier2001] and Manon[Manon2000].

Different test campaigns were conducted on this experimental setup, in particular :

- Campaign 2900 : measurements of α , $U_{g,z}$ and d_G using one optical probe
- Campaign 3000 : measurements of α , $U_{g,z}$ and d_G using two optical probes
- Campaign 800 : measurements of T_L and T_w using thermocouples

Each experimental case is named following this nomenclature : CccGgPppWwwTtt with cc being the campaign number, g the inlet mass velocity (G), pp the outlet pressure (P), ww the total heat power applied (W) and tt the inlet temperature (T_{in}). For instance, C8G3P26W23Te69 refers to the case from the campaign 800 with $G \approx 3000 \text{ kg/m}^2/\text{s}$, $P \approx 26 \text{ bar}$, $W \approx 23 \text{ kW}$ and $T_{in} \approx 69^\circ\text{C}$.

2.1.2 NEPTUNE_CFD simulations of DEBORA cases

In this work, we present the simulations of the following cases :

- C8G2P26W16Te44.9 and C8G2P26W16Te49.6 (single-phase flow)
- C8G2P26W16Te66.6 and C8G2P26W16Te70.3 (two-phase flow)
- C30G2P26W16Te66.6 and C30G2P26W16Te70.6 (two-phase flow)

The pressure of 26 bar is chosen to match the pressure of the mixing vanes cases (DEBORA-Promoteur, Section 6.1). Mesh sensitivity is performed over two meshes : a large mesh (M1) with 460 356 cells = 338 radial \times 1362 axial cells and a fine mesh (M2) with 3 157 952 cells = 1568 radial \times 2014 axial cells. On Figure 2.1, we present the results regarding liquid temperature at the outlet and wall temperature. The liquid temperature profile seems to be correctly reproduced by the simulations, though we see a slight overestimation close to the wall. Looking closer at boiling cases shows a difference of $\approx 0.5^\circ\text{C}$, which is close to the uncertainty of the measurements [Garnier2001]. Concerning the wall temperature, it appears that it is underestimated before the **Onset of Nucleate Boiling** (ONB) ($T_w < T_{sat}$) and overestimated after the ONB ($\approx +5^\circ\text{C}$). Post-ONB wall temperature is characterized by a stabilization of its value above the saturation temperature (here $T_{w,ONB} - T_{sat} \approx 2^\circ\text{C}$).

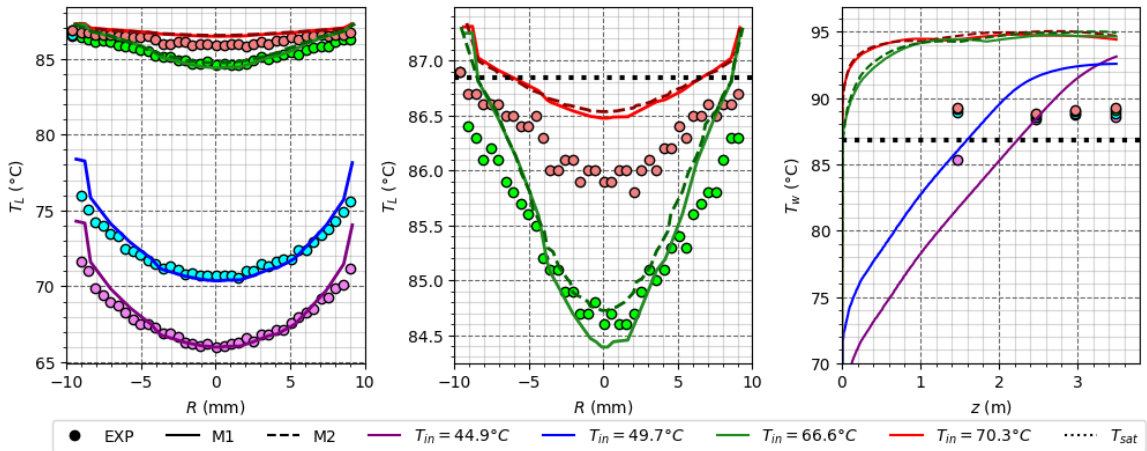


Figure 2.1: NCFD (lines) vs. Exp. (circles) - T_L and T_w - Cases C8G2P26W16Te44.9, Te49.6, Te66.6 and Te70.3 - Simulations using two meshes M1 (coarse) and M2 (fine).

On Figure 2.2, we compare the results of the simulations to the experiments regarding void fraction, bubble Sauter diameter and axial gas velocity. Void fraction profiles are quite correctly reproduced, though we observe a 10% higher peak at the wall for $T_{in} = 66.6^\circ\text{C}$. The order of magnitude of bubble diameter is correct ($\sim 0.1\text{mm}$) and NEPTUNE_CFD manages to detect coalescence (increase of bubble diameter when leaving the wall) and bulk condensation (decrease of bubble diameter when reaching the core of the flow), which is in qualitative agreement with the experiments. Quantitatively speaking, bubble diameter is globally underestimated. Finally, gas velocity profile is reasonably reproduced for $T_{in} = 66.6^\circ\text{C}$, but not for $T_{in} = 70.6^\circ\text{C}$. The latter experimental profile is flatter, which could be explained by a change of flow regime since uncondensed vapor is detected in the bulk.

Finally, the simulations reasonably agree with the experiments. The strongest discrepancies being mostly the wall temperature and bubble diameter. Potential ways of improving those results are investigated in next sub-section.

2.1.3 Investigating the nucleation site density modeling N_{sit}

In NEPTUNE_CFD, wall temperature is computed through the Heat Flux Partitioning model, which role is to find the appropriate T_w which balances Equation 5.1. However, some laws used to express param-

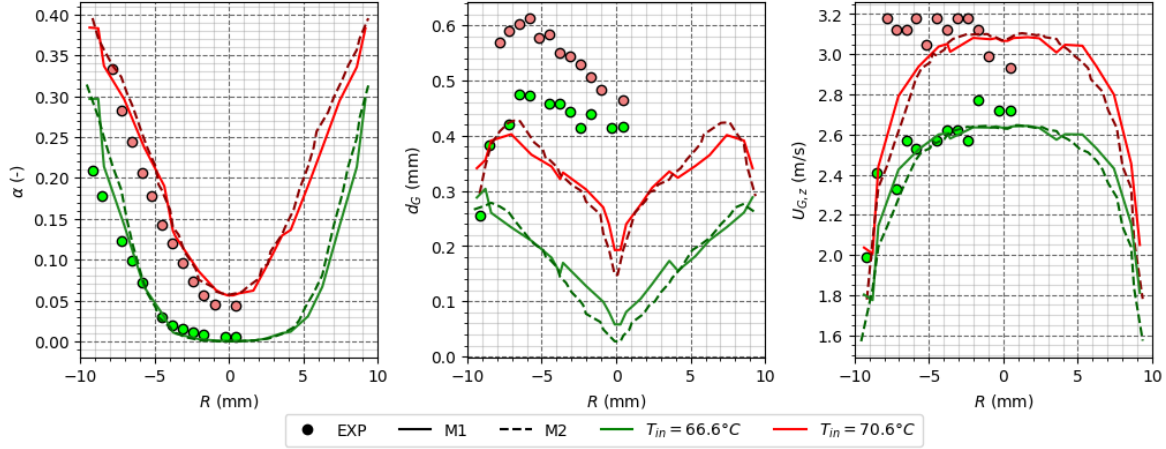


Figure 2.2: NCFD (lines) vs. Exp. (circles) - α , d_G and $U_{G,z}$ - Cases C30G2P26W16Te66.6 and Te70.6 - Simulations using two meshes M1 (coarse) and M2 (fine).

eters such as N_{sit} , f , or d_d are quite old and simple. For instance, the Lemmert & Chawla [Lemmert1977] expression of N_{sit} only depends on the wall superheat (Sub-section 1.1.5).

A comparison of the Lemmert & Chawla law [Lemmert1977] with the Hibiki & Ishii [Hibiki2003] law for N_{sit} against 4 data sets from the literature is presentend on Figure 2.3. The Hibiki & Ishii correlation depends simultaneously on wall superheat, pressure and contact angle. Experimental measurements of Borishanskii *et al.* [Borishanskii1961], Richenderfer *et al.* [Richenderfer2018], Kossolapov *et al.* [Kossolapov2020] and Zhou *et al.* [Zhou2020] are used to assess the two nucleation site density correlations.

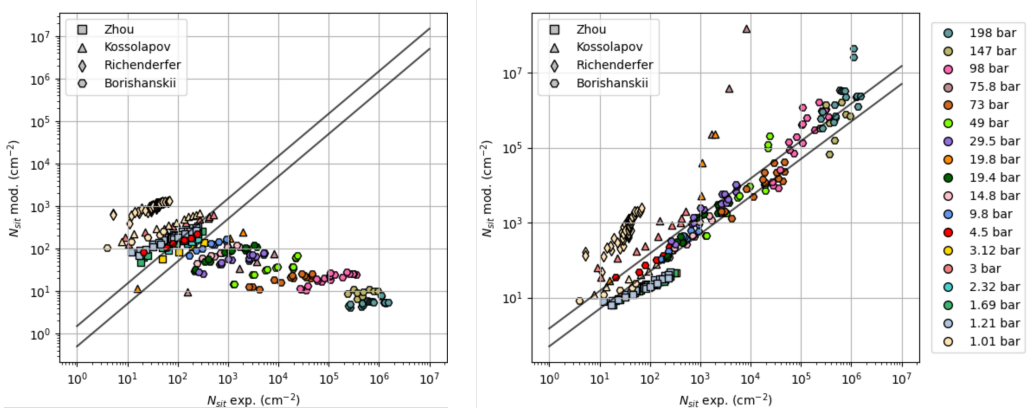


Figure 2.3: N_{sit} correlations of Lemmert & Chawla (left) and Hibiki & Ishii (right) vs. exp. data from literature. Operation pressures are displayed. $\pm 50\%$ error bars are drawn in black.

Figure 2.3 clearly shows that the Lemmert & Chawla law lack of pressure dependence fails to reproduce high pressure measurements contrary to the Hibiki & Ishii one. Even though Hibiki & Ishii correlation shows significant discrepancies with measurements of Kossolapov *et al.* and Richenderfer *et al.*, its prediction capability is greater in average than Lemmert & Chawla correlation.

To assess the influence of nucleation site density law on NEPTUNE_CFD computations, we compare results obtained with both correlations on Figure 2.4, which shows a remarkable impact of the modification of N_{sit} correlation. Using Hibiki & Ishii correlation reduces the error on T_w by approximately 2°C while α and T_L remain unchanged. This implies that the same heat flux partitioning is found with the two models, but that the pressure dependence of Hibiki & Ishii law helped to balance Equation 5.1 using a lower T_w , thus closer to experimental measurements.

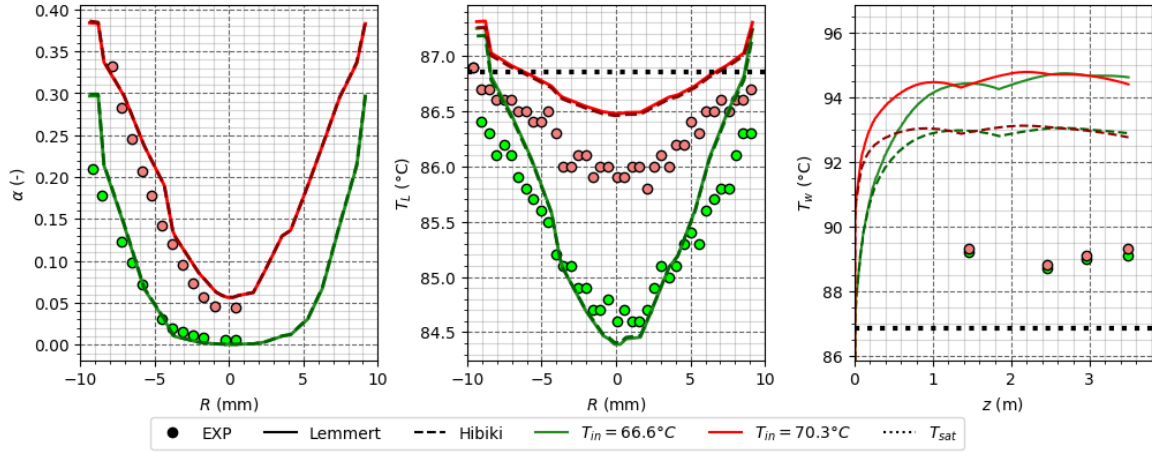


Figure 2.4: NCFD results for α , T_L and T_w using Lemmert & Chawla and Hibiki & Ishii correlation. Cases 8G2P26W23Te66.6 and Te70.3, 30G2P26W23Te66.6 and 70.6.

Such a result indicates that the HFP model could be improved through a systematic analysis of each parameter's impact and modeling (bubble departure diameter, detachment frequency, etc.). Assembling a more recent and consistent model could provide better results regarding wall temperature prediction. Models such as the one developed by Kommajosyula [Kommajosyula2020] could be interesting to apply for high-pressure flows.

Now that simple tube boiling flow has been assessed through the presented results, next section will focus on the simulation of boiling flow in a tube equipped with a mixing device.

Part III

DEVELOPMENT OF A NEW WALL HEAT FLUX PARTITIONING MODEL

3

EXISTING HEAT FLUX PARTITIONING MODELS

3.1 KURUL & PODOWSKI (1990)

In their original work published in 1990, Kurul & Podowski [**kurul_1990**] proposed a complete closure for the wall heat flux partitioning. They considered the applied heat flux to be divided between three mechanisms:

- A liquid single-phase heat flux $\phi_{c,L}$;
- A boiling heat flux ϕ_e ;
- A quenching heat flux ϕ_q induced by bubbles leaving the surface.

The total wall heat flux being :

$$\phi_w = \phi_{c,L} + \phi_e + \phi_q \quad (3.1)$$

The convective heat flux is expressed as :

$$\phi_{c,l} = A_{c,L} \rho_L c_p, L U_{L,\delta} \text{St}_{L,\delta} (T_w - T_{L,\delta}) \quad (3.2)$$

with δ a location in the buffer layer.

Assuming bubbles are spherical and leave the surface at diameter D_{lo} , they write:

$$\phi_e = \frac{1}{6} \pi D_{lo}^3 \rho_V h_{LV} f N_{sit} \quad (3.3)$$

$$(3.4)$$

The quenching heat flux occurring over the wait time t_w between two nucleated bubbles is computed as:

$$\phi_q = t_w f A_q \frac{2\lambda_L (T_w - T_{L,\delta})}{\sqrt{\pi \eta_L t_w}} \quad (3.5)$$

This expression corresponds to the average heat flux for semi-infinite conduction over a time t_w , as expressed by Del Valle and Kenning [**DelValle**].

They also estimate the portion of the surface affected by the bubbles as:

$$A_q = \min (1 ; F_A \pi R_{lo}^2 N_{sit}) = 1 - A_{c,L} \quad (3.6)$$

where $F_A = 4$ accounts for the bubble influence area when leaving the surface.

Needed closure relationships : N_{sit}, f, t_w, D_{lo}

3.2 BASU (2000)

In 2005, Basu *et al.* [Basu2005, Basu2005a] proposed a new HFP model together with a series of experiments to further study the different needed closure relationships. This model was meant to account for finer descriptions of the multiple phenomena at stake in subcooled flow boiling. In particular, they account for bubble sliding and merging and thus distinguish bubble departure diameter D_d (leaving the nucleation site) and lift-off diameter D_{lo} (leaving the wall).

Their approach consists of separating the boiling flow in three regions (Figure 3.1):

- Pre-ONB zone, where only liquid forced convection occurs, yielding:

$$\phi_w = h_{c,L} (T_w - T_L) \quad (3.7)$$

- Zone between the ONB and the OSV, prior to observing a net amount of vapor with bubble lifting off the surface. The heat flux is then still totally transferred to the liquid, but the equivalent convective heat transfer coefficient is supposed enhanced by 30% due to the presence of bubbles on the wall:

$$\phi_w = \bar{h}_{c,L} (T_w - T_L) \approx 1.3 h_{c,L} (T_w - T_L) \quad (3.8)$$

Basu *et al.* define the ONB as:

$$T_{w,ONB} = T_{sat} + \frac{4\sigma T_{sat}}{D_c \rho_V h_{LV}} \quad (3.9)$$

$$D_c = \sqrt{\frac{8\sigma T_{sat} \lambda_L}{\rho_V h_{LV} \phi_w}} (1 - \exp(-\theta^3 - 0.5\theta)) \quad (3.10)$$

- Post-OSV zone, where bubbles now leave the surface towards the bulk flow. This is where the other parts of the HFP appear *i.e.* the boiling and quenching fluxes. The beginning of OSV is defined by Basu *et al.* as:

$$T_{L,OSV} = T_{sat} - 0.7 \exp \left(-0.065 \frac{D_d h_{c,L}}{\lambda_L} \right) \frac{\phi_w}{h_{c,L}} \quad (3.11)$$

The hypothesis of Basu *et al.* is that the heat flux is first transferred to the superheated liquid close to the wall (by convection and transient quenching), part of which contributing to the evaporation through the liquid-vapor interface. The remaining heat is transferred to the bulk liquid (ϕ_L) either from the superheated liquid layer or bubble condensation. The whole heat transfer mechanism can thus be written as:

$$\phi_w = \phi_{c,L} + \phi_q = \phi_e + \phi_L \quad (3.12)$$

In order to estimate the quenching heat flux associated to bubble sliding and lift-off, Basu *et al.* consider two cases:

- 1) Bubble sliding from departure ($D = D_d$) to lift-off ($D = D_{lo}$) ;
- 2) Bubble coalescence with neighboring sites before departure.

Those two cases are distinguished using the average distance between nucleation sites s , which they suppose equal to $1/\sqrt{N_{sit}}$.

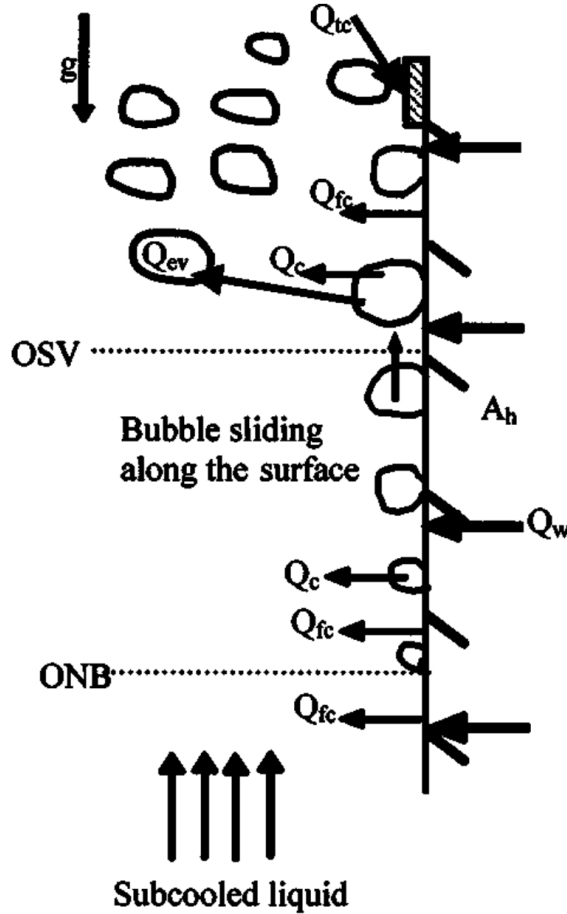


Figure 3.1: Sketch of the heat transfers zones considered by Basu *et al.*. (Adapted from [Basu2005])

3.2.1 Case 1 : Bubble sliding, $D_d < s$

In this situation, the bubble will grow up to its departure diameter D_d and slide over a length $l_{sl,0}$ before lifting-off. If $l_{sl,0} < s$, the bubble will slide up to its lift-off diameter D_l and leave the wall without colliding with other bubbles. On the contrary, if $l_{sl,0} \geq s$ the sliding bubble will merge with bubbles growing on their nucleation site, inducing a sudden growth of the bubble diameter that can exceed D_{lo} and thus lift-off after sliding over a reduced length $l_{sl} < l_{sl,0}$. Those assumptions are summarized on Figure 3.2.

If bubble coalescence occurs, the number of bubbles lifting-off the surface is lower than the actual number of nucleating sites. Basu *et al.* thus define a reduction factor:

$$R_f = \begin{cases} \frac{s}{l_{sl}} = \frac{1}{l\sqrt{N_{sit}}} & \text{if } l_{sl,0} \geq s \\ 1 & \text{if } l_{sl,0} < s \end{cases} \quad (3.13)$$

Regarding bubble sizes, they suppose that bubbles coalesced by a sliding bubble while growing have a diameter D_d *i.e.* they were close to departure (in reality, the coalesced bubble would have a diameter $D < D_d$). This results in a bubble of diameter $D = (D_{sl}^3 + D_d^3)^{1/3}$ which will lift-off if $D > D_{lo}$. Consequently, a sliding bubble can merge with numerous bubbles before lifting off. Noting N_{merg} the number of coalesced bubble and D_N the resulting bubble diameter, the sliding distance is:

$$l_{sl} = N_{merg}s + l_{D_N \rightarrow D_{lo}} \quad (3.14)$$

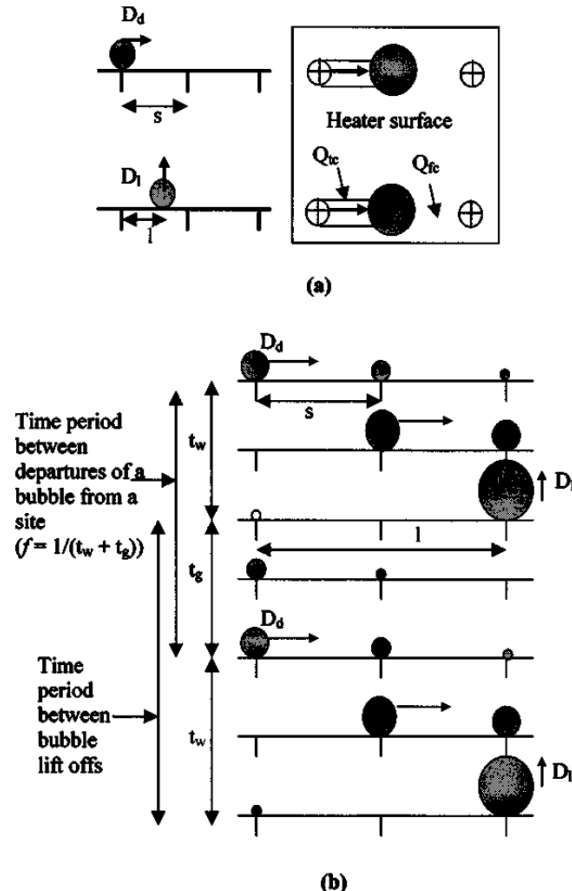


Figure 3.2: Sliding bubble behavior considered by Basu *et al.*. (Adapted from [Basu2005])

where $l_{D_N \rightarrow D_{lo}}$ is the remaining distance to slide if $D_N < D_{lo}$, being 0 if $D_N > D_{lo}$.

The surface swiped by the sliding bubble is then expressed as $A_{sl} = C\bar{D}l_{sl}$ with \bar{D} the average bubble diameter during sliding and C the ration between the bubble diameter and its foot, expressed correlating measurements from Maity [Maity2000] as :

$$C = 1 - \exp(2 - \theta^{0.6}) \quad (3.15)$$

After observing in their experiments that $D_d \approx 0.5D_{lo}$, Basu *et al.* choose:

$$\bar{D} = \frac{D_{lo} + D_d}{2} \approx 0.75D_{lo} \quad (3.16)$$

Noting $t^* = \left(\frac{\lambda_L}{h_{c,L}}\right)^2 \frac{1}{\pi\eta_L}$ the time at which transient conduction heat transfer becomes equal to forced liquid convection, the quenching heat flux is expressed as:

$$\phi_q = \frac{1}{t_w + t_g} \int_0^T \frac{\lambda_L}{\sqrt{\pi\eta_L t}} (T_w - T_L) A_{sl} R_f N_{sit} dt \quad (3.17)$$

where $T = t^*$ if $t^* < t_w + t_g$ (forced convection dominates at some point during a nucleation cycle) or $T = t_w + t_g$ if $t^* \geq t_w + t_g$ (transient conduction dominates over the whole nucleation cycle).

The liquid convective heat transfer is then:

$$\phi_{c,L} = \overline{h_{c,L}} (T_w - T_L) A_{c,L} + \overline{h_{c,L}} (T_w - T_L) A_{sl} R_f N_{sit} \left(1 - \min \left(1 ; \frac{t^*}{t_w + t_g} \right) \right) \quad (3.18)$$

with $A_{c,L} = 1 - A_{sl} R_f N_{sit}$.

And the boiling heat flux:

$$\phi_e = \rho_V h_{LV} \frac{\pi}{6} D_{lo}^3 R_f N_{sit} \frac{1}{t_w + t_g} \quad (3.19)$$

3.2.2 Case 2 : Bubble coalescence without sliding, $D_d \geq s$

Under higher wall superheats, the subsequent rise in the nucleation site density N_{sit} can lead to boiling regimes where bubbles coalesce with each other at early stages of their lifetime *i.e.* while still attached to their nucleation site. This situation is accounted for by Basu *et al.* in the case when $D_d \geq s$ by considering immediate lift-off of coalesced bubble at radius $D > D_{lo}$. In this case, the total number of bubbles leaving the surface is lower than N_{sit} and is thus reduced using:

$$R_f = \frac{s^3}{D_{lo}^3} \quad (3.20)$$

Under this massive coalescing regime, the entire surface will experience quenching due to bubble lift-off all over the heater. Depending on the values of t^* , we have:

$$\phi_q = \begin{cases} \frac{1}{t_w + t_g} \int_0^{t^*} \frac{\lambda_L}{\sqrt{\pi \eta_L t}} (T_w - T_L) dt & \text{if } t^* < t_w \\ \frac{1}{t_w + t_g} \left[\int_0^{t_w} \frac{\lambda_L}{\sqrt{\pi \eta_L t}} (T_w - T_L) dt + \int_0^T \frac{\lambda_L}{\sqrt{\pi \eta_L t}} (T_w - T_L) [1 - S_b N_{sit}] dt \right] & \text{if } t^* \geq t_w \end{cases} \quad (3.21)$$

$$\phi_{c,L} = \begin{cases} \overline{h_{c,L}} (T_w - T_L) \frac{t_w - t^*}{t_w + t_g} + \overline{h_{c,L}} (T_w - T_L) [1 - A_b N_{sit}] \frac{t_g}{t_w + t_g} & \text{if } t^* < t_w \\ \overline{h_{c,L}} (T_w - T_L) [1 - A_b N_{sit}] \frac{t_w + t_g - t^*}{t_w + t_g} & \text{if } t^* \geq t_w \end{cases} \quad (3.22)$$

with $A_b = \frac{\pi (Cs) 2}{4}$.

And the boiling heat flux still expressed as Eq. 3.19.

Needed closure relationships : $N_{sit}, t_w, t_g, D_d, D_{lo}, l_{sl,0}, h_{c,L}$.

3.3 GILMAN (2017)

A more recent HFP model dedicated to CFD simulations has been proposed by Gilman & Baglietto in 2017 [gilman2017]. Among the different advances proposed in their work, we can mention :

- A probabilistic law to account for static interaction between nucleation sites ;
- A force-balance approach to compute the bubble departure and lift-off diameters ;
- A generic law for the enhanced forced convection coefficient accounting for bubble presence ;
- The presence of a modified quenching term accounting for local wall superheat beneath a bubble dry spot.

The total heat flux is partitioned between the liquid forced convection $\phi_{c,L}$, the solid quenching $\phi_{q,s}$, the quenching due to bubble sliding $\phi_{q,sl}$ and the evaporation flux ϕ_e . Yielding:

$$\phi_w = \phi_{c,L} + \phi_{q,s} + \phi_{q,sl} + \phi_e \quad (3.23)$$

The convective term is computed in a way similar to Basu *et al.* [Basu2005] in Eq. 3.18:

$$\phi_{c,L} = \phi_{c1,L} + \phi_{c2,L} \quad (3.24)$$

$$= h_{c,L} (1 - A_{sl} N_{sit,a}^*) (T_w - T_L) + \overline{h_{c,L}} A_{sl} N_{sit,a}^* \left(1 - \frac{t^*}{t_w + t_g} \right) (T_w - T_L) \quad (3.25)$$

where $N_{sit,a}^*$ is the active nucleation site density that will generate sliding bubbles, that can differ from the empirical value of available sites N_{sit} usually computed by a correlation.

The active nucleation site density is actually smaller than N_{sit} since Gilman considers an static interaction between the available sites *i.e.* the fact that a bubble laying on a site may be blocking nucleation from sites laying beneath its foot. Following a Complete Spatial Randomness (CSR) approach, they express the probability to find a site under a growing bubble of radius R_d as:

$$\mathcal{P} = 1 - e^{-N_b \pi R_d^2} \quad (3.26)$$

where $N_b = \frac{t_g}{t_w + t_g} N_{sit}$ is the density of bubbles covering the heater.

The number of active sites is then computed as:

$$N_{sit,a} = (1 - \mathcal{P}) N_{sit} \quad (3.27)$$

$$= \exp \left(-\frac{t_g}{t_w + t_g} N_{sit} \pi R_d^2 \right) N_{sit} \quad (3.28)$$

This value is then reduced by Gilman to obtain $N_{sit,a}^*$ using a reduction factor representing sliding bubble coalescence (similar to Basu in Eq. 3.13):

$$N_{sit,a}^* = R_f N_{sit,a} = \frac{s}{l_{sl,0} + s} N_{sit,a} \quad (3.29)$$

The sliding quenching term is also computed in a similar way to Basu as:

$$\phi_{q,sl} = \frac{2\lambda_L (T_w - T_L)}{\sqrt{\pi \eta_L t^*}} A_{sl} N_{sit,a}^* \quad (3.30)$$

$$A_{sl} = \overline{D} l_{sl} = \frac{D_d + D_{lo}}{2} (N_{merg} s + l_{D_N \rightarrow D_{lo}}) \quad (3.31)$$

Regarding the boiling heat flux, Gilman splits it in two contributions respectively associated with the inception of nucleation and liquid microlayer evaporation :

$$\phi_e = \phi_{e,init} + \phi_{e,ML} \quad (3.32)$$

$$= \frac{4}{3} \pi R_d^3 \rho_V h_{LV} \frac{1}{t_w + t_g} N_{sit,a} + V_{ML} \rho_L h_{LV} \frac{1}{t_w + t_g} N_{sit,a} \quad (3.33)$$

$$\text{with } V_{ML} = \frac{2}{3} \pi \left(\frac{R_d}{2} \right)^3 \delta_{max} \quad (3.34)$$

where $\delta_{max} = 2 \mu\text{m}$ based on experiments from Gerardi [Gerardi].

Finally, the solid quenching term is written as:

$$\phi_{q,s} = \rho_w c_{p,w} V_q \delta T_q \frac{1}{t_g + t_w} N_{sit,a} \quad (3.35)$$

$$V_q = \frac{2}{3} \pi r_w^2 \quad (3.36)$$

with $\Delta T_q = 2 K$ as suggested by Gerardi *et al.* [Gerardi_etal].

Needed closure relationships : N_{sit} , t_w , t_g , D_d , D_{lo} , $l_{sl,0}$, $h_{c,L}$, $\overline{h_{c,L}}$.

3.4 ZHOU (2020)

The last HFP model we will look through in this Chapter was proposed by Zhou *et al.* [zhou]. It is one of the most recent available in the literature and was built along with associated experiments for validation. In particular they compute separate heat flux contributions for static (*st*) or sliding bubbles (*sl*), yielding a total heat flux:

$$\phi_w = \phi_{c,L} + (\phi_{e,st} + \phi_{e,sl}) + (\phi_{e,sl} + \phi_{q,sl}) \quad (3.37)$$

An interesting aspect of Zhou *et al.* work is the presence of a condensation term in the evaporation heat fluxes, written as:

$$\phi_{e,st} = \rho_V h_{LV} \frac{4}{3} \pi R_d^3 N_{sit,a} f + h_{cond} (T_{sat} - T_L) A_{cond} N_{sit,a} f (t_g - t_s) \quad (3.38)$$

$$\phi_{e,sl} = \frac{\pi}{6} \rho_V h_{LV} (D_{lo}^3 - D_d^3) f N_{sit}^* + h_{cond} (T_{sat} - T_L) A_{cond} N_{sit}^* t_{sl} f \quad (3.39)$$

$$A_{cond} = \pi D_d \max(R_d (1 + \cos(\theta)) - y_{sat}; 0) \quad (3.40)$$

where y_{sat} is the wall distance where the liquid is at saturation temperature, t_s the moment when $D_b = y_{sat}$ and N_{sit}^* the number of sliding bubbles.

The condensation heat transfer coefficient is computed using the correlation from Ranz & Marshall:

$$h_{cond} = \frac{\lambda_L}{D_d} (2 + 0.6 \text{Re}_b^{0.5}) \text{Pr}_L^{0.3} \quad (3.41)$$

Following similar approaches to HFP models from Basu or Gilman, the quenching heat flux for static bubbles is expressed as:

$$\phi_{q,st} = \begin{cases} t_w f \frac{2\lambda_L (T_w - T_L)}{\sqrt{\pi \eta_L t_w}} A_b N_{sit} & \text{if } t^* \geq t_w \\ t^* f \frac{2\lambda_L (T_w - T_L)}{\sqrt{\pi \eta_L t^*}} A_b N_{sit} + h_{c,L} (T_w - T_L) A_b N_{sit}^* f (t_w - t^*) & \text{if } t^* < t_w \end{cases} \quad (3.42)$$

with $A_b = \underbrace{K_b}_{=2} \pi R_d^2$.

And for the sliding bubbles:

$$\phi_{q,sl} = \begin{cases} \frac{2\lambda_L (T_w - T_L)}{\sqrt{\pi \eta_L (t_g + t_w)}} A_{sl} N_{sit}^* & \text{if } t^* \geq t_g + t_w \\ t^* f \frac{2\lambda_L (T_w - T_L)}{\sqrt{\pi \eta_L t^*}} A_b N_{sit}^* + h_{c,L} (T_w - T_L) A_{sl} N_{sit}^* f (t_g + t_w - t^*) & \text{if } t^* < t_w \end{cases} \quad (3.43)$$

with $A_{sl} = \underbrace{K_{sl}}_{=2} \frac{D_d + D_{lo}}{2} l_{sl}$ and $l_{sl} = \min(l_{sl,0}; \frac{1}{\sqrt{t_g f N_{sit}}})$.

Finally, the forced liquid convective heat flux is computed:

$$\phi_{c,L} = h_{c,L} (1 - A_b N_{sit} - A_{sl} N_{sit}^*) (T_w - T_L) \quad (3.44)$$

Needed closure relationships : N_{sit} , t_w , t_g , D_d , D_{lo} , $l_{sl,0}$, $h_{c,L}$.

3.5 CLOSURE LAWS FOR REMAINING PARAMETERS

In each of the 4 presented HFP models, there is a number of parameters that still need to be computed in order for the model to be fully expressed. Those parameters are often the nucleation site density, bubble diameters, etc. To do so, closure relationships are used and differ from one model to another. Here we want to sum up the different choices of the authors to point the variety of possibilities that exist.

3.5.1 Nucleation Site Density : N_{sit}

The value of the nucleation site density is a very sensitive parameter that controls the intensity of the boiling heat transfer. Unfortunately, its value can vary over a very large range of value depending on the operating conditions and heater material and is thus expressed using experimental correlations.

In their work, Kurul & Podowski used the law of Lemmert and Chawla [**Lemmert**]:

$$N_{sit} = [210 (T_w - T_{sat})]^{1.8} \quad (3.45)$$

Later, Basu [**Basu**] correlated her own experimental results to obtain:

$$N_{sit} = \begin{cases} 0.34 [1 - \cos(\theta)] \Delta T_w^2 & \text{if } \Delta T_{w,ONB} < \Delta T_w < 15 K \\ 3.4 \times 10^{-5} [1 - \cos(\theta)] \Delta T_w^{5.3} & \text{if } \Delta T_w > 15 K \end{cases} \quad (3.46)$$

In 2003, Hibiki & Ishii [**HI**] came up with a new correlation to estimate the nucleation site density that includes a pressure dependence, which has been used by Gilman & Baglietto [**Gilman**] and many other authors [**HI_others**]:

$$N_{sit} = N_0 \left(1 - \exp \left(-\frac{\theta^2}{8\mu^2} \right) \right) \left[\exp \left(f(\rho^+) \frac{\lambda'}{R_c} \right) - 1 \right] \quad (3.47)$$

$$R_c = \frac{2\sigma \left(1 + \frac{\rho_V}{\rho_L} \right) / P}{\exp \left(\frac{h_{LV} \Delta T_w}{R_g T_w T_{sat}} \right) - 1} \quad (3.48)$$

$$f(\rho^+) = -0.01064 + 0.48246\rho^+ - 0.22712\rho^{+2} + 0.05468\rho^{+3} \quad (3.49)$$

with R_g the perfect gas constant times the molar mass of the fluid, $N_0 = 4.72 \times 10^5 \text{ m}^{-2}$, $\mu = 0.722 \text{ rad}$, $\lambda' = 2.5 \times 10^{-3} \text{ m}$ and $\rho^+ = \log_{10} \left(\frac{\rho_L - \rho_V}{\rho_V} \right)$.

Finally, Zhou *et al.* followed a approach similar to Basu *et al.* by correlating their own experimental data:

$$N_{sit} = N_0 (1 - \cos(\theta)) [\exp(f(P) \Delta T_w) - 1] f(P) = 0.218 \ln\left(\frac{P}{P_0}\right) + 0.1907 \quad (3.50)$$

with $N_0 = 55\ 395.26\ \text{m}^{-2}$ and $P_0 = 1.01\ \text{bar}$.

3.5.2 Bubble Departure Frequency f , Growth Time t_g and Wait Time t_w

Historically, Kurul & Podowski modeled the BDF according to Cole [Cole] which derived an expression using photographic observations of bubble nucleation, further verified by Ceumern & Lindenstjerna for pool boiling of water at pressures up to 8 bar. :

$$f = \sqrt{\frac{4}{3} \frac{g(\rho_L - \rho_V)}{\rho_L D_d}} \quad (3.51)$$

Then, assuming that the growth time of the bubble before departure is small compared to the wait time before a new bubble nucleates ($t_{g,d} \ll t_w$) gives :

$$t_w \approx \frac{1}{f} \quad (3.52)$$

Although the assumption of a negligible growth time is true in different cases, notably when bubble departure diameter is small *i.e.* they leave their nucleation site nearly instantly, this is not generally true and the value of the ratio $\frac{t_{g,d}}{t_w}$ can vary by decades depending on the thermal-hydraulics conditions. Thus, later models considered separate modeling of the growth and wait time in order to compute the BDF as :

$$f = \frac{1}{t_{g,d} + t_w} \quad (3.53)$$

In this scope, Basu *et al.* [Basu] correlated their own experimental results to obtain :

$$t_g = \frac{D_d^2}{45 e^{-0.02 \text{Ja}_L} \eta_L \text{Ja}_w} \quad (3.54)$$

$$t_w = 139.1 \Delta T_w^{-4.1} \quad (3.55)$$

Gilman & Baglietto [Gilman] chose use the growth law of Zuber [Zuber1961] and the total BDF of Cole (Eq. 3.51) to close the relation 3.53.

$$t_{g,d} = \frac{\pi R_d^2}{4b^2 \text{Ja}_w \eta L}, \quad b = 1.56 \quad (3.56)$$

4

BOILING BUBBLE DYNAMICS

4.1 FORCE BALANCE MODELING

4.2 ESTABLISHMENT OF THE FORCE BALANCE FOR A BUBBLE ON A VERTICAL WALL

In this section, we wish to detail expressions of the different forces experienced by the bubble and to compare their magnitude in order to assess which will be predominant in the departure and lift-off process.

4.2.1 Bubble shape : Geometrical definitions

In order to clearly express each of the considered forces, assumptions regarding the shape of the bubble nucleating at the wall are needed.

Here, we assume that the bubbles will mostly have the shape of a truncated sphere with respect to the contact angle θ_s (Fig. 4.1), being a thermophysical property of the fluid and the wall. This assumption can thoroughly be discussed since many experimental measurements and visualizations have shown that in the case of low pressure boiling, bubbles tend to be strongly deformed depending on the flow conditions (MAITY, ESTRADA-PÉREZ *et al.*, etc.) thus casting doubts on spherical or quasi-spherical hypotheses.

On the other hand, experiments conducted by KOSSOLAPOV found that in vertical flow boiling, increasing pressure leads to smaller and less deformable bubbles. Thus, supposing a truncated spherical shape could be relevant to model nucleating bubbles on a heater surface. Moreover, working on highly deformed bubbles would undoubtedly imply complicated calculations and extra parameters to account for. KOSSOLAPOV's measurements also concluded that bubbles' inclination due to the flow nearly disappears at high pressures. However, since bubble tilt plays a great role in the surface tension force, we consider an angle tilt $d\theta$ compared to the static contact angle θ_s .

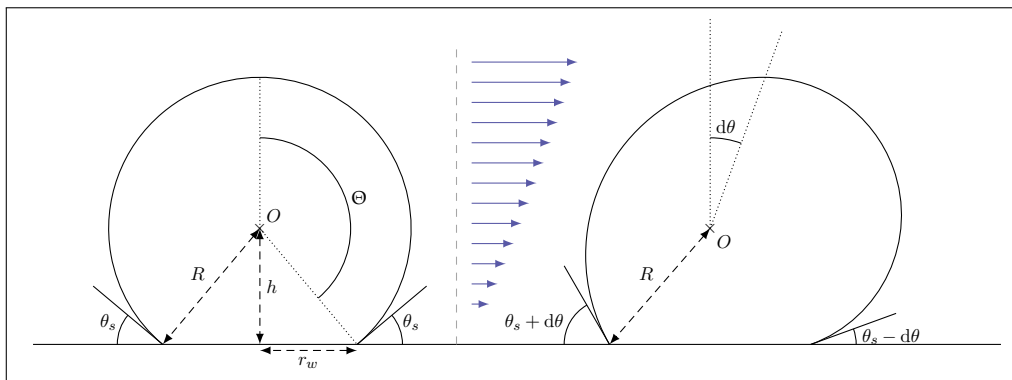


Figure 4.1: Sketch of the supposed bubble shape with (right) and without inclination (left).

The resulting bubble's volume V_b and projected area in the direction of the flow S_p can then be computed using the spherical coordinates system and defining the total angular portion covered by the bubble as $\Theta = \pi - \theta_s$, the bubble foot radius $r_w = R \sin(\theta_s)$ and the distance between the center of the bubble and the surface $h = R(1 + \cos(\theta_s))$, we have :

$$V_b = \underbrace{\int_{r=0}^R \int_{\theta=0}^{\Theta} \int_{\varphi=0}^{2\pi} r^2 \sin(\theta) dr d\theta d\varphi}_{\text{Spherical volume}} + \underbrace{\frac{1}{3}\pi r_w^2 h}_{\text{Conic volume}} = \frac{4}{3}\pi R^3 \left[\frac{1}{4}(2 - \cos(\theta_s))(1 + \cos(\theta_s))^2 \right] \quad (4.1)$$

$$S_p = \underbrace{\int_{r=0}^R \int_{\theta=-\Theta}^{\Theta} r dr d\theta}_{\text{Circular area}} + \underbrace{r_w h}_{\text{Triangular area}} = \pi R^2 \left[1 - \frac{\theta_s}{\pi} + \frac{\sin(2\theta_s)}{2\pi} \right] \quad (4.2)$$

Thus, we can define shape factors that represent the ratio between the volume and projected areas of the truncated sphere compared to a complete sphere :

$$f_V(\theta_s) = \frac{V_{ts}}{V_s} = \frac{1}{4} (2 - \cos(\theta_s)) (1 + \cos(\theta_s))^2 \quad (4.3)$$

$$f_{S_p}(\theta_s) = \frac{S_{p,ts}}{S_{p,s}} = 1 - \frac{\theta_s}{\pi} + \frac{\sin(2\theta_s)}{2\pi} \quad (4.4)$$

Subscripts s and ts respectively denoting spherical and truncated spherical shapes.

Using those assumptions, we can thus express the volume of vapor generated for a single bubble up to its lift-off diameter $D_{lo} = 2R_{lo}$ (Eq. 4.5) :

$$V_b = \frac{4}{3}\pi R_{lo}^3 f_V(\theta_s) = \frac{\pi D_{lo}^3}{6} f_V(\theta_s) \quad (4.5)$$

As described in Section 4.2.1, we consider a bubble with a potential inclination $d\alpha$ from the static contact angle θ_s . Thus, the downstream contact angle is $\theta_d = \theta_s - d\theta$ and the upstream contact angle is $\theta_u = \theta_s + d\theta$ (Figure 4.1).

To estimate the bubble foot radius r_w of such a bubble, we can express it as the average between the two foot diameters for the advancing and receding contact angles :

$$r_w = \frac{1}{2} (\sin(\theta_d) R + \sin(\theta_u) R) = R \sin(\theta_s) \cos(d\theta) \quad (4.6)$$

In the following subsections, the vectors \bar{e}_{\parallel} and \bar{e}_{\perp} respectively represent the colinear and orthogonal vector to the wall surface.

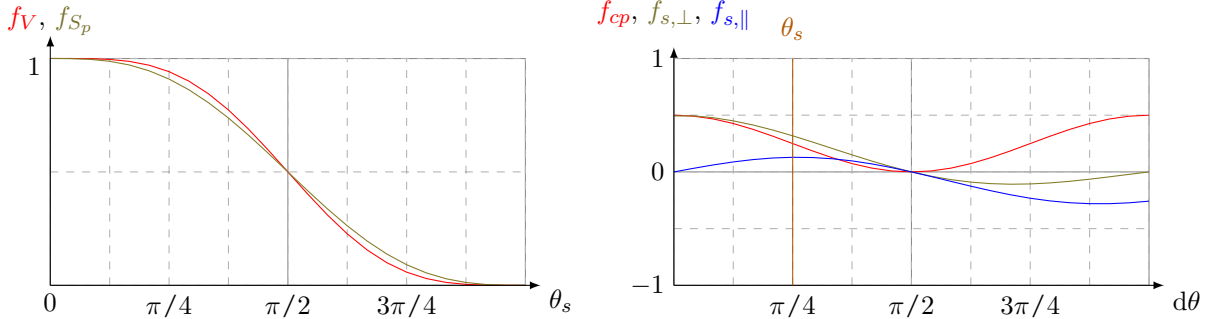


Figure 4.2: Representation of the shape functions

4.2.2 Buoyancy force

The well-known buoyancy force, also called Archimedes force, is computed by integration of the hydrostatic pressure exerted by the liquid over the bubble's surface and results in the difference between the gravity forces experienced by the vapour bubble and the equivalent liquid volume. The expression of this force $\overline{F_B}$ is aligned with the gravity vector $\bar{g} = -g\bar{e}_x$.

$$\overline{F_B} = V_b (\rho_V - \rho_L) \bar{g} = \frac{4}{3}\pi R^3 f_V(\theta_s) (\rho_L - \rho_V) g \bar{e}_x \quad (4.7)$$

4.2.3 Contact Pressure force

The contact pressure force arises due to the pressure difference between the center of the bubble and the surrounding liquid. This pressure jump can be computed using LAPLACE's expression $\Delta P = 2\sigma/R_c$ where R_c is the curvature radius of the bubble's interface, being equal to R in the case of a spherical bubble. This pressure difference is then applied over the bubble foot area and results in a repelling force from the bubble's point of view, giving the resulting expression of $\overline{F_{CP}}$.

$$\overline{F_{CP}} = \frac{2\sigma}{R_c} \frac{\pi d_w^2}{4} \overline{e_y} \approx 2\sigma\pi R \underbrace{\sin^2(\theta) \cos^2(d\theta)}_{f_{CP}} \overline{e_\perp} = 2\pi R\sigma f_{CP}(\theta, d\theta) \overline{e_x} \quad (4.8)$$

(4.9)

4.2.4 Capillary force

The capillary or surface tension force results from the integration of the effort exerted over the triple contact line between the vapor inside the bubble, the surrounding liquid and the wall. This force has been derived by KLAUSNER[CITE] for a inclined bubble, yielding for each direction regarding the wall :

$$\overline{F_C} = -1.25 d_w \sigma \frac{\pi (\theta_u - \theta_d)}{\pi^2 - (\theta_u - \theta_d)^2} (\sin(\theta_u) + \sin(\theta_d)) \overline{e_x} - d_w \sigma \frac{\pi}{\theta_u - \theta_d} (\cos(\alpha_d) - \cos(\alpha_u)) \overline{e_y} \quad (4.10)$$

$$\approx -\pi R\sigma \underbrace{\left[1.25 \frac{2d\theta}{(\frac{\pi}{2})^2 - d\theta^2} \sin(\theta_s)^2 \cos(d\theta)^2 \right]}_{f_{C,x}} \overline{e_x} - \pi R\sigma \underbrace{\left[2 \sin(\theta_s)^2 \frac{\sin(2d\theta)}{2d\theta} \right]}_{f_{C,y}} \overline{e_y} \quad (4.11)$$

$$= -\pi R\sigma f_{C,x}(\theta_s, d\theta) \overline{e_x} - \pi R\sigma f_{C,y}(\theta_s, d\theta) \overline{e_y} \quad (4.12)$$

4.2.5 Added Mass force of a growing bubble

Added mass effects are experienced by the bubble :

- when its boundary is moving during its growth
- when accelerating while sliding on the wall
- when the surrounding liquid is accelerating

We consider a spherical cap shaped bubble standing on a plane wall and facing an uniform liquid velocity U . In this situation, Van Der Geld derived the potential flow around the bubble and expressed the liquid kinetic energy, obtaining :

$$T_L = \rho_L V_b \left(\frac{1}{2} \alpha \dot{y}^2 + \frac{1}{2} \text{tr}(\beta) \dot{R}^2 + \frac{1}{2} \psi \dot{R} \dot{y} + \frac{1}{2} \alpha_2 U^2 \right) \quad (4.13)$$

where α , $\text{tr}(\beta)$, ψ and α_2 are polynomimals of $\lambda = \frac{R}{2h}$. We also have x and $y = h$ denoting the coordinates of the geometrical center of the bubble.

Therefore, we can write those coefficients in the following form :

$$\alpha = \sum_{k=0}^n \alpha_k \frac{R^k}{2^k y^k} \quad (4.14)$$

If we suppose that the generalized coordinates and velocities x , \dot{x} , y , \dot{y} , R , and \dot{R} , we can use the expression of the kinetic energy of the fluid to apply Lagrange's equations to derive the added mass forces on the bubble in both direction parallel and normal to the wall :

$$F_{AM,x} = -\frac{\partial}{\partial t} \left(\frac{\partial T_L}{\partial \dot{x}} \right) + \frac{\partial T_L}{\partial x} \quad (4.15)$$

$$F_{AM,y} = -\frac{\partial}{\partial t} \left(\frac{\partial T_L}{\partial \dot{y}} \right) + \frac{\partial T_L}{\partial y} \quad (4.16)$$

In the case of the sliding bubble, we replace the uniform liquid velocity U by the relative velocity experienced by the bubble $U_{rel} = U_{liq} - \dot{x}$ where U_{liq} is the uniform surrounding liquid velocity and \dot{x} the velocity of the center of the bubble, which is the sliding velocity of the bubble. Yielding :

$$T_L = \frac{\rho_L V_b}{2} \left(\alpha \dot{y}^2 + \text{tr}(\beta) \dot{R}^2 + \psi \dot{R} \dot{y} + \alpha_2 (U_{liq} - \dot{x})^2 \right) \quad (4.17)$$

ADDED MASS IN x DIRECTION Parallel to the wall, since λ depends on y and R , it is independent of \dot{x} , yielding zero-derivatives for the added mass coefficients. We can write :

$$\frac{\partial T_L}{\partial \dot{x}} = \frac{\rho_L V_b}{2} \alpha_2 \frac{\partial ((U_{liq} - \dot{x})^2)}{\partial \dot{x}} \quad (4.18)$$

$$= \rho_L V_b \alpha_2 (\dot{x} - U_{liq}) \quad (4.19)$$

$$(4.20)$$

As for the time derivatives, we have :

$$\frac{\partial V_b}{\partial t} = \frac{\partial \frac{4}{3} \pi R^3}{\partial t} = 4\pi R^2 \dot{R} \quad (4.21)$$

$$\frac{\partial \lambda}{\partial t} = \frac{\dot{R} 2y - R 2\dot{y}}{4y^2} = \lambda \left(\frac{\dot{R}}{R} - \frac{\dot{y}}{y} \right) = \lambda \left(\frac{\dot{R}}{R} - 2\lambda \frac{\dot{y}}{R} \right) = \frac{\lambda}{R} (\dot{R} - 2\lambda \dot{y}) \quad (4.22)$$

$$\frac{\partial \alpha}{\partial t} = \sum_{k=0}^n \alpha_k \frac{\partial \lambda^k}{\partial t} = \sum_{k=0}^n \alpha_k k \lambda^{k-1} \frac{\partial \lambda}{\partial t} = \left(\frac{\dot{R}}{R} - \frac{\dot{y}}{y} \right) \underbrace{\sum_{k=0}^n \alpha_k k \lambda^k}_{\tilde{\alpha}} = \frac{1}{R} (\dot{R} - 2\lambda \dot{y}) \tilde{\alpha} \quad (4.23)$$

Yielding :

$$\frac{\partial}{\partial t} \left(\frac{\partial T_L}{\partial \dot{x}} \right) = \rho_L \left[4\pi R^2 \dot{R} \alpha_2 (\dot{x} - U_{liq}) + \frac{4}{3} \pi R^3 \left(\frac{\dot{R}}{R} - \frac{\dot{y}}{y} \right) \tilde{\alpha}_2 (\dot{x} - U_{liq}) + \frac{4}{3} \pi R^3 \alpha_2 \ddot{x} \right] \quad (4.24)$$

$$= 4\pi R^2 \rho_L \left[\alpha_2 \dot{R} (\dot{x} - U_{liq}) + \frac{\tilde{\alpha}_2}{3} (\dot{R} - 2\lambda \dot{y}) (\dot{x} - U_{liq}) + \frac{R}{3} \alpha_2 \ddot{x} \right] \quad (4.25)$$

$$= 4\pi R^2 \rho_L \left[\left(\alpha_2 + \frac{\tilde{\alpha}_2}{3} \right) \dot{R} (\dot{x} - U_{liq}) - \frac{2}{3} \lambda \tilde{\alpha}_2 \dot{y} (\dot{x} - U_{liq}) + \frac{R}{3} \alpha_2 \ddot{x} \right] \quad (4.26)$$

We also have, with the independence of the variables :

$$\frac{\partial T_L}{\partial x} = 0 \quad (4.27)$$

Finally yielding,

$$F_{AM,x} = 4\pi R^2 \rho_L \left[\left(\alpha_2 + \frac{\tilde{\alpha}_2}{3} \right) \dot{R} U_{rel} - \frac{2}{3} \lambda \tilde{\alpha}_2 \dot{y} U_{rel} - \frac{R}{3} \alpha_2 \ddot{x} \right] \quad (4.28)$$

We can immediately observe that the added mass related to the bubble growth will promote detachment when the bubble is still attached to its nucleation site ($\dot{x} = 0$). This contradicts the often-used approach using solely the Rayleigh-Plesset equation projected in both direction using the inclination angle of the bubble.

The other part of this added-mass force is naturally linked to the acceleration of the bubble and the mass of displaced liquid.

ADDED MASS IN y DIRECTION Following the same approach normal to the wall, we obtain :

$$\frac{\partial T_L}{\partial \dot{y}} = \frac{1}{2} \rho_L \frac{4}{3} \pi R^3 (\alpha_2 \dot{y} + \psi \dot{R}) = \rho_L \frac{4}{3} \pi R^3 \left(\alpha \dot{y} + \frac{\psi}{2} \dot{R} \right) \quad (4.29)$$

$$\begin{aligned} \frac{\partial}{\partial t} \left(\frac{\partial T_L}{\partial \dot{y}} \right) &= \rho_L 4\pi R^2 \dot{R} \left(\alpha \dot{y} + \frac{1}{2} \psi \dot{R} \right) + \rho_L \frac{4}{3} \pi R^3 \left(\frac{1}{R} (\dot{R} - 2\lambda \dot{y}) \tilde{\alpha} \dot{y} + \alpha \ddot{y} + \frac{1}{2} \tilde{\psi} \frac{1}{R} (\dot{R} - 2\lambda \dot{y}) \dot{R} + \frac{1}{2} \psi \ddot{R} \right) \\ &= \rho_L 4\pi R^2 \left[\frac{\alpha}{3} R \ddot{y} + \frac{\psi}{6} R \ddot{R} + \left(\frac{\psi}{2} + \frac{\tilde{\psi}}{6} \right) \dot{R}^2 - \frac{2}{3} \lambda \tilde{\alpha} \dot{y}^2 + \left(\alpha + \frac{\tilde{\alpha}}{3} - \frac{\tilde{\psi}}{3} \right) \dot{R} \dot{y} \right] \end{aligned} \quad (4.30) \quad (4.31)$$

$$\frac{\partial T_L}{\partial y} = \rho_L \frac{4}{3} \pi R^3 \left(\frac{1}{2} \frac{\partial \alpha}{\partial y} \dot{y}^2 + \frac{1}{2} \frac{\partial \text{tr}(\beta)}{\partial y} \dot{R}^2 + \frac{1}{2} \frac{\partial \psi}{\partial y} \dot{R} \dot{y} + \frac{1}{2} \frac{\partial \alpha_2}{\partial y} (U_{liq} - \dot{x})^2 \right) \quad (4.32)$$

Where we can write :

$$\frac{\partial \alpha}{\partial y} = \sum_{k=0}^n \alpha_k \frac{\partial \lambda^k}{\partial y} = \sum_{k=0}^n \alpha_k \frac{R^k}{2^k} \frac{\partial}{\partial y} \left(\frac{1}{y^k} \right) = \sum_{k=0}^n \alpha_k \frac{R^k}{2^k} (-k) \frac{1}{y^{k+1}} = \frac{1}{y} \sum_{k=0}^n (-k) \alpha_k \lambda^k = -\frac{1}{y} \tilde{\alpha} \quad (4.33)$$

Giving :

$$\frac{\partial T_L}{\partial y} = \rho_L 4\pi R^2 \frac{R}{6y} \left[-\tilde{\alpha} \dot{y}^2 - \text{tr}(\tilde{\beta}) \dot{R}^2 - \tilde{\psi} \dot{R} \dot{y} - \tilde{\alpha}_2 U_{rel}^2 \right] \quad (4.34)$$

$$= -\rho_L 4\pi R^2 \frac{\lambda}{3} \left[\tilde{\alpha} \dot{y}^2 + \text{tr}(\tilde{\beta}) \dot{R}^2 + \tilde{\psi} \dot{R} \dot{y} + \tilde{\alpha}_2 U_{rel}^2 \right] \quad (4.35)$$

Which finally yields :

$$\begin{aligned} F_{AM,y} &= -\rho_L 4\pi R^2 \left[\frac{\alpha}{3} R \ddot{y} + \frac{\psi}{6} R \ddot{R} + \left(\frac{\psi}{2} + \frac{\tilde{\psi}}{6} \right) \dot{R}^2 - \frac{2}{3} \lambda \tilde{\alpha} \dot{y}^2 + \left(\alpha + \frac{\tilde{\alpha}}{3} - \frac{\tilde{\psi}}{3} \right) \dot{R} \dot{y} \right] \\ &\quad - \rho_L 4\pi R^2 \frac{\lambda}{3} \left[\tilde{\alpha} \dot{y}^2 + \text{tr}(\tilde{\beta}) \dot{R}^2 + \tilde{\psi} \dot{R} \dot{y} + \tilde{\alpha}_2 U_{rel}^2 \right] \end{aligned} \quad (4.36)$$

$$\begin{aligned} &= \rho_L 4\pi R^2 \left[\frac{\lambda}{3} \tilde{\alpha} \dot{y}^2 + \left(-\frac{\lambda}{3} \text{tr}(\tilde{\beta}) - \frac{\psi}{2} - \frac{\tilde{\psi}}{6} \right) \dot{R}^2 + \left(-\alpha - \frac{\tilde{\alpha}}{3} + \frac{1-\lambda}{3} \tilde{\psi} \right) \dot{R} \dot{y} - \frac{\alpha}{3} R \ddot{y} - \frac{\psi}{6} R \ddot{R} - \frac{\lambda}{3} \tilde{\alpha}_2 U_{rel}^2 \right] \end{aligned} \quad (4.37)$$

Where :

$$\begin{aligned}\alpha = & 111.62137 - 844.131315\lambda + 2678.058461\lambda^2 - 4534.349913\lambda^3 \\ & + 4311.889654\lambda^4 - 2180.345705\lambda^5 + 457.591961\lambda^6\end{aligned}\quad (4.38)$$

$$\begin{aligned}\psi = & -220.824854 + 1639.114567\lambda - 5130.691427\lambda^2 + 8625.857798\lambda^3 \\ & - 8169.91248\lambda^4 + 4121.492877\lambda^5 - 863.784836\lambda^6\end{aligned}\quad (4.39)$$

$$\begin{aligned}\text{tr}(\beta) = & 104.601303 - 736.214699\lambda + 2293.784611\lambda^2 - 3857.878559\lambda^3 \\ & + 3659.95521\lambda^4 - 1849.854303\lambda^5 + 388.412909\lambda^6\end{aligned}\quad (4.40)$$

$$\alpha_2 = 0.359528 + 1.341274\lambda - 1.973813\lambda^2 + 0.796613\lambda^3 \quad (4.41)$$

If we define added mass coefficients C_{AM} as :

$$F_{AM,x} = \pi R^2 \rho_L (C_{AM,x1} \dot{R} U_{rel} + C_{AM,x2} \dot{y} U_{rel} + C_{AM,x3} R \ddot{x}) \quad (4.42)$$

$$F_{AM,y} = \pi R^2 \rho_L (C_{AM,y1} \dot{y}^2 + C_{AM,y2} \dot{R}^2 + C_{AM,y3} \dot{R} \dot{y} + C_{AM,y4} R \ddot{y} + C_{AM,y5} R \ddot{R} + C_{AM,y6} U_{rel}^2) \quad (4.43)$$

We obtain :

$$C_{AM,x1} = 6.372904\lambda^3 - 13.1587533\lambda^2 + 7.15346133\lambda + 1.438112 \quad (4.44)$$

$$C_{AM,x2} = -6.372904\lambda^4 + 10.527002667\lambda^3 - 3.576730667\lambda^2 \quad (4.45)$$

$$C_{AM,x3} = -1.062150667\lambda^3 + 2.631750667\lambda^2 - 1.78836533\lambda - 0.479370667 \quad (4.46)$$

$$\begin{aligned}C_{AM,y1} = & 3660.735688\lambda^7 - 14535.638033\lambda^6 + 22996.74482133\lambda^5 - 18137.399652\lambda^4 + 7141.48922933\lambda^3 \\ & - 1125.50842\lambda^2\end{aligned}\quad (4.47)$$

$$\begin{aligned}C_{AM,y2} = & -3107.303272\lambda^7 + 17515.071036\lambda^6 - 41501.056736\lambda^5 + 53557.772476\lambda^4 - 40620.190154667\lambda^3 \\ & + 18083.92435533\lambda^2 - 4370.972178667\lambda + 441.649708\end{aligned}\quad (4.48)$$

$$\begin{aligned}C_{AM,y3} = & 6910.278688\lambda^7 - 39878.0014\lambda^6 + 94306.5065933\lambda^5 - 118320.60118933\lambda^4 + 84460.07430133\lambda^3 \\ & - 33721.052968\lambda^2 + 6687.51976933\lambda - 446.48548\end{aligned}\quad (4.49)$$

$$\begin{aligned}C_{AM,y4} = & -610.122614667\lambda^6 + 2907.12760667\lambda^5 - 5749.18620533\lambda^4 + 6045.799884\lambda^3 \\ & - 3570.744614667\lambda^2 + 1125.50842\lambda - 148.8284933\end{aligned}\quad (4.50)$$

$$\begin{aligned}C_{AM,y5} = & 575.85655733\lambda^6 - 2747.661918\lambda^5 + 5446.60832\lambda^4 - 5750.57186533\lambda^3 \\ & + 3420.46095133\lambda^2 - 1092.743044667\lambda + 147.21656933\end{aligned}\quad (4.51)$$

$$\begin{aligned}C_{AM,y6} = & -3.186452\lambda^4 + 5.26350133\lambda^3 - 1.78836533\lambda^2 \\ & \quad (4.52)\end{aligned}\quad (4.53)$$

In the case of the full or truncated sphere on a wall, we can write $y = R\cos(\theta)$ and $\dot{y} = \dot{R}\cos(\theta)$ if we suppose a quasi-constant contact angle during bubble lifetime. Moreover, $\lambda = 1/2\cos(\theta)$.

The added-mass forces then become :

$$F_{AM,x} = \rho_L \pi R^2 [(C_{AM,x1} + C_{AM,x2}\cos(\theta)) \dot{R} U_{rel} + C_{AM,x3} R \ddot{x}] \quad (4.54)$$

$$F_{AM,y} = \rho_L \pi R^2 [(C_{AM,y1}\cos(\theta)^2 + C_{AM,y2} + C_{AM,y3}\cos(\theta)) \dot{R}^2 + (C_{AM,y4}\cos(\theta) + C_{AM,y5}) R \ddot{R} + C_{AM,y6} U_{rel}^2] \quad (4.55)$$

Finally, if we consider the full sphere case : $\theta = 0$ and $\lambda = 0.5$, we can estimate the numerical values of the sphere added mass coefficients $C_{AM,S}$:

$$F_{AM,x} = \rho_L \pi R^2 [C_{AM,Sx1} \dot{R} U_{rel} + C_{AM,Sx2} R \ddot{x}] \quad (4.56)$$

$$F_{AM,y} = \rho_L \pi R^2 [C_{AM,Sy1} \dot{R}^2 + C_{AM,Sy2} R \ddot{R} + C_{AM,Sy3} U_{rel}^2] \quad (4.57)$$

where $C_{AM,Sx1} \approx 2.5451535$; $C_{AM,Sx2} \approx -0.8483845$

$C_{AM,Sy1} \approx 4.774859833$; $C_{AM,Sy2} \approx -0.359872041667$ and $C_{AM,Sy3} \approx 0.0116930833$

4.2.6 Added Mass from Duhar et al.

$$\overline{F_{AM}} = -\rho_L \frac{d}{dt} \left[V_b \frac{1}{2} \left(1 + \frac{3}{16} \left(\frac{R}{y} \right)^3 \right) (U_{b,x} - U_L) \overline{e_x} + V_b \frac{1}{2} \left(1 + \frac{3}{8} \left(\frac{R}{y} \right)^3 \right) U_{b,y} \overline{e_y} \right] \quad (4.58)$$

$$+ \frac{3}{32} \rho_L \frac{d^2}{dt^2} (RV_b) \left(\frac{R}{y} \right)^2 \overline{e_y} + \frac{\pi R^2}{2} \left(\frac{R}{y} \right)^4 \left[\frac{3}{8} U_{rel}^2 + \frac{3}{4} U_{b,y}^2 \right] \overline{e_y} \quad (4.59)$$

Yielding :

$$\overline{F_{AM}} \cdot \overline{e_x} = \frac{\rho_L V_b}{2} \left[3 \left(1 + \frac{3}{16} \left(\frac{R}{y} \right)^3 \right) \frac{\dot{R}}{R} U_{rel} + \frac{9}{16} \left(\frac{R}{y} \right)^3 \left(\frac{\dot{R}}{R} - \frac{\dot{y}}{y} \right) U_{rel} - \left(1 + \frac{3}{16} \left(\frac{R}{y} \right)^3 \right) \frac{\partial U_{b,x}}{\partial t} \right] \quad (4.60)$$

$$\overline{F_{AM}} \cdot \overline{e_y} = -\frac{\rho_L V_b}{2} \left[3 \left(1 + \frac{3}{8} \left(\frac{R}{y} \right)^3 \right) \frac{\dot{R}}{R} U_{b,y} + \frac{3}{8} \left(\frac{R}{y} \right)^3 \left(\frac{\dot{R}}{R} - \frac{\dot{y}}{y} \right) U_{b,y} + \left(1 + \frac{3}{8} \left(\frac{R}{y} \right)^3 \right) \frac{\partial U_{b,y}}{\partial t} \right] \quad (4.61)$$

$$\frac{\rho_L V_b}{2} \left[\frac{3}{4} \left(\frac{R}{y} \right)^2 \left(\ddot{R} + 3 \frac{\dot{R}^2}{R} \right) \right] + \frac{\rho_L V_b}{2} \left[\frac{3}{4} \left(\frac{R}{y} \right)^4 \left(\frac{3}{8} \frac{U_{rel}^2}{R} + \frac{3}{4} \frac{U_{b,y}^2}{R} \right) \right] \quad (4.62)$$

4.2.7 Lift and drag forces

The lift force and the drag force represent the two components of the global hydrodynamic effort exerted by the surrounding flow over a bubble. The lift force corresponds to the force directed orthogonally to the flow direction while the drag is the colinear one.

Those forces are usually expressed using both the projected area of the bubble facing the flow and the relative velocity along with a lift coefficient C_L and a drag coefficient C_D respectively.

$$\overline{F_D} = \frac{1}{2} C_D S_p \rho_l U_{rel}^2 \overline{e_{||}} \quad (4.63)$$

$$= \frac{1}{2} C_D \pi R^2 f_{S_p}(\alpha) \rho_l U_{rel}^2 \overline{e_{||}} \quad (4.64)$$

$$\overline{F_L} = \frac{1}{2} C_L S_p \rho_l U_{rel}^2 \overline{e_{\perp}} \quad (4.65)$$

$$= \frac{1}{2} C_L \pi R^2 f_{S_p}(\alpha) \rho_l U_{rel}^2 \overline{e_{\perp}} \quad (4.66)$$

In those two expressions, the main parameter remains C_D and C_L which modeling can be developed depending on the flow characteristics (uniform, shear, wall influence, etc.). For instance, one of the most recent and complete expression of those coefficients have been derived from DNS conducted by SHI *et al.* which takes into account the distance to the wall and the shear rate simultaneously.

4.2.7.1 Drag and lift coefficient from Shi *et al.*

In this section, we detail the expression of the drag and lift coefficient derived by Shi *et al.* from multiple DNS simulations.

The following notations are proper to this sub-section of the document. Variables used by Shi *et al.* to describe drag and lift are detailed on Table 4.1

Name	Definition	Unit
d	Bubble diameter	m
γ	Flow shear rate	s ⁻¹
\tilde{L}	Distance to the wall	m
\tilde{L}_u	$\nu_l / U_{rel} $	m
\tilde{L}_ω	$\sqrt{\nu_l / \omega}$	m
L_u	\tilde{L} / \tilde{L}_u	(-)
L_ω	$\tilde{L} / \tilde{L}_\omega$	(-)
L_R	$2\tilde{L}/d$	(-)
Re	$ U_{rel} d / \nu_l$	(-)
Sr	$\gamma d / U_{rel}$	(-)
ε	$\tilde{L}_u / \tilde{L}_\omega = \sqrt{ Sr / Re}$	(-)

Table 4.1: Variables used by Shi *et al.*

The drag and lift coefficient are computed from their DNS results by integrating the hydrodynamic effort over the bubble's surface. The axial and radial component respectively yielding the drag and lift coefficient when divided by $\pi d^2 \rho_l U_{rel}^2 / 8$.

DRAG COEFFICIENT : The total drag coefficient is expressed as a correction ΔC_D^W of a uniform drag coefficient C_{D0}^U to account for shear and wall effects :

$$C_D^W = \Delta C_D^W C_{D0}^U + C_{D0}^U = C_{D0}^U \left(1 + \Delta C_D^W \right) \quad (4.67)$$

$$\text{with } C_{D0}^U (\text{Re} \gg 1) = \frac{48}{\text{Re}} \quad (\text{Kang and Leal, 1988}) \quad (4.68)$$

$$\Delta C_D^W (\text{Re}) \approx \Delta C_D^W [\text{Re} = O(1)] + c_{D\infty} \Delta C_D^W (\text{Re} \gg 1) \quad (4.69)$$

$$\text{with } c_{D\infty} = 1 - e^{-0.07\text{Re}} \quad (4.70)$$

$$\Delta C_D^W [\text{Re} = O(1)] \approx f'_D (L_u) b^2 (\text{Re}) \Delta C_D^{\text{W-in}} \quad (4.71)$$

$$f'_D (L_u) \approx \frac{1}{1 + 0.16L_u (L_u + 4)} \quad (4.72)$$

$$b (\text{Re}) = 1 + \tanh (0.012\text{Re}^{0.8}) + \tanh (0.07\text{Re}^{0.8}) \quad (4.73)$$

$$\Delta C_D^{\text{W-in}} (\text{Sr}, L_R) = \left(\frac{3}{8} L_R^{-1} + \frac{3}{64} L_R^{-4} \right) \left(1 - \frac{3}{8} L_R^{-1} - \frac{3}{64} L_R^{-4} \right)^{-1} - \frac{1}{16} \left(L_R^{-2} + \frac{3}{8} L_R^{-3} \right) \text{Sr} \quad (4.74)$$

They actually operate a blending between a high Reynolds and a low Reynolds expression, which have both been derived from their numerical results :

$$\Delta C_D^W (\text{Re} \gg 1) \approx \Delta C_{Du}^W (\text{Re} \gg 1) + \Delta C_{D\omega}^U (\text{Re} \gg 1) + \Delta C_{D\omega}^{W-U} (\text{Re} \gg 1) \quad (4.75)$$

$$\Delta C_{Du}^W (\text{Re} \gg 1) \approx 0.47 L_R^{-4} + 5.5 \times 10^{-3} L_R^{-6} \text{Re}^{3/4} \quad (4.76)$$

$$\Delta C_{D\omega}^U (\text{Re} \gg 1) \approx 2 \times 10^{-3} |\text{Sr}|^{1.9} \text{Re} \quad (4.77)$$

$$\Delta C_{D\omega}^{W-U} (\text{Re} \gg 1) \approx 0.05 L_R^{-7/2} \text{Sr} \text{Re}^{1/3} \quad (4.78)$$

LIFT COEFFICIENT : The total lift coefficient C_L^W is expressed as :

$$C_L^W (\text{Re}, \text{Sr}, L_R) = C_{Lu}^W (\text{Re}, \text{Sr}, L_R) + C_{L\omega}^W (\text{Re}, \text{Sr}, L_R) \quad (4.79)$$

which corresponds to the superposition of two contributions being the uniform flow and the shear rate, both in presence of the wall.

$$C_{Lu}^W (\text{Re}, \text{Sr}, L_R) \approx f_L f'_L b^2 (L_R/3)^g C_{Lu}^{\text{W-in}} + c_{T1} \left[C_{Lu}^W (\text{Re} \rightarrow \infty) + c_{T2} \text{Re}^{-1} L_R^{-4} \right] \quad (4.80)$$

$$f_L (L_\omega, \varepsilon) = e^{-0.22\varepsilon^{0.8} L_\omega^{2.5}} \quad (4.81)$$

$$f'_L (L_u) \approx \frac{1}{1 + 0.13 L_u (L_u + 0.53)} \quad (4.82)$$

$$b(\text{Re}) = 1 + \tanh(0.012 \text{Re}^{0.8}) + \tanh(0.07 \text{Re}^{0.8}) \quad (4.83)$$

$$g = -2.0 \tanh(0.01 \text{Re}) \quad (4.84)$$

$$C_{Lu}^{\text{W-in}} = \frac{1}{2} \left(1 + \frac{1}{8} L_R^{-1} - \frac{33}{64} L_R^{-2} \right) \quad (4.85)$$

$$c_{T1} (\text{Re}) = 1 - e^{-0.22 \text{Re}^{0.6}} \quad (4.86)$$

$$C_{Lu}^W (\text{Re} \rightarrow \infty) \approx -\frac{3}{8} L_R^{-4} \left[1 + \frac{1}{8} L_R^{-3} + \frac{1}{6} L_R^{-5} \right] + O(L_R^{-10}) \quad (4.87)$$

$$c_{T2} = 15 \tanh(0.01 \text{Re}) \quad (4.88)$$

$$C_{L\omega}^W (\text{Re}, \text{Sr}, L_R) \approx h'_L C_{L\omega}^U (\text{Re} \ll 1) + c_{T3} (\text{Re}) (1 + I_{WS}) C_{L\omega}^U (\text{Re} \gg 1) \quad (4.89)$$

$$\text{with } c_{T3} (\text{Re}) = 1 - e^{-0.3 \text{Re}} \quad (4.90)$$

$$h'_L (L_\omega, \varepsilon, L_R) = 1 - e^{-\frac{11}{96} \pi^2 \frac{L_\omega}{J_L(\varepsilon)} (1 + \frac{9}{8} L_R^{-1} - \frac{1271}{3520} L_R^{-2})} \quad (4.91)$$

$$J_L(\varepsilon) = J_L(\infty) (1 + 0.2 \varepsilon^{-2})^{-3/2} \text{ with } J_L(\infty) = 2.254 \quad (4.92)$$

$$C_{L\omega}^U (\text{Re} \ll 1) = \frac{8}{\pi^2} \frac{\text{Sr}}{|\text{Sr}|} \varepsilon J_L(\varepsilon) \quad (4.93)$$

$$I_{WS} = a_G L_R^{-7/2} (1 + b_G \text{Re}^{-1/2}) \text{ with } a_G = 0.23 \text{ and } b_G = 13 \quad (4.94)$$

$$C_{L\omega}^U (\text{Re} \gg 1) = \frac{2}{3} \text{Sr} (1 - 0.07 |\text{Sr}|) \frac{1 + 16 \text{Re}^{-1}}{1 + 29 \text{Re}^{-1}} \quad (4.95)$$

4.3 FORCE BALANCE MODELING

4.3.1 General Considerations

When trying to derive the force balance over a bubble, the first step consists of splitting the whole effort experienced by the bubble between different contributions depending on their nature. In our case, we

focus on a bubble growing on a vertical wall and facing an upward flow as depicted in Figure 4.3. The considered forces are:

- The Buoyancy force $\overline{F_B}$, including Archimedes force and the weight of the bubble ;
- The Capillary or Surface Tension force $\overline{F_C}$;
- The Contact Pressure force $\overline{F_{CP}}$;
- The Drag and Lift forces $\overline{F_D}$ and $\overline{F_L}$;
- The Inertia force, including Added-Mass and Tchen force $\overline{F_I}$.

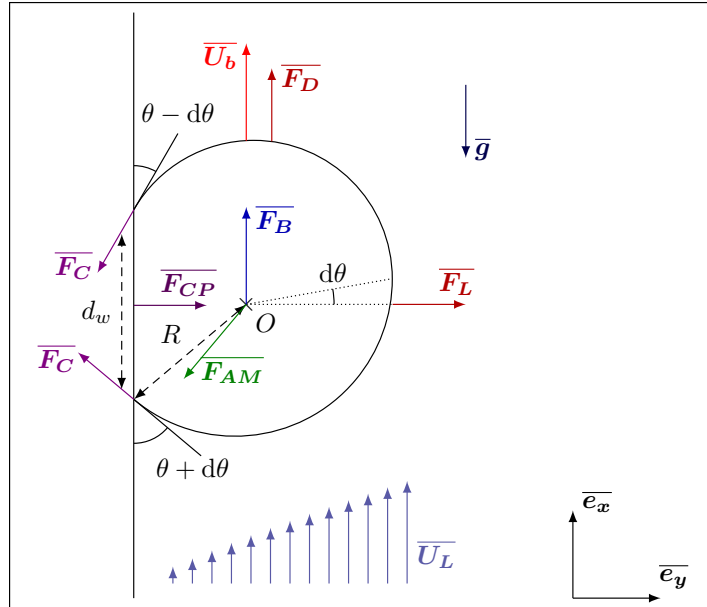


Figure 4.3: Sketch of the forces applied to the bubble facing an upward flow $\overline{U_L}$ and sliding at velocity $\overline{U_b}$

Regarding the bubble shape, we consider a quasi-spherical bubble of radius R with a circular contact area with the wall of radius r_w . It has a static contact angle θ and is tilted under the influence of the flow by an inclination angle $d\theta$ (half the total angle hysteresis). The resulting downstream and upstream contact angles are therefore $\theta_d = \theta - d\theta$ and $\theta_u = \theta + d\theta$. If the bubble has a shape close to a truncated sphere, we can approximate the bubble foot radius as:

$$r_w \approx R \sin \left(\frac{\theta_u + \theta_d}{2} \right) = R \sin (\theta) \quad (4.96)$$

We suppose $V_b \approx \frac{4}{3}\pi R^3$ for the bubble volume.

4.3.2 Buoyancy Force

The Buoyancy force results from both the weight of the bubble and the integration of the static liquid pressure over its surface which naturally yields:

$$\overline{F_B} = V_b (\rho_V - \rho_L) \overline{g} = \frac{4}{3}\pi R^3 (\rho_L - \rho_V) g \overline{e_x} \quad (4.97)$$

4.3.3 Capillary Force

The most common and generally accepted expression of the capillary force has been derived by Klausner [klausner_vapor_1993] by integrating the tangential effort at the triple contact line over the bubble foot radius while assuming an evolution of the contact angle from θ_d to θ_u as a polynomial expression of degree 3. This results in:

$$\begin{aligned}\overline{F_C} = & -\pi R \sigma \left[2.5 \frac{r_w}{R} \frac{d\theta}{(\frac{\pi}{2})^2 - d\theta^2} \sin(\theta) \cos(d\theta) \right] \overline{e_x} \\ & - \pi R \sigma \left[2 \frac{r_w}{R} \sin(\theta) \frac{\sin(d\theta)}{d\theta} \right] \overline{e_y}\end{aligned}\quad (4.98)$$

4.3.4 Contact Pressure Force

The Contact Pressure force is linked to the overpressure inside the bubble. Combined with the Archimedes force, it can be expressed versus the difference of liquid and vapor pressure at the bubble foot using Laplace's equation as:

$$\overline{F_{CP}} \approx \frac{2\sigma}{R_c} \pi r_w^2 \overline{e_y} \approx \pi R \sigma 2 \sin(\theta)^2 \overline{e_y} \quad (4.99)$$

Here, R_c is the curvature radius of the bubble which is often assumed to be equal to $5R$ [klausner_vapor_1993, sugrue_modified_2016, mazzocco_reassessed_2018] without other explanation than avoiding an overestimation of the Contact Pressure force. To avoid this arbitrary choice, following the hypothesis of a nearly spherical bubble shape gives $R_c = R$.

4.3.5 Drag and Lift Forces

The external liquid flow over the bubble induces the well-known Drag and Lift forces, acting respectively in the flow direction and perpendicular to the flow. They are usually expressed using associated coefficients C_D and C_L defined by:

$$\overline{F_D} = \frac{1}{2} C_D \rho_L S_p \|\overline{U_L} - \overline{U_b}\| (\overline{U_L} - \overline{U_b}) \quad (4.100)$$

$$\overline{F_L} = \frac{1}{2} C_L \rho_L S_p \|\overline{U_L} - \overline{U_b}\|^2 \overline{e_y} \quad (4.101)$$

with $S_p = \pi R^2$ the projected area of the bubble in the direction of the flow.

Traditional approaches rely on expressions of the Drag force for a bubble in an infinite medium based on numerical correlations as proposed by Mei [mei_unsteady_1992]:

$$C_{D,U} = \frac{16}{Re_b} \left[1 + \left(\frac{8}{Re_b} + \frac{1}{2} \left(1 + \frac{3.315}{\sqrt{Re_b}} \right) \right)^{-1} \right] \quad (4.102)$$

Results from DNS conducted by Eames *et al.* [eames_lift_2008] proposed expressions of the Drag and Lift forces for a hemispherical bubble on a wall facing a viscous shear flow. Earlier, Legendre & Magnaudet [legendre_lift_1998] analytically derived coefficients to transpose Drag and Lift expressions for a particle to the case of a bubble. This was applied by Mazzocco *et al.* [mazzocco_reassessed_2018] to the Drag for a solid particle near a wall in a shear flow proposed by Zeng *et al.* [zeng_forces_2009]. In this work, we propose to rely on the recent work of Shi *et al.* [shi_drag_2021] who conducted DNS of a shear flow over a spherical bubble of constant radius close to a wall for bubble Reynolds number between 10^{-1} and 10^3 and shear rates between -0.5 and 0.5.

They computed the resulting Drag and Lift coefficients for each simulations and proposed correlations fitting their numerical results. The total Drag coefficient is expressed as a correction of the Drag coefficient for a bubble in an unbounded uniform flow $C_{D,U}$. The total drag is given by:

$$C_D = (1 + \Delta C_D) C_{D,U} \quad (4.103)$$

where ΔC_D accounts for both the effect of the shear flow and the wall vicinity.

To cover the whole range of bubble Reynolds numbers, correlations at low and high Re_b are smoothly connected using an exponential term.

$$\Delta C_D = \Delta C_{D,Re_b=O(1)} + \left(1 - e^{-0.07Re_b}\right) \Delta C_{D,Re_b \gg 1} \quad (4.104)$$

Each of those corrections is computed depending on Re_b , the non-dimensional shear rate Sr , the non-dimensional distances $L_R = \frac{y}{R}$ and $L_u = y \frac{|U_{rel}|}{\nu_L}$ ($L_R = 1$ being a spherical bubble laying on a wall).

$$\begin{aligned} \Delta C_{D,Re_b=O(1)} &= \frac{1 + \tanh(0.012Re_b^{0.8}) + \tanh(0.07Re_b^{0.8})^2}{1 + 0.16L_u(L_u + 4)} \\ &\times \left[\left(\frac{3}{8}L_R^{-1} + \frac{3}{64}L_R^{-4} \right) \left(1 - \frac{3}{8}L_R^{-1} - \frac{3}{64}L_R^{-4} \right)^{-1} \right. \\ &\quad \left. - \frac{1}{16} \left(L_R^{-2} + \frac{3}{8}L_R^{-3} \right) Sr \right] \end{aligned} \quad (4.105)$$

$$\begin{aligned} \Delta C_{D,Re_b \gg 1} &= 0.47L_R^{-4} + 0.0055L_R^{-6}Re_b^{3/4} + 0.002|Sr|^{1.9}Re_b \\ &\quad + 0.05L_R^{-7/2}SrRe_b^{1/3} \end{aligned} \quad (4.106)$$

Figure 4.4 shows the evolution of the Drag correction ΔC_D against the bubble Reynolds number for different distances to the wall L_R and two values of Sr . We can see that as the distance between the wall and the bubble increases the Drag correction logically approaches zero and that increasing the shear rate Sr increases ΔC_D for higher values of Re_b .

Shi *et al.* [shi_drag_2021] conducted DNS for wall distances down to $L_R = 1.5$. However, Scheiff *et al.* [scheiff_experimental_2021] compared the values obtained for $L_R = 1$ with measured Drag coefficients of bubbles sliding on a wall and observed a good agreement, which legitimates the use of this new Drag correlation by extending its application to the case of a bubble laying on a wall and using the uniform drag coefficient of Eq. 4.102.

Since this work focuses on the sliding, the total force balance will be studied along the x axis, parallel to the wall. Thus, we do not detail the whole expression of Shi *et al.* for C_L . For further work, it is though interesting to mention that their expression of C_L is based on the sum of three contributions (wall presence, shear and a coupled term) and changes sign when reaching negative values or Sr for instance.

4.3.6 Inertia Force

The Inertia force originates from various effects (bubble growth, freestream and bubble acceleration, etc.) that includes both Added Mass and Tchen forces and is expressed as [magnaudet_motion_2000]:

$$\overline{F_I} = \underbrace{\rho_L V_b \left(\frac{\partial \overline{U}_L}{\partial t} + \overline{\nabla}(U_L) \cdot \overline{U}_L \right)}_{\text{Liquid inertia or Tchen force}} + \underbrace{\frac{d}{dt} (\rho_L C_{AM} V_b (\overline{U}_L - \overline{U}_b))}_{\text{Added Mass force } \overline{F_{AM}}} \quad (4.107)$$

Since we consider a steady and quasi-parallel liquid flow, the inertia term is equal to zero.

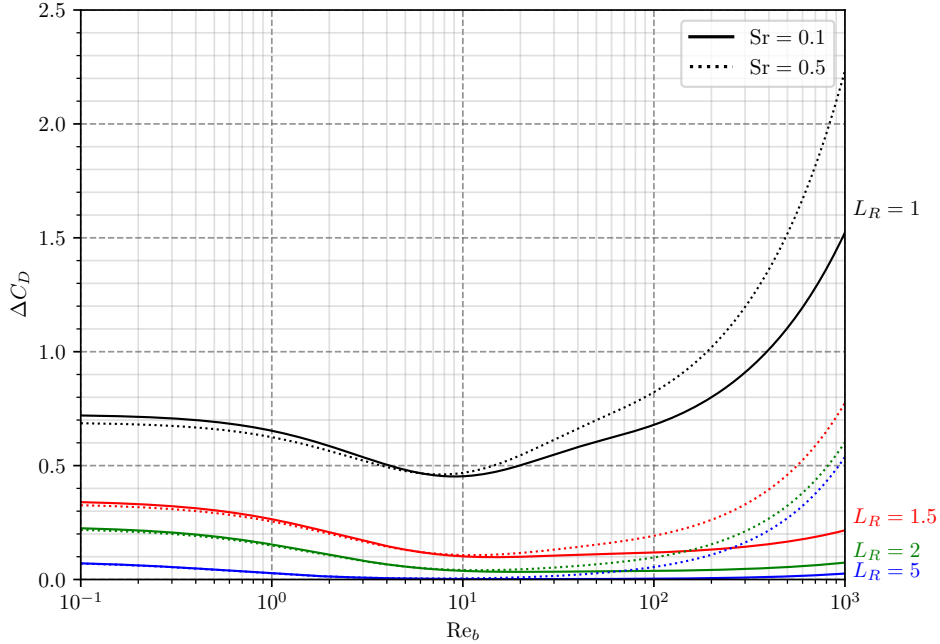


Figure 4.4: Drag correction from Shi *et al.* [shi_drag_2021].

4.3.6.1 Former Approaches

In previous Mechanistic Models, the derivation of the Added Mass force was conducted with different approaches. In particular, some authors have chosen to rely on the Rayleigh-Plesset Equation for a growing hemispherical bubble in a quiescent flow to obtain the reaction force from the liquid, oriented perpendicularly to the wall.

$$\overline{F_{AM,RPE}} = -\rho_L \pi R^2 \left[R \ddot{R} + \frac{3}{2} \dot{R}^2 \right] \overline{e_y} \quad (4.108)$$

Then, assuming a bubble inclination angle θ_i , this force is projected along the x axis to obtain an Added Mass force parallel to the wall that hinders departure. The inclination angle value is often empirical and used for data fitting [zeng_unified_1993-1, colombo_prediction_2015, mazzocco_reassessed_2018, ren_development_2020].

$$\overline{F_{AM,RPE}} = -\rho_L \pi R^2 \left[R \ddot{R} + \frac{3}{2} \dot{R}^2 \right] (\sin(\theta_i) \overline{e_x} + \cos(\theta_i) \overline{e_y}) \quad (4.109)$$

This approach is questionable on different aspects. First, the RPE assumes a moving boundary in a quiescent unbounded liquid, which is physically far from the real situation of a bubble growing on a wall in a boiling flow. Moreover, the subsequent projection along the different directions regarding an unknown angle is hardly reasonable if θ_i is chosen arbitrarily.

On the other hand, some authors [klausner_vapor_1993, thorncroft_bubble_2001, guan_bubble_2015] considered two distinct contributions:

- Hemispherical bubble growth in a stagnant liquid, leading to Eq. 4.109 including the inclination angle θ_i ;
- Spherical bubble growth in an uniform unbounded and inviscid liquid flow, which yields a detaching Added Mass term due to the interaction of bubble growth with the external flow:

$$\overline{F_{AM,U}} = \frac{3}{2} \rho_L V_b \frac{\dot{R}}{R} U_L \overline{e_x} \quad (4.110)$$

By including the effect of the liquid flow, this approach can be considered as closer to the reality. However, it relies on two separate derivations associated to different physical considerations.

4.3.6.2 Proposed Approach

To tackle the Added Mass derivation in a proper way, we propose to follow the approach of Lamb [lamb_hydrodynamics_1895] (also presented by Milne Thomson [milne-thomson_theoretical_1938] or Van Winjaarden [wijngaarden_hydrodynamic_1976]). By solving the potential flow around a bubble and its image, we can obtain the total liquid kinetic energy E_L that corresponds to a situation where a bubble is at a given distance from a wall (represented by the line normal to the line of centers of the bubbles).

Then, using Lagrange's equations to compute the resulting forces in each direction:

$$F_{AM,x} = -\frac{\partial}{\partial t} \left(\frac{\partial E_L}{\partial \dot{x}} \right) + \frac{\partial E_L}{\partial x} \quad (4.111)$$

$$F_{AM,y} = -\frac{\partial}{\partial t} \left(\frac{\partial E_L}{\partial \dot{y}} \right) + \frac{\partial E_L}{\partial y} \quad (4.112)$$

To express the liquid kinetic energy, we can rely on the work of Van Der Geld [van_der_geld_dynamics_2009] who derived E_L in the case of a full or truncated spherical bubble laying on a wall and facing an uniform flow parallel to the wall of velocity U_L (Eq. 4.113). If the bubble slides at a velocity $U_b = \dot{x}$, it sees a liquid velocity $U_{rel} = U_L - \dot{x}$.

$$E_L = \frac{\rho_L V_b}{2} \left(\alpha \dot{y}^2 + \text{tr}(\beta) \dot{R}^2 + \psi \dot{R} \dot{y} + \alpha_2 (U_L - \dot{x})^2 \right) \quad (4.113)$$

where (x, y) are the coordinates of the bubble's center and α , $\text{tr}(\beta)$, ψ , α_2 are polynomials of $R/y = 1/L_R$ derived by Van Der Geld for $1 < R/y < 2$ i. e. $0.5 < L_R < 1$.

Injecting E_L in Eq. 4.111 and 4.112 and computing the values for the sphere case ($y = R$ and $\dot{y} = \dot{R}$) yields:

$$F_{AM,x} = \rho_L V_b \left[3C_{AM,x} \frac{\dot{R}}{R} U_{rel} - C_{AM,x} \frac{\partial U_b}{\partial t} \right] \quad (4.114)$$

with $C_{AM,x} \approx 0.636$.

$$F_{AM,y} = \rho_L V_b \left[-(3C_{AM,y1} + C_{AM,y2}) \frac{\dot{R}^2}{R} - C_{AM,y1} \dot{R} + C_{AM,y3} \frac{U_{rel}^2}{R} \right] \quad (4.115)$$

with $C_{AM,y1} \approx 0.27$, $C_{AM,y2} \approx 0.326$ and $C_{AM,y3} \approx 8.77 \times 10^{-3}$.

Parallel to the wall, the coupled term $\frac{\dot{R}}{R} U_{rel}$ in Eq. 4.114 promotes detachment and sliding of the bubble if $U_{rel} > 0$ e. g. if the bubble is attached to its nucleation site. This relatively agrees with the detaching term of the "two situations" derivations detailed in 4.3.6.1 and clearly contradicts the aforementioned approach where solely projecting the RPE on both axes lead to an Added-Mass term related to bubble growth that only hinders the departure by sliding.

Moreover, Eq. 4.115 exhibits a term induced by the relative velocity that acts as a lift force, which seems to rarely appear in other approaches.

Here we want to insist on the importance on conducting an approach as rigorous as possible when deriving those transient aspects of the force balance. Otherwise, some terms may be missing and lead to contradictory physical conclusions. Although the proposed method has already been used in different

works, we obtained revisited values of the Added Mass coefficients based on the derivation of the liquid kinetic energy by Van Der Geld.

In the spirit of avoiding to introduce extra empirical terms, we keep the Added Mass force as presented in Eq. 4.114 and 4.115. No projection of the y term along the x axis to account for asymmetric bubble growth is considered in this study.

4.3.7 Force Balance Summary

On Table 4.2, we sum up some of the mentioned force balance approaches and their models.

	Klausner [klausner_vapor_1993] (1993)	Thorncroft [thorncroft_bubble_2001] (2001)	Sugrue [sugrue_modified_2016] (2016)
Forces	$\overline{F_B}$ $\frac{4}{3}\pi R^3 (\rho_L - \rho_V) \bar{g}$	$\frac{4}{3}\pi R^3 (\rho_L - \rho_V) \bar{g}$	$\frac{4}{3}\pi R^3 (\rho_L - \rho_V) \bar{g}$
	$\overline{F_C}$ Eq. 4.98, $r_w = 0.045$ mm	Eq. 4.98, $r_w = R \sin(\theta_d)$	Eq. 4.98, $r_w = 0.025R$
	$\overline{F_{CP}}$ Eq. 4.99, $R_c = 5R$	Neglected	Eq. 4.99, $R_c = 5R$
	$\overline{F_D}$ $C_D = \frac{16}{Re_b} \left[1 + \frac{3}{2} \left(\left(\frac{12}{Re_b} \right)^n + 0.796^n \right)^{1/n} \right], n = 0.65$	$C_D = \frac{16}{Re_b} \left[1 + \left(\frac{8}{Re_b} + \frac{1}{2} \left(1 + \frac{3.315}{\sqrt{Re_b}} \right) \right)^{-1} \right]$	$C_D = \frac{16}{Re_b} \left[1 + \frac{3}{2} \left(\left(\frac{12}{Re_b} \right)^n + 0.796^n \right)^{1/n} \right], n = 0.65$
	$\overline{F_L}$ $C_L = 2.74\sqrt{Sr}$ $\times \left[Re_b^{-2} + \left(0.24\sqrt{Sr} \right)^4 \right]^{\frac{1}{4}}$	$C_L = 0.71\sqrt{Sr}$ $\times \left[\left(\frac{1.15J(\varepsilon)}{\sqrt{Re_b}} \right)^2 + \left(\frac{3\sqrt{2Sr}}{8} \right)^2 \right]^{\frac{1}{2}}$	$C_L = 2.74\sqrt{Sr}$ $\times \left[Re_b^{-2} + \left(0.24\sqrt{Sr} \right)^4 \right]^{\frac{1}{4}}$
	$\overline{F_{AM}}$ $\frac{3}{2}\rho_L V_b \frac{\dot{R}}{R} U_L \bar{e}_x - \rho_L \pi R^2 \left(\frac{3}{2}\dot{R}^2 + R\ddot{R} \right)$ $\times (\cos(\theta_i) \bar{e}_y + \sin(\theta_i) \bar{e}_x), \theta_i = 10^\circ$	$2\pi\rho_L R^2 \dot{R} U_L \bar{e}_x - \rho_L \pi R^2 \left(\frac{3}{2}\dot{R}^2 + R\ddot{R} \right)$ $\times (\cos(\theta_i) \bar{e}_y + \sin(\theta_i) \bar{e}_x), \theta_i = 45^\circ$	$-\rho_L \pi R^2 \left(\frac{3}{2}\dot{R}^2 + R\ddot{R} \right)$ $\times (\cos(\theta_i) \bar{e}_y + \sin(\theta_i) \bar{e}_x), \theta_i = 10^\circ$
Forces	Mazzocco [mazzocco_reassessed_2018] (2018)	Ren (2020) [ren_development_2020]	Present model
	$\overline{F_B}$ $\frac{4}{3}\pi R^3 (\rho_L - \rho_V) \bar{g}$	$\frac{4}{3}\pi R^3 (\rho_L - \rho_V) \bar{g}$	$\frac{4}{3}\pi R^3 (\rho_L - \rho_V) \bar{g}$
	$\overline{F_C}$ Eq. 4.98, $r_w = R/15$	Eq. 4.98, $r_w = 0.2R$	Eq. 4.98, $r_w = R \sin(\theta)$
	$\overline{F_{CP}}$ Eq. 4.99, $R_c = 5R$	Eq. 4.99, $R_c = 5R$	Eq. 4.99, $R_c = R$
	$\overline{F_D}$ $C_D = 1.13 \frac{24}{Re_b} \left(1 + 0.104 Re_b^{0.753} \right)$	$C_D = \frac{16}{Re_b} \left[1 + \frac{3}{2} \left(\left(\frac{12}{Re_b} \right)^n + 0.796^n \right)^{1/n} \right], n = 0.65$	$C_D = C_{D,U} (1 + \Delta C_D)$ $C_{D,U}$ by Eq. 4.102, ΔC_D by Eq. 4.104
	$\overline{F_L}$ $C_L = 2.61$	$C_L = 2.74\sqrt{Sr}$ $\times \left[Re_b^{-2} + \left(0.24\sqrt{Sr} \right)^4 \right]^{\frac{1}{4}}$	C_L by Shi <i>et al.</i> [shi_drag_2021]
F_{AM}	$-\frac{1}{4}\pi\rho_L K^4 (\cos(\theta_i) \bar{e}_y + \sin(\theta_i) \bar{e}_x),$ $\sin(\theta_i) = 0.2, \cos(\theta_i) = 1$	$-\rho_L \pi R^2 \left(\frac{3}{2}\dot{R}^2 + R\ddot{R} \right)$ $\times (\cos(\theta_i) \bar{e}_y + \sin(\theta_i) \bar{e}_x), \theta_i = 15^\circ$	$\frac{F_{AM,x}}{\rho_L V_b} = C_{AM,x} \left[3 \frac{\dot{R}}{R} U_{rel} - \frac{\partial U_b}{\partial t} \right],$ $C_{AM,x} = 0.636, F_{AM,y}$ by Eq. 4.115.

Table 4.2: Summary of different force-balance mechanistic approaches.

4.3.8 Bubble Growth

The question of the bubble growth law during its lifetime including sliding is still an open question that aims to cover various types of heat transfer mechanisms:

- Evaporation due to superheated liquid near the bubble base ;
- Evaporation of a liquid microlayer trapped between the base of the bubble and the wall ;
- Condensation on top of the bubble when it reaches subcooled liquid ;
- Convective heat transfer due to relative velocity between the bubble and the liquid.

To our knowledge, many authors that have been tackling this issue had to consider empirical or fitted parameters when trying to exhaustively account for all the above heat transfers. For instance, Zhou [zhou_experimental_2020] and Yoo [yoo_development_2018] have proposed growth models that consider all the previously mentioned mechanisms. However, to fully close their mathematical model, many empirical values were used such as:

- The ratio between the bubble projected area and the microlayer area ;
- The fraction of bubble area facing subcooling liquid ;
- Value of coefficients in the condensation law [levenspielCollapse_1959].

Moreover, those models postulate the existence of a microlayer contributing to the growth while recent numerical and experimental investigations showed that the bubble may as well grow with a microlayer or in a pure contact line regime depending on the operating conditions [urbanoDirect_2018, buresModelling_2021, kossolapovExperimental_2021].

In order to assess the force modeling proposed before, we choose a simpler growth law derived from heat conduction in the superheated liquid layer [plesssetGrowth_1954].

$$R(t) = K \text{Ja}_w \sqrt{\eta_L t} \quad (4.116)$$

where K is an adjustable constant, with an upper bound around 2 for a spherical bubble in a quiescent unbounded superheated liquid [plesssetGrowth_1954, yunPrediction_2012]. This value can thus be lower in the case of subcooled flow boiling. For instance, later comparisons with experimental measurements suggest values of K slightly below 1 for subcooled flow boiling (Figure 4.11).

This type of bubble growth has been widely used, and showed good agreement with many experimental observations and is particularly valid for early growth stages or small bubbles at high pressure.

4.3.9 Liquid Velocity

To compute the liquid velocity and shear rate at bubble center height, we use the wall law of Reichardt [reichardtVollstandige_1951], which describes the velocity profile from the viscous sublayer to the logarithmic region.

$$\begin{aligned} U_L^+ &= \frac{1}{\kappa} \ln(1 + \kappa y^+) + c \left(1 - e^{-y^+/\chi} + \frac{y^+}{\chi} e^{-y^+/3} \right) \\ U_L &= U_L^+ U_\tau \end{aligned} \quad (4.117)$$

with $\kappa = 0.41$, $\chi = 11$ and $c = 7.8$.

$$\begin{aligned} \frac{\partial U_L^+}{\partial y^+} &= \frac{1}{1 + \kappa y^+} + \frac{c}{\chi} \left(e^{-y^+/\chi} + \left(1 - \frac{y^+}{3} \right) e^{-y^+/3} \right) \\ \frac{\partial U_L}{\partial y} &= \gamma = \frac{U_\tau^2}{\nu_L} \frac{\partial U_L^+}{\partial y^+} \end{aligned} \quad (4.118)$$

The friction velocity is computed using Mac Adams correlation [mcadamsHeat_1954].

$$U_\tau = \sqrt{\frac{\tau_w}{\nu_L}} \quad (4.119)$$

$$\tau_w = 0.018 \text{ Re}_{D_h}^{-0.182} \frac{G_L^2}{\rho_L} \quad (4.120)$$

4.4 DEPARTURE BY SLIDING

4.4.1 Non-Dimensional Analysis

Now that the force balance has been established, we can write it parallel to the wall before bubble departure by sliding *i.e.* $U_b = \frac{\partial U_b}{\partial t} = 0$.

$$-\pi R \sigma f_{C,x} + \frac{4}{3} \pi R^3 (\rho_L - \rho_V) g + \frac{1}{2} C_D \rho_L \pi R^2 U_L^2 + \frac{4}{3} \pi R^3 \rho_L 3 C_{AM,x} \frac{\dot{R}}{R} U_L = 0 \quad (4.121)$$

$$f_{C,x} = 2.5 \frac{d\theta}{(\pi/2)^2 - d\theta^2} \sin(\theta)^2 \cos(d\theta) \quad (4.122)$$

with $f_{C,x} \rightarrow 0$ if $d\theta \rightarrow 0$.

We can note that the departure by sliding is promoted by the Buoyancy, the Drag and the Added Mass forces. Only the Capillary force keeps the bubble attached to its nucleation site, which will be discussed later.

Re-writing Eq. 4.121 in non-dimensional form by dividing the LHS by the Added Mass force yields:

$$-\frac{1}{2} \frac{f_{C,x}}{K^2 C_{AM,x}} \frac{1}{Ca} \frac{Pr_L}{Ja_w^2} + \frac{1}{3} \frac{1}{K^2 C_{AM,x}} \frac{Re_b}{Fr} \frac{Pr_L}{Ja_w^2} + \frac{1}{8} \frac{C_D}{K^2 C_{AM,x}} Re_b \frac{Pr_L}{Ja_w^2} + 1 = 0 \quad (4.123)$$

where we have the following non-dimensional numbers:

$$Re_b = \frac{2 R U_L}{\nu_L} ; Fr = \frac{\rho_L U_L^2 R}{(\rho_L - \rho_V) g R} ; We = \frac{\rho_L U_L^2 R}{\sigma} ; Eo = \frac{(\rho_L - \rho_V) g R^2}{\sigma} ; \\ Ja_w = \frac{(T_w - T_{sat}) \rho_L c_{P,L}}{\rho_V h_{LV}} ; Pr_L = \frac{\nu_L}{\eta_L} ; \frac{\dot{R}}{U_L} = \frac{K^2 Ja_w^2}{Pr_L Re_b} ; Ca = \frac{\mu_L U_L}{\sigma}$$

Eq. 4.123 exhibits terms that can be used to compare the magnitude of each detaching forces. We can obtain the following conditions:

$$\text{Added Mass greater than Drag if: } \frac{Ja_w^2}{Pr_L} > \frac{1}{8} \frac{C_D}{C_{AM,x}} \frac{1}{K^2} Re_b \quad (4.124)$$

$$\text{Added Mass greater than Buoyancy if: } \frac{Ja_w^2}{Pr_L} > \frac{1}{3} \frac{1}{C_{AM,x} K^2} \frac{Re_b}{Fr} \quad (4.125)$$

$$\text{Drag greater than Buoyancy if: } Re_b > \frac{16}{3} \frac{1}{C_D} \frac{Eo}{Ca} = Re_c \quad (4.126)$$

Those boundaries can be plotted on a $(Ja_w^2/Pr ; Re_b)$ map for a given fluid and bubble diameter D . An example of such a map is presented on Figure 4.5. This allows to visualize the operating conditions under which each of the detaching forces will be dominant. Logically, Buoyancy dominates for low Re_b regimes contrary to Drag. Added Mass dominates when values of Ja_w^2/Pr_L are high *i.e.* when bubble grows rapidly.

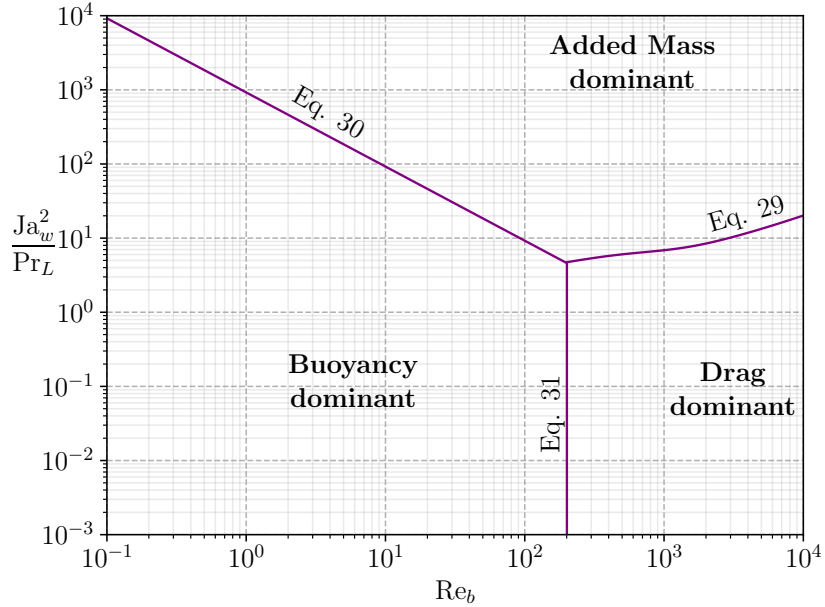


Figure 4.5: Dominance map regarding departure by sliding. Boundaries plotted for water at 1 bar and $D_d = 0.5\text{mm}$. ($K = 2$)

4.4.1.1 Influence of Pressure

On Figure 4.6a, we draw the dominance map for 3 different pressures and associated orders of magnitude of bubble departure diameter [kocamustafaogullari_pressure_1983].

The impact of pressure is mostly seen through the decrease of bubble departure diameter. As pressure increases, Buoyancy force decreases while Drag and Added Mass forces display much larger dominance zones. The competition between those two terms mainly relies on the competition between liquid flow velocity and wall superheat or heat flux.

4.4.1.2 Comparison between Fluids

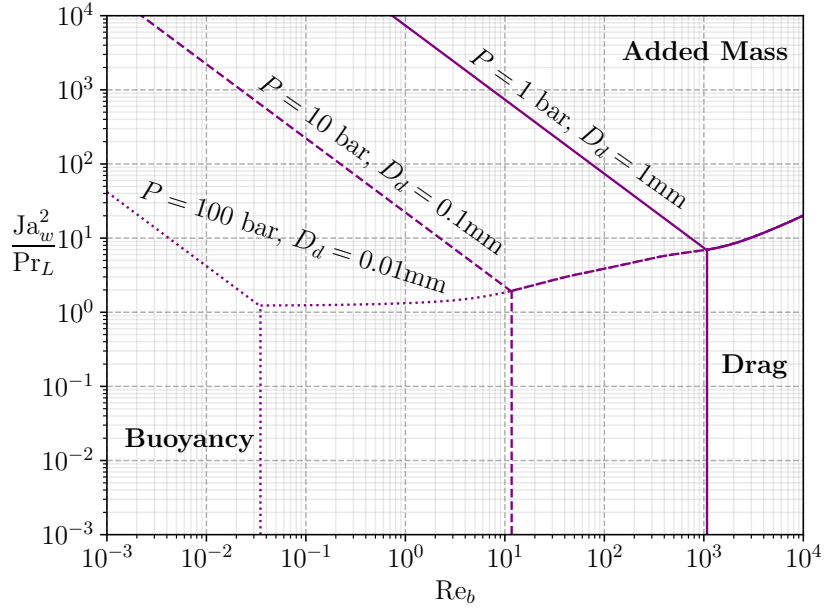
On Figure 4.6b, we compare the dominance zones for R12 at 26 bar and water at 155 bar. Moderately pressurized R12 (10 to 30 bar) has often been used as a simulating fluid to mimic water in PWR since it has the same density ratio and Weber number for instance.

Assuming that the conservation of Weber and Boiling numbers may lead to similar bubble departure diameters, we can observe that the boundaries between the two fluids are very close. This qualitatively indicates that R12 shall present bubble departure by sliding mechanisms similar to what happens in PWR, which could comfort the confidence one may have in extrapolating the observations done using the simulating fluid to industrial applications.

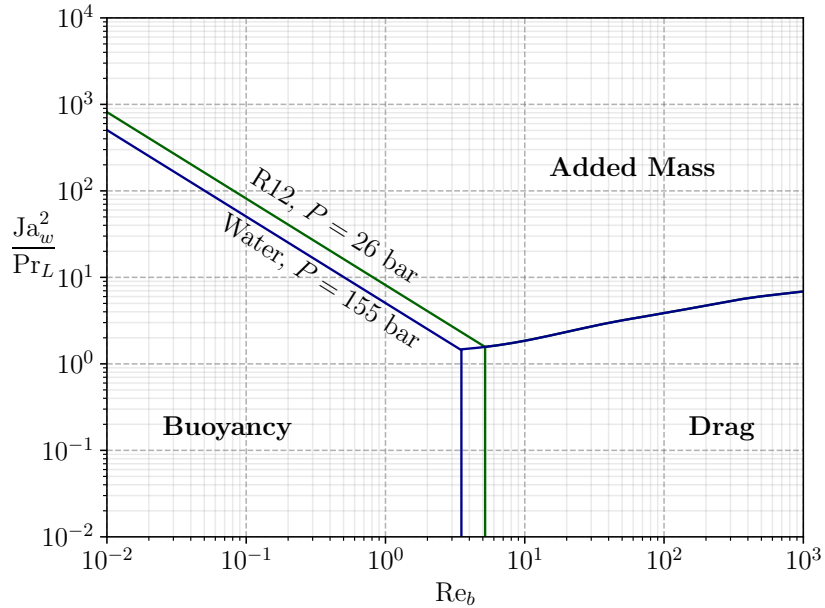
4.4.2 Application to Experimental Data

Now we want to apply this non-dimensional approach to experimental measurement in order to determine the actual bubble departure by sliding regimes. We rely on 7 experiments in which bubble departure diameters in vertical flow boiling were measured. The operating conditions are gathered in Table 4.3. If the value of ΔT_w is not available in the considered data-set, we estimate it ΔT_w using Frost & Dzakowic correlation [frost_extension_1967].

$$\Delta T_w = Pr_{L,sat} \sqrt{\frac{8\sigma\phi_w T_{sat}}{\lambda_L \rho_V h_{LV}}} \quad (4.127)$$



(a) Dominance map plotted for water at different pressures and bubble departure diameters. ($K = 2$)



(b) Dominance map for R12 as simulating fluid for PWR. $D_d = 0.05\text{mm}$ is chosen according to R12 measurements from Garnier *et al.* [garnier_local_2001] who observed bubbles of $\sim 0.1\text{mm}$ diameter after lift-off. ($K = 2$)

Figure 4.6: Examples of qualitative analysis using the non-dimensional regime map

Comparisons with bubble growth profile from Kossolapov [kossolapov_experimental_2021] showed that values of K respectively around 7 and 15 were needed to match experimental measurements at 20 bar and 40 bar. This means Eq. 4.127 probably underestimates the wall superheat on those cases. We will thus further adopt a corrective factor of 7 at 20 bar and 15 at 40 bar to use more realistic values of K .

Author	Fluid	D_h [mm]	P [bar]	G_L [kg/m ² /s]	ΔT_L [K]	ϕ_w [kW/m ²]	ΔT_w [K]	D_d [mm] (N_{mes})
Thorncroft [thorncroft_experimental_1998] (1998)	FC-87	12.7	N.A.	0 - 319	0.99 - 3.27	2.83 - 11.8	0.54 - 6.89	0.094 - 0.237 (10)
Maity [maity_effect_2000] (2000)	Water	20	1.01	0 - 239.6	0.3 - 0.7	N.A.	5 - 5.9	0.788 - 1.71 (9)
Chen [chen_prediction_2012] (2012)	Water	3.8	1.2 - 3.35	214 - 702	14.5 - 30.3	83.6 - 334	N.A.	0.549 - 2.255 (22)
Sugrue [sugrue_modified_2016] (2014)	Water	16.6	1.01	250 - 400	10 - 20	50 - 100	2 - 6	0.229 - 0.391 (16)
Guan [guan_bubble_2015] (2014)	Water	9	1.01	87.3 - 319.2	8.5 - 10.5	68.2 - 104	4.5 - 8.5	0.62 - 1.85 (12)
Ren [ren_development_2020] (2020)	Water	3.8	2 - 5.5	488.4 - 1654	28.7 - 51	160.7 - 643.2	N.A.	0.045 - 0.111 (42)
Kossolapov [kossolapov_experimental_2021] (2021)	Water	11.8	19.9 - 39.8	500 - 1500	10	178 - 613	N.A.	0.01 - 0.047 (11)

Table 4.3: Bubble departure diameters data sets in vertical flow boiling

To place experimental measurements on the non-dimensional map, we need a bubble detachment diameter value D_d to plot the dominance zones. Since measured D_d vary significantly in each experiment, we draw the boundaries for the maximum and minimum values of D_d as shown on Figure 4.7a. If the considered data covers different pressures, boundaries for each pressure are plotted to exhibit its impact (Figures 4.7d, 4.7e and 4.7f). We chose a value of $K = 1$ to draw the boundaries.

The Figure 4.7 shows that for most of the low pressure experiments, the detaching forces are the Added Mass and the Buoyancy. Smaller bubbles are mainly detached under the effect of the Added Mass force (Figures 4.7c, 4.7d and 4.7e). When the bubbles detach at higher diameters, the impact of the Buoyancy force naturally increases and is comparable to the Added Mass force (Figures 4.7a and 4.7b).

When the pressure increases, we observe that the experimental measurements gradually move towards the Drag dominant zone as seen on Figures 4.7e and 4.7f. This main difference in the dynamic regime when bubble departs by sliding arises from multiple effects:

- The decrease of ρ_L / ρ_V with pressure, thus reducing Jaw and the impact of the detaching Added Mass term ;
- The higher liquid mass fluxes in Kossolapov experiments, increasing the impact of the Drag ;
- The decrease of D_d with pressure, reducing the magnitude of Buoyancy.

However, we see that some measurements lie close to the Added Mass / Drag boundary (Figure 4.7f), indicating that the Added Mass force still plays a significant role for bubble detachment. This means that regardless of the operating pressure, the detaching term associated to the coupling between bubble growth and outer liquid flow should not be neglected in the force balance (Eq. 4.114).

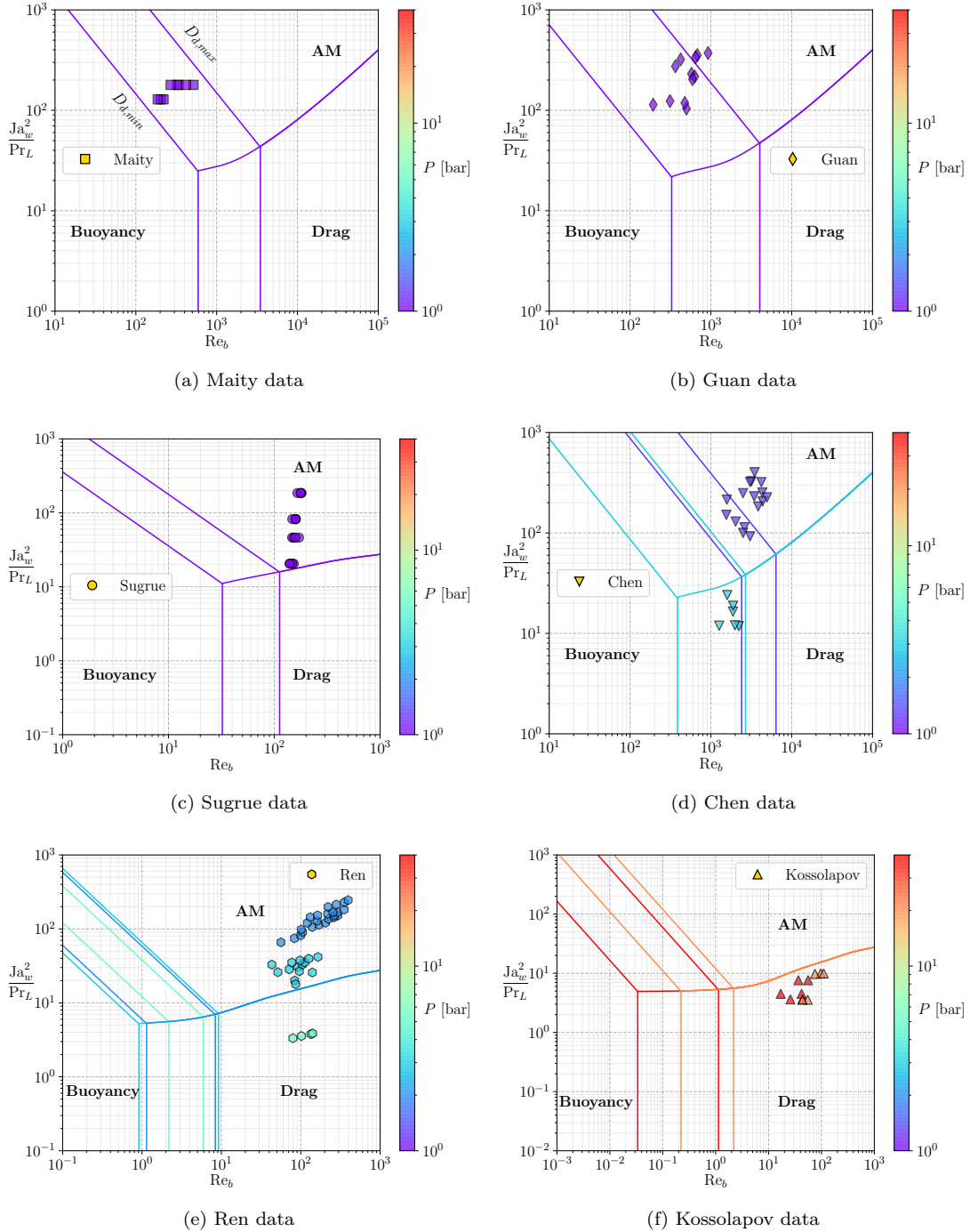


Figure 4.7: Dominance maps for each water data sets from Table 4.3.

4.4.3 Departure Diameter Prediction

4.4.3.1 About the Use of Empiricism

As previously mentioned, the case of bubble detachment in vertical flow boiling is particular since only one force maintains the bubble attached to its nucleation site: the Capillary force (Eq. 4.98). Its expression depends on the contact angle θ , the angle half-hysteresis $d\theta$ and the bubble foot radius r_w

(or ratio to bubble diameter r_w/R) and is thus very sensitive to those values. Paradoxically, those terms are among the least precisely known due to the difficulty of measurement and associated uncertainties. For instance, conducting precise evaluations of the contact angle near the bubble base through optical techniques can be challenging because of the strong temperature gradients close to the heated surface. Consequently, empirical choices have to be made in order to set a value to those parameters, often by relying on data-fitting or approximate measurements in other conditions. For instance, contact angles are often taken as arbitrary average values [[ren_development_2020](#)] or measurements in room conditions [[sugrue_modified_2016](#)] and applied over a whole set of experiments. This is questionable since contact angle is unlikely to remain unchanged over different operating conditions and surfaces with varying roughness and properties [[song_temperature_2021](#)].

However, no better information except those given by the authors can be used to evaluate the Capillary force since no generic model exist to compute the contact angle and hysteresis. In this work, admitting a significant uncertainty (typically 5°, as in Guan [[guan_bubble_2015](#)]), we will use the following values for the contact angles :

- $\theta_u = 25.3^\circ$ and $\theta_d = 6.6^\circ$ for Thorncroft data (measured values for FC-87 on nichrome [[thorncroft_bubble_2001](#)]) ;
- $\theta_u = 50^\circ$ and $\theta_d = 40^\circ$ for Maity data (measured average contact angles for each bubble during its lifetime [[maity_effect_2000](#)]) ;
- $\theta_u = 130^\circ$ and $\theta_d = 65^\circ$ for Chen data (chosen values in their study following measurements for water on stainless steel at high temperature by Kandlikar *et al.* [[kandlikar_contact_2002](#)]) ;
- $\theta_u = 91^\circ$ and $\theta_d = 8^\circ$ for Sugrue data (measured values at room temperature [[sugrue_effects_2012](#)]) ;
- $\theta_u = 75^\circ$ and $\theta_d = 30^\circ$ for Guan data (measured average value through experimental visualizations [[guan_bubble_2015](#)]) ;
- $\theta_u = 45^\circ$ and $\theta_d = 36^\circ$ for Ren data (chosen values in their study [[ren_development_2020](#)]) ;
- $\theta = 80^\circ$ for Kossolapov data (typical contact angle for water on ITO [[kossolapov_experimental_2021](#)]) and $d\theta = 1^\circ$ assuming that the very small bubbles at high pressure are nearly not tilted.

Similarly, the bubble foot radius r_w is often empirically assumed to be either constant [[klausner_vapor_1993](#)] proportional to the bubble radius [[sugrue_modified_2016](#), [mazzocco_reassessed_2018](#)] or to follow a linear or logarithmic law of R [[zhou_experimental_2020](#), [guan_bubble_2015](#)]. That is why we chose to use the truncated sphere hypothesis (Eq. 4.96) to compute r_w using R and θ .

Finally, we would like to acknowledge that the empiricism to evaluate those parameters represents one of the biggest flaws of the force-balance approach. Indeed, such a model aims to detect small sign changes in a sum of a few μN of forces that are decades larger as pointed out by Bucci *et al.* [[bucci_not-so-subtle_2021](#)]. Mechanistic models are thus strongly sensitive to any extra parameter included in the modeling of the forces.

4.4.3.2 Growth Constant Values

Since the value $K \approx 2$ represents an upper bound for the growth constant in a quiescent uniformly superheated liquid [[plesset_growth_1954](#)] and that values below 1 can be a better fit for bubble growth in subcooled flow boiling (Figure 4.11), we propose a simple law that includes an influence of the liquid subcooling and velocity:

$$K = \frac{2}{(1 + \text{Re}_\tau)^{0.3} (1 + \text{Ja}_L)} \quad (4.128)$$

where $\text{Re}_\tau = U_\tau L_c / \nu_L$.

This expression naturally degenerates to $K = 2$ for quiescent saturated liquid and yields values between 0.15 and 1.99 for the cases of Table 4.3.

4.4.3.3 Predictions

We consider the non-dimensional force balance before departure.

$$C_{AM,x}K^2 \frac{Ja_w^2}{Pr_L} + \frac{1}{3} \frac{Re_b}{Fr} + \frac{1}{8} C_D Re_b = \frac{1}{2} \frac{f_{C,x}}{Ca} \quad (4.129)$$

Since we only have the capillary term hindering departure as a first approach, we can suppose that departure is reached when:

$$C_{AM,x}K^2 \frac{Ja_w^2}{Pr_L} + \frac{1}{3} \frac{Re_b}{Fr} + \frac{1}{8} C_D Re_b > \frac{1}{2} \frac{f_{C,x}}{Ca} \quad (4.130)$$

which is similar to considering that the other forces overcome the Capillary force.

On Figure 4.8, we show the predictions obtained with the proposed modeling and those obtained with Mazzocco's recent model [mazzocco_reassessed_2018].

The model have an acceptable trend on some experimental sets, but strong overestimation occur on the cases of Sugrue. Moreover, we observe significant underestimations on the data of Ren at 2 bar and Thorncroft.

Mazzocco's model provides a good accuracy on the data of Sugrue, Guan, Maity and Ren (2 bar). However, we observe very large overestimation over Thorncroft's measurements and significant underestimation on Chen, Ren (3 and 5 bar) and Kossolapov measurements.

4.4.4 Discussion and accounting for parameters uncertainties

The aforementioned errors observed for the proposed model may originate from various reasons:

- The contact angle proposed for Sugrue cases is high with a large hysteresis, suggesting strongly deformed and flattened bubbles under the truncated sphere hypothesis. Based on images from Sugrue's work [sugrue_experimental_2014], a comparison between a real bubble with the assumed shape is presented on Figure 4.9. This shows a huge difference which indicates that the contact angle and hysteresis values may be overestimated. Using the available images, the ratio of the bubble diameter to the apparent bubble foot would lead to an average contact angle $\theta \approx 20^\circ$ for a truncated sphere. Noting that a larger inclination is observed for the bubbles under higher mass fluxes leads us to suppose a value $d\theta \approx 15^\circ$. This represent a similar inclination to contact angle ratio ($d\theta/\theta$) compared to the initially proposed values. The resulting new shape is also presented on Figure 4.9 and seem to better represent the actual bubble.
- For cases where limited under and overestimation is observed, we may allow to account for an uncertainty as high as 5° for the average contact angle θ and half-hysteresis $d\theta$.
- As mentioned earlier, applying the same contact angle and hysteresis over a wide range of measurements is a strong assumption, especially for cases where different pressures and bubble diameter variations are observed. Thus, we may slightly distinguish the applied values of θ and $d\theta$ for different pressures within a given experiment, keeping a change no larger than 5° .
- Kossolapov cases at $G_L = 500 \text{ kg/m}^2/\text{s}$ are better predicted. Cases under higher mass fluxes (1000 and $1500 \text{ kg/m}^2/\text{s}$) present underestimation that could come from the value of $d\theta$. At such mass fluxes, the Weber number can be up to a decade higher and bubbles may thus accept a larger inclination before detachment.
- Cases of Ren and Chen rely on chosen values for θ and $d\theta$ and not on measured ones. They are therefore subject to strong uncertainties. We can note that the values for Chen cases are significantly high.
- The proposed growth law is still rather simple and may miss significant information, especially regarding bubble size and fluid properties such as the Prandtl number.

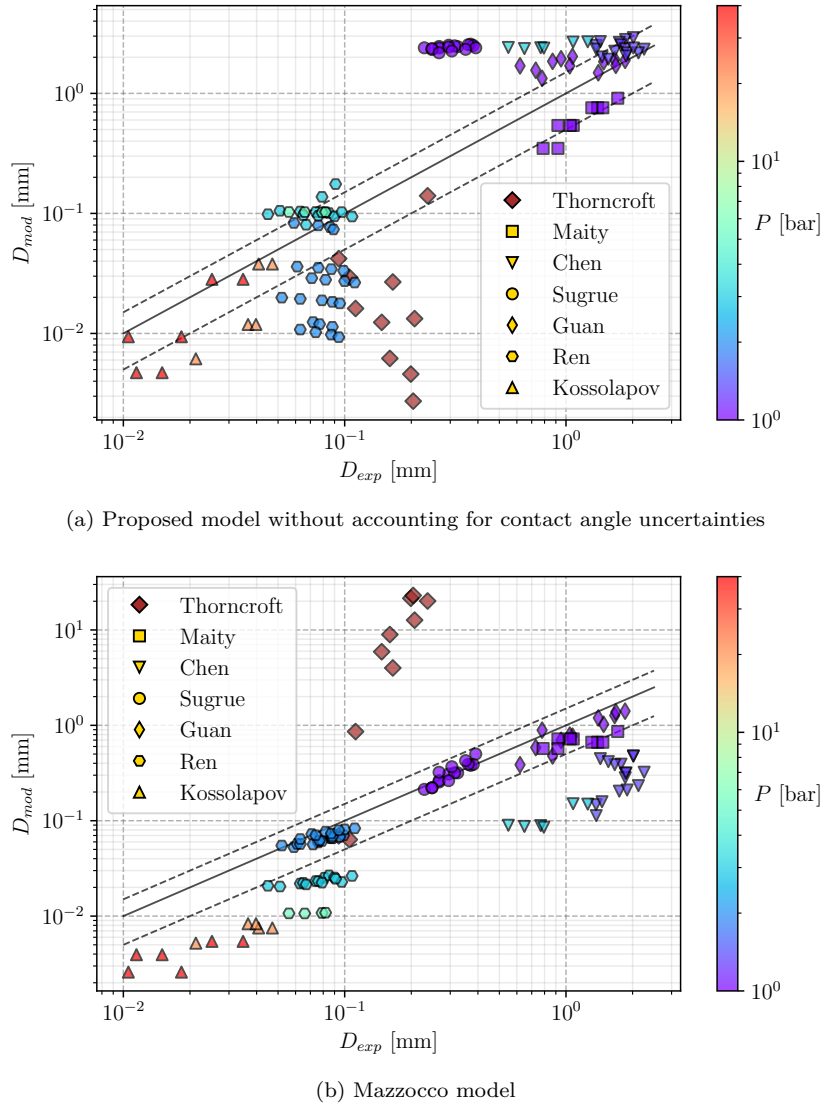


Figure 4.8: Predicted bubble departure diameters

- Errors on Thorncroft cases may be linked to uncertainties regarding FC-87 properties. Indeed, we use the values given at $T_{sat} = 29^\circ$ at 1 bar in his work [**thorncroft_experimental_1998**]. However, the saturation temperature indicated in his test matrix is close to 40° which means that measurements were conducted at a higher pressure, for which we do not have FC-87 properties.

Therefore, using modified values of θ and $d\theta$ among experimental data sets with no more than a 5° change (except for Sugrue cases reassessed values) leads to predictions on Figure 4.10.

The predictive capacity of the model is significantly enhanced, especially on Sugrue's cases which tends to indicate that the contact angle reassessment was justified under the truncated sphere hypothesis. Table 4.4 summarizes the average errors obtained with the present model and Mazzocco's one.

The proposed model achieves an overall better predictive capability even when excluding measurements from Thorncroft on which Mazzocco's model strongly overestimates the departure diameter. Mazzocco's model is still better on Sugrue and Guan cases since it was built and validated using those measurements. It better predicts results from Ren but only for the 2 bar cases while it underestimates the departure diameter for higher pressures. Those results are a coupled effect of his optimized growth law along with the imposed value of r_w/R and the use of the inclination angle to hinder departure as mentioned in 4.3.6.

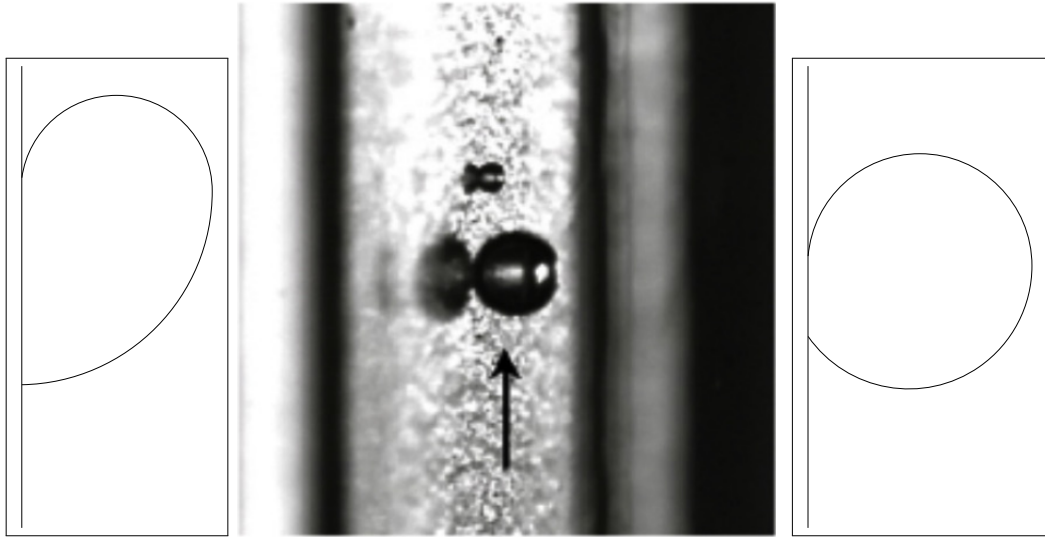
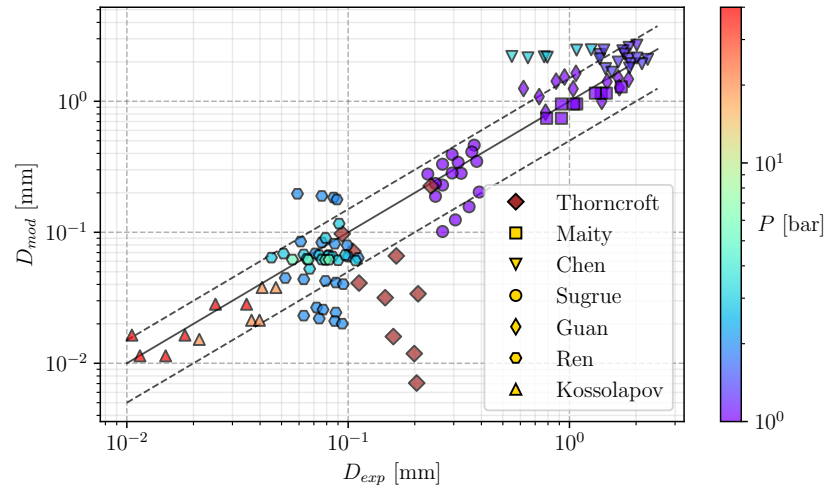


Figure 4.9: Initially assumed, real and reassessed bubble shape for Sugrue cases (picture adapted from [sugrue_experimental_2014]).

Author	θ [°]	$d\theta$ [°]
Thorncroft	20	14
Maity	45	10
Chen	92.5	27.5
Sugrue	20	15
Guan	47.5	17.5
Ren (2 bar)	45.5	8.5
Ren (3 bar)	37.5	3.5
Ren (5 bar)	35.5	3.5
Koss. (500 kg/m ² /s)	80	0.5
Koss. (1000 kg/m ² /s)	80	1
Koss. (1500 kg/m ² /s)	80	1.5



(a) Modified contact angle and hysteresis values.

(b) Predicted bubble departure diameters.

Figure 4.10: Proposed model performance while accounting for contact angle uncertainties

The approach demonstrated the importance and the strong influence of the contact angle and hysteresis. A small change of their value (staying in the uncertainty range of 5°) allowed to reach reasonable predictions over a large range of bubble departure diameters with the model of this paper, using a reduced number of empirical parameters.

Author	Mazzocco	Present model
Thorncroft	4874%	60.6%
Maity	39.7%	13.8%
Chen	83.8%	69.9%
Sugrue	9.73%	26.22%
Guan	25.5%	36.8%
Ren	40.32%	44.1%
Kossolapov	78.3%	24.1%
Total	442%	43%
Total (without Thorncroft)	46.58%	41.4%

Table 4.4: Average relative error reached by the models.

4.5 SLIDING PHASE

4.5.1 Modeling

After departure, bubbles slide over a distance l_{sl} which scales the impact of the sliding phenomenon over the wall heat transfer. Achieving good prediction of bubble sliding velocity is then important if one wishes to correctly quantify its impact.

Following the force balance framework presented in Section 4.3, we can write Newton's second law parallel to the wall for the sliding bubble.

$$\rho_V \frac{d(V_b U_b)}{dt} = -\pi R \sigma f_{C,x} + \frac{4}{3} \pi R^3 (\rho_L - \rho_V) g + \frac{1}{2} C_D \rho_L \pi R^2 U_L^2 + \frac{4}{3} \pi R^3 \rho_L \left[3C_{AM,x} \frac{\dot{R}}{R} U_{rel} - C_{AM,x} \frac{dU_b}{dt} \right] \quad (4.131)$$

This equation can be re-written to express the bubble acceleration.

$$\left(1 + \frac{\rho_L}{\rho_V} C_{AM,x} \right) \frac{dU_b}{dt} = \left(\frac{\rho_L}{\rho_V} - 1 \right) g + \frac{3}{8} \frac{C_D}{R} \frac{\rho_L}{\rho_V} (U_L - U_b) |U_L - U_b| + 3 \frac{\dot{R}}{R} \left[C_{AM,x} \frac{\rho_L}{\rho_V} (U_L - U_b) - U_b \right] - \frac{3}{4} \frac{\sigma}{\rho_V} \frac{f_{C,x}}{R^2} \quad (4.132)$$

Then, we numerically solve this equation from the moment when $R \geq R_d$ using a first order Euler scheme for a duration close to the experimental sliding time. Next sections compare obtained results against low and high pressure data.

4.5.2 Low Pressure Sliding

Maity [maity_effect_2000] provided simultaneous measurements of bubble radius and velocity over time for three liquid mass fluxes in vertical boiling. To assess the validity of Eq. 4.132, we modify the growth constant K in order to roughly match experimental radius measurements. The goal is to verify

if the force balance allows a good prediction of bubble velocity provided a correct bubble growth. The contact angles were kept the same as in 4.4.3 since Maity provided average values over the bubble lifetime.

Results are displayed on Figure 4.11. The model seems to fairly good predict bubble sliding velocity for the 3 cases. The moment of departure is a bit underestimated as previously observed (Figure 4.8). The biggest discrepancy is observed for the case at $G_L = 143.8 \text{ kg/m}^2/\text{s}$. The slope of the velocity profile is close to the experiments, but the bubble reaches a nearly constant acceleration too rapidly which yields an approximately constant overestimation of 0.1 m/s.

The $G_L = 239.6 \text{ kg/m}^2/\text{s}$ is well predicted regarding the velocity. However, the growth profile was difficult to match since measurements exhibit significant changes in growth regime after departure, which is probably due to the bubble being large enough to be impacted by the bulk flow. A finer model for bubble growth could be of interest here.

We can note that values of K between 0.5 and 1 were used to better fit the bubble radius time profile.

4.5.3 High Pressure Sliding

In his work, Kossolapov [kossolapov_experimental_2021] conducted measurements of radius and sliding length over thousands of individual bubbles and then provided the associated statistical distributions. To compare our model with his measurements, we took the upper and lower bounds of R and l_{sl} over time and plotted the associated bands of measured values as shown on Figure 4.12 and 4.13. Comparisons were done for cases at 20 bar and 40 bar and 3 different values of G_L . The value of $d\theta$ for the simulations was kept really small (2° at 20 bar and 0.5° at 40 bar) since bubble tilt is supposed to reduce during sliding because the relative velocity regarding the liquid flow is diminishing. Moreover, higher pressure means smaller bubbles that are even more unlikely to present a significant contact angle hysteresis. We also want to mention that neglecting the capillary term in Eq. 4.132 had a minor impact over the results except that the bubble accelerates a little bit faster.

The obtained results are in good agreement with the sliding length profile vs. time, which means bubble sliding velocity is well predicted for those cases.

Once the estimation of ΔT_w using Eq. 4.127 is corrected as mentioned in 4.4.2, values of K between 0.8 and 1.3 reasonably fits the bubble radius measurements.

4.6 CONCLUSION

In this work, we proposed a revisited force balance for a single bubble in a vertical upward boiling flow. This force balance was then used to study bubble departure by sliding and compared with bubble departure diameter and sliding velocity measurements. The main highlights of this study are:

- The use of a recent correlation to compute the Drag coefficient thanks to DNS results of Shi *et al.* [shi_drag_2021].
- Reassessed computation of the Added Mass force and associated coefficients from the expression of the liquid kinetic energy proposed by Van Der Geld [van_der_geld_dynamics_2009].
- A global force balance that avoids including extra empirical parameters. We notably get rid of empirical choices regarding bubble foot radius and do not include an arbitrary bubble inclination angle to create an Added Mass term hindering departure.
- A non dimensional approach leading to force regime maps to qualitatively determine the dynamic regime in which bubbles are departing from the nucleation site. It shows that the detaching Added Mass term due to external liquid flow is rarely negligible and often dominates at low pressure. Increasing pressure mostly leads to Drag dominant regimes.
- Bubble departure diameter predictions are achieved with a reasonable accuracy over a large range of measured values from 7 data sets. This could be reached by accepting an uncertainty of 5° for

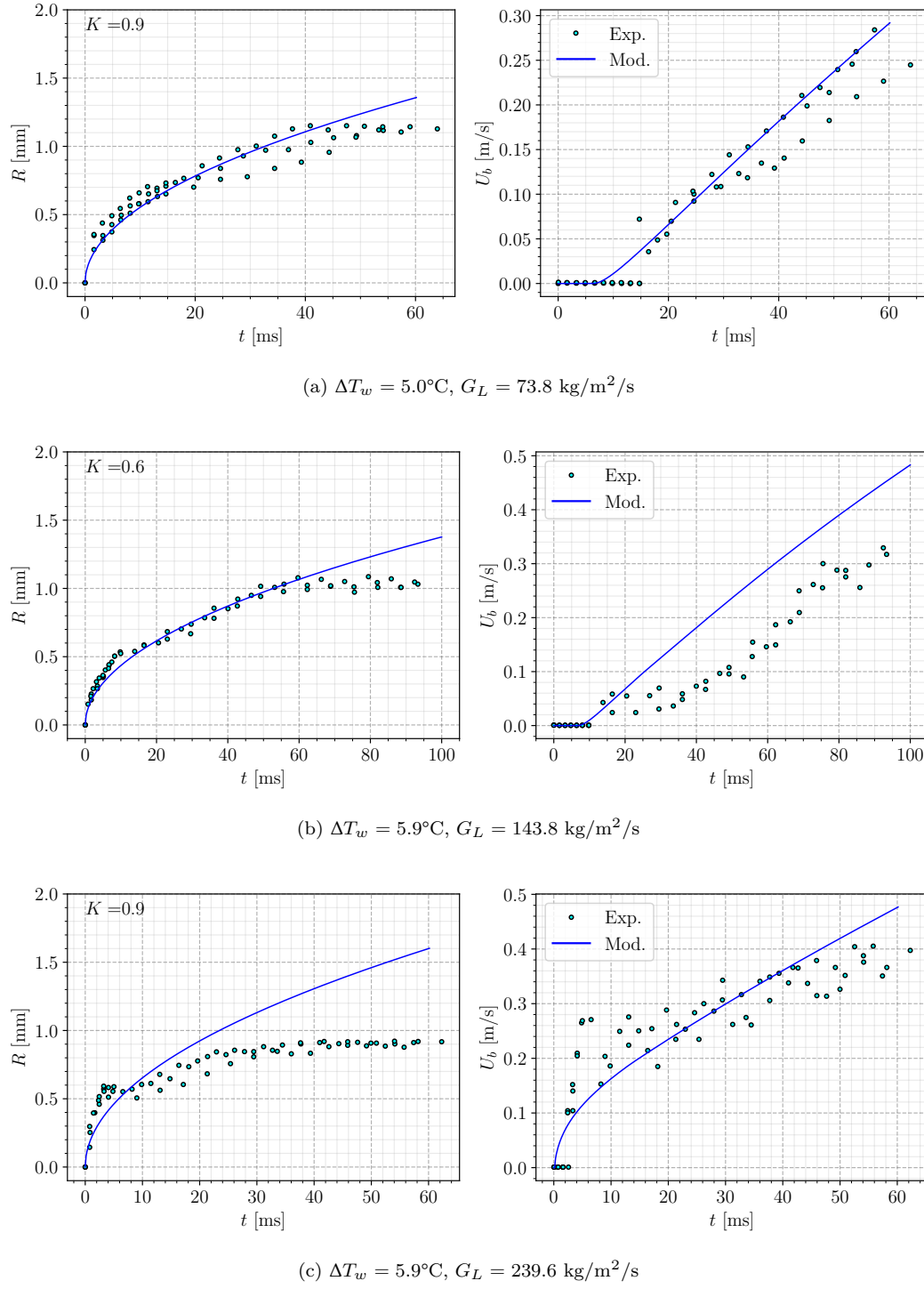
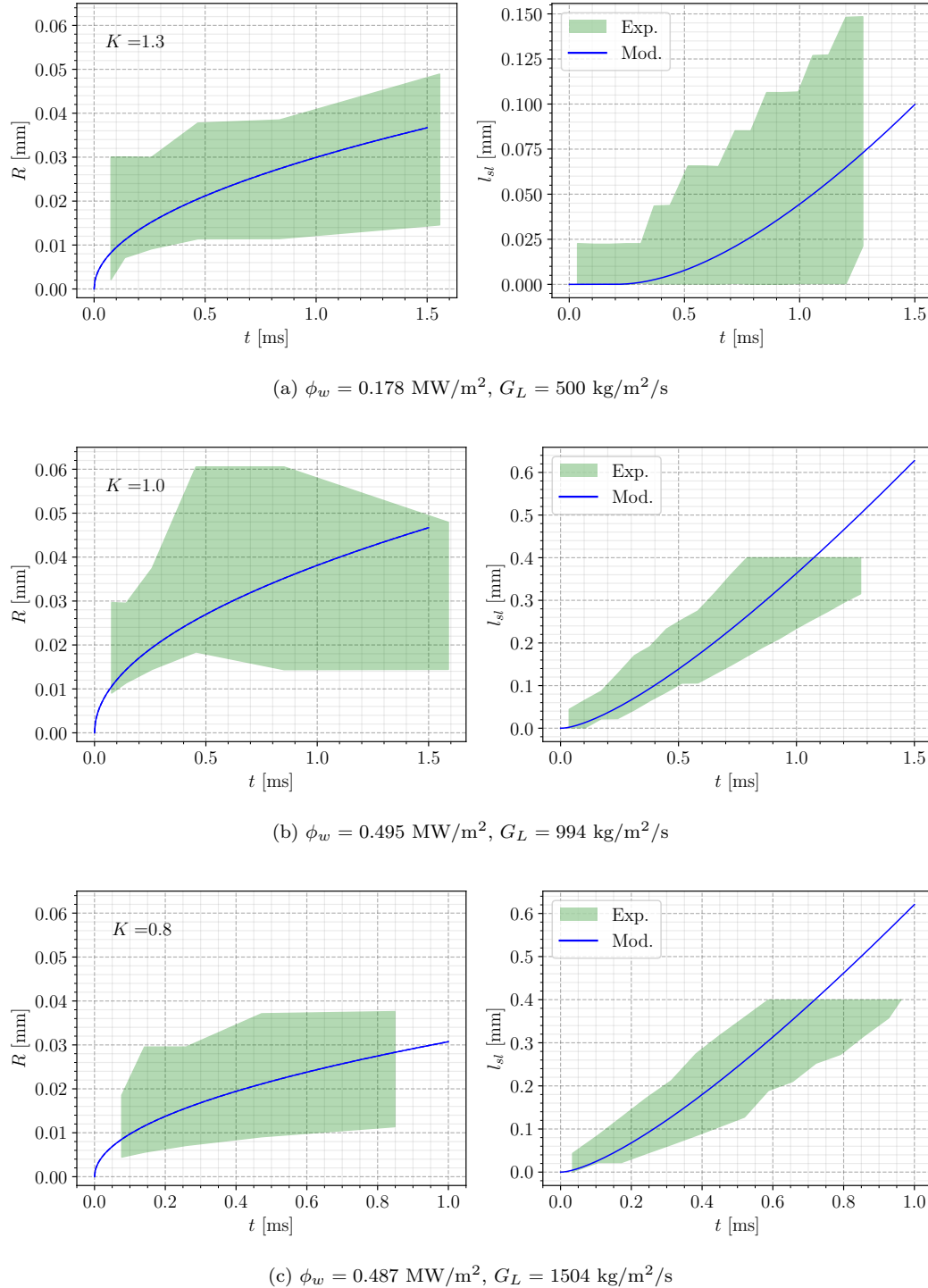


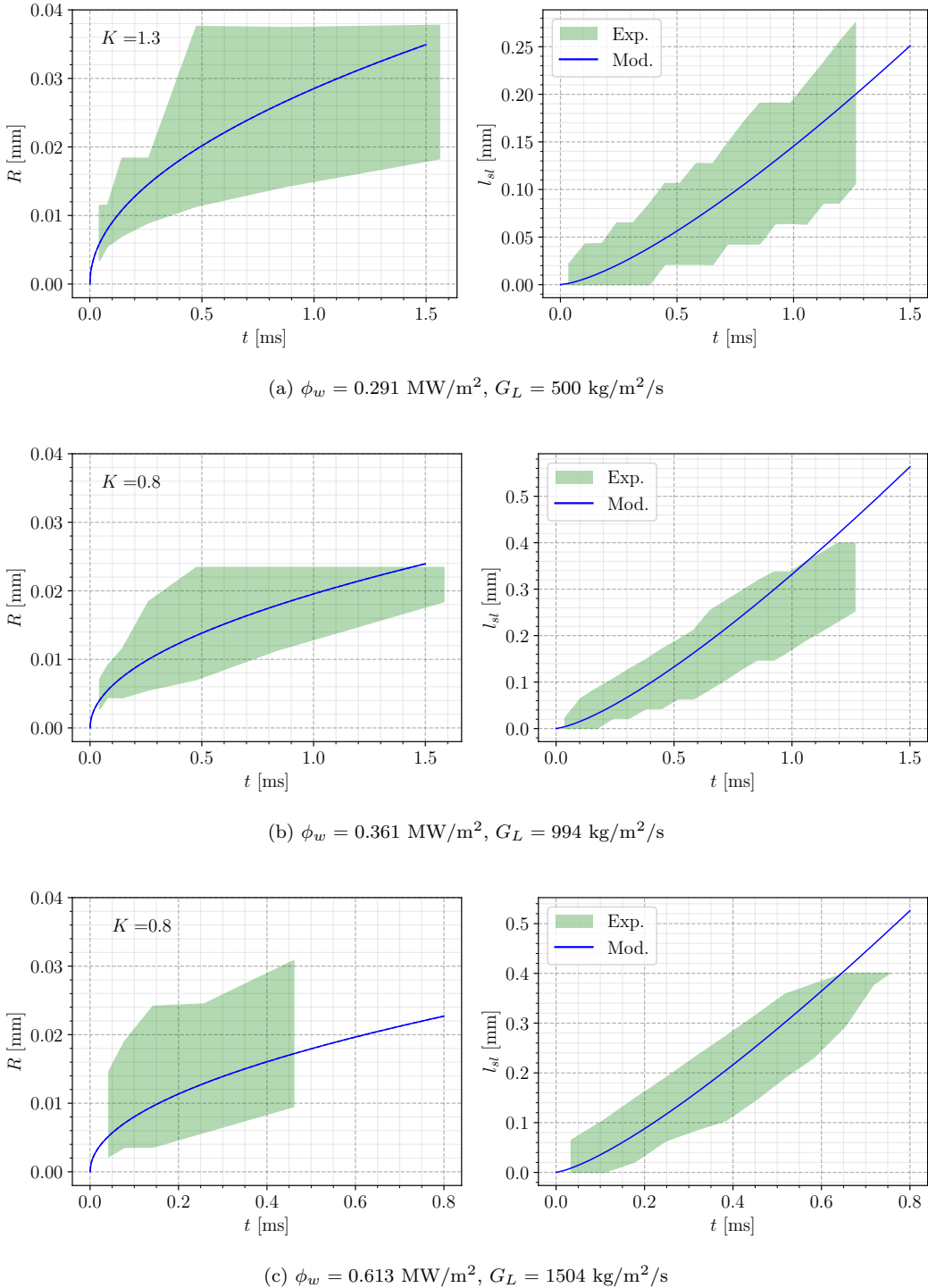
Figure 4.11: Bubble sliding velocity predictions on Maity cases

the values of the contact angle θ and half-hysteresis $d\theta$ to which the model was sensitive. This indicates that using fixed values for large data sets seems incorrect and that extra empiricism may not be needed if a proper modeling of those parameters was achieved.

Figure 4.12: Bubble sliding length predictions on Kossolapov cases - $P = 20 \text{ bar}$

- Bubble sliding velocity simulations showed a good agreement with experimental observations both at low and high pressure provided a correct bubble growth profile.

The limitations of the developed approach lie mainly in the simple and empirical law to estimate the growth constant K (Eq. 4.128). This could be enriched by a clean modeling of the bubble growth including effects such as condensation, microlayer evaporation and impact of the external liquid flow.

Figure 4.13: Bubble sliding length predictions on Kossolapov cases - $P = 40$ bar

Existing models rely on empirical values which thus reduces their general applicability outside of their validation range. For instance, studies conducted by Zhou [**zhou_experimental_2020**] and Yoo [**yoo_development_2018**] could be used by enriching their modeling with finer results to get rid of data fitting. DNS results such as those regarding bubble growth in a flowing superheated or subcooled liquid by Legendre *et al.* [**legendre_thermal_1998**] could be of interest in that prospect.

Finally, the precise estimation of the contact angle and hysteresis remains a critical parameter to predict departure by sliding as demonstrated throughout this study. Local measurements of those values and their evolution with operating conditions would be a very valuable information in that regard. The article of Song & Fan [[song_temperature_2021](#)] that sums up existing modeling and experimental measurements provides a good overview of the problem and identifies the associated challenges that are still to be tackled.

5

ASSEMBLING OF A NEW HEAT FLUX PARTITIONING MODEL

5.1 NEW MODEL

5.2 GENERAL DESCRIPTION OF THE MODEL

The main goal of such a model is to provide a way to compute the wall temperature T_w resulting from the applied wall heat flux ϕ_w , or the other way around.

In order to try to be as extensive as possible regarding the different heat transfer mechanisms at stake, the wall heat flux is supposed to be split between 4 different contributions (Figure 5.1) :

- A convective heat flux towards the liquid phase, unaffected by the presence of bubbles on the heater surface : $\phi_{c,l}$
- A boiling heat flux, representing the energy removed from the wall to grow a bubble up to its lift-off diameter : ϕ_b
- A quenching heat flux, accounting for transient heat transfer to the liquid phase when bubbles slide or lift-off from the wall : ϕ_q
- A convective heat flux towards the vapor phase, representing the heat transfer occurring through the dry areas of the surface beneath the bubbles : $\phi_{c,v}$

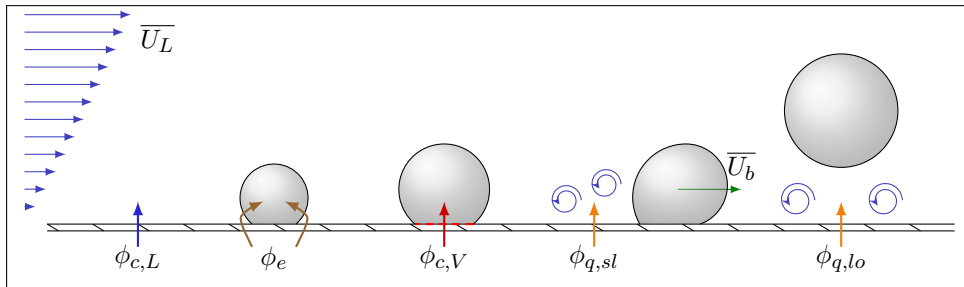


Figure 5.1: Sketch of the considered HFP **A terminer, je dois ajouter des flèches pour indiquer les flux !**

Listing of the different physics parameter involved in bubble departure phenomenon

The supposed mechanisms yields the total wall heat flux partitioning (5.1) :

$$\phi_w = \phi_{c,l} + \phi_e + \phi_q + \phi_{c,v} \quad (5.1)$$

In the following subsections, we focus our analysis on each term to detail its modeling.

5.2.1 Convective heat fluxes

The convective heat fluxes towards the liquid phase $\phi_{c,l}$ and the vapor phase $\phi_{c,v}$ can be written using an associated heat transfer coefficient (5.2) :

$$\phi_{c,l} = \textcolor{orange}{a}_{c,l} \textcolor{blue}{h}_{c,l} (\textcolor{red}{T}_w - \textcolor{blue}{T}_l) \quad \text{and} \quad \phi_{c,v} = \textcolor{orange}{a}_{c,v} \textcolor{blue}{h}_{c,v} (\textcolor{red}{T}_w - \textcolor{blue}{T}_v) \quad (5.2)$$

5.2.2 Boiling heat flux

The total energy associated with the nucleation of a bubble with a volume V_b can be expressed as $V_b \rho_v h_{lv}$. If one knows the nucleation frequency f at which bubbles are generated along with the nucleation site density on the heater surface N_{sit} , the resulting heat flux associated with the nucleation phenomenon can thus be written as (5.3) :

$$\phi_b = \textcolor{blue}{N}_{sit} \textcolor{blue}{f} \textcolor{orange}{V}_b \rho_v h_{lv} \quad (5.3)$$

5.2.3 Quenching heat flux

The quenching heat flux accounts for the transient heat transfer which occurs when cold liquid is brought close to the wall when a bubble slides or lifts-off, thus disrupting the previously established thermal boundary layer.

DEL VALLE & KENNING have supposed that this kind phenomenon can be represented as a semi-infinite transient heat transfer between the liquid at T_l and the wall at T_w . Solving the conductive heat transfer problem yields an instantaneous heat flux expressed as Eq. 5.4.

$$\phi_q(t) = \frac{\lambda_l (\textcolor{red}{T}_w - \textcolor{blue}{T}_l)}{\sqrt{\pi \eta_l t}} \quad (5.4)$$

Therefore, we can average this heat flux over a time t_w , during which the quenching operates, and ponderating it both by the portion of the affected heater area a_q and the fraction of quenching time over a total bubble nucleation cycle $t_w f$, yielding :

$$\phi_q = \textcolor{orange}{a}_q \textcolor{blue}{t}_w \textcolor{blue}{f} \frac{1}{\textcolor{blue}{t}_w} \int_0^{\textcolor{blue}{t}_w} \frac{\lambda_l (\textcolor{red}{T}_w - \textcolor{blue}{T}_l)}{\sqrt{\pi \eta_l t}} dt = \textcolor{orange}{a}_q \textcolor{blue}{t}_w \textcolor{blue}{f} \frac{2\lambda_l (\textcolor{red}{T}_w - \textcolor{blue}{T}_l)}{\sqrt{\pi \eta_l \textcolor{blue}{t}_w}} \quad (5.5)$$

5.2.4 Needed closure relationships

After expressing each heat flux components of the global partitioning, the resulting formulations yields a first list of parameters for which closure relationships (or at least precise definition) are needed. Terms previously highlighted in orange will be given a specific definition, terms in blue require a closure law, wall temperature is indicated in red.

The different terms needing further development are listed below :

- The fractions of the heater area ponderating convective and quenching heat transfers : $a_{c,l}$, $a_{c,v}$ and a_q (??)
- The convective heat transfer coefficients : $h_{c,l}$ and $h_{c,v}$ (Section ??)
- The nucleation site density over the heater surface : N_{sit} (Section : ??)

- The nucleation frequency, which includes both the growth time t_g (Section ??) of a bubble and the waiting time t_w (**Je dois encore proposer une modélisation pour t_w , à discuter**) : $f = 1 / (t_g + t_w)$
- The total bubble volume V_b (4.2.1) generated until its lift-off, thus including the modeling of the bubble lift-off diameter : D_{lo}
- The phases temperature : T_l (??) and T_v (??)

5.2.5 Single Bubble Quenching Area

$$A_{q,1b} = \begin{cases} \pi R_{lo}^2 & \text{if } l_{sl} \leq R_{lo} - R_d \\ \frac{1}{2}\pi R_d^2 + l_{sl}(R_d + R_{lo}) + \frac{1}{2}\pi R_{lo}^2 & \text{if } l_{sl} \geq R_{lo} + R_d \end{cases} \quad (5.6)$$

Which can be re-expressed by defining $l_{sl}^* = \frac{l_{sl}}{R_{lo}}$ and $A_{q,1b}^* = \frac{A_{q,1b}}{\pi R_{lo}^2}$

$$A_{q,1b}^* = \begin{cases} 1 & \text{if } l_{sl}^* \leq 1 - \frac{R_d}{R_{lo}} \\ \frac{1}{2} \left(1 + \left(\frac{R_d}{R_{lo}} \right)^2 \right) + \frac{l_{sl}^*}{\pi} \left(1 + \frac{R_d}{R_{lo}} \right) & \text{if } l_{sl}^* \geq 1 + \frac{R_d}{R_{lo}} \end{cases} \quad (5.7)$$

and we linearly interpolate those two expressions for the region where $1 - \frac{R_d}{R_{lo}} \geq l_{sl} \geq 1 + \frac{R_d}{R_{lo}}$.

5.2.6 Bubble Growth Time

5.2.7 Bubble Wait Time

5.2.8 Nucleation Site Density

The choice of a nucleation site density correlation can be a complicated matter since many different laws exist in the literature (Lemmert & Chawla, Hibiki & Ishii, Basu *et al.*, etc.).

In order to help us choosing an appropriate closure for N_{sit} , we compare 4 different correlations (Lemmert & Chawla, Hibiki & Ishii, Li *et al.* and Zhou *et al.*) to 4 different sets of experimental measurements of the NSD in various thermal-hydraulics conditions (Borishanskii *et al.*, Richenderfer *et al.*, Kossolapov, Zhou *et al.*). The results are presented on Figures 2.5 to 2.8 with error bars of $\pm 50\%$.

As we can see, the model from Lemmert & Chawla fails to correctly predict the nucleation site density at high pressures. Which is a direct consequence of its solely dependency on the wall superheat.

On the other hand, models such as those from Hibiki & Ishii and Li *et al.* seem to better reproduce the different trends with flow conditions.

Finally, although the model of Zhou *et al.* includes a pressure term, its partial calibration on only low pressure data may explain the huge difference observed when trying to reproduce other experimental measurements.

Je vais ajouter un tableau des conditions TH de chacune des expériences + la formule détaillée de chacun des modèles.

5.2.9 Considerations on bubble interaction and nucleation sites deactivation

NSD correlation actually compute the total number of sites where bubbles can nucleate on a surface. However, they do not represent how important a nucleation site will be in term of bubbles generation compared to another.

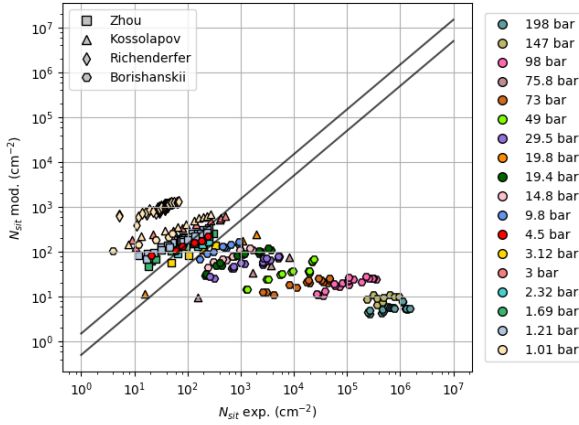


Figure 5.2: Model from Lemmert & Chawla

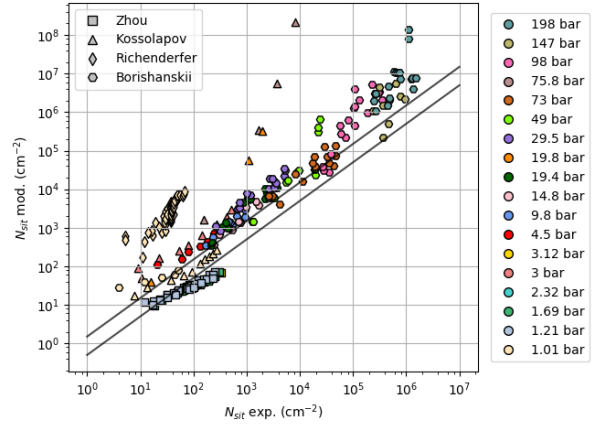
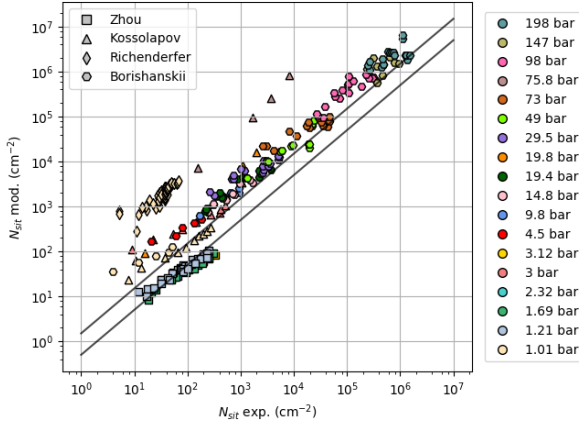
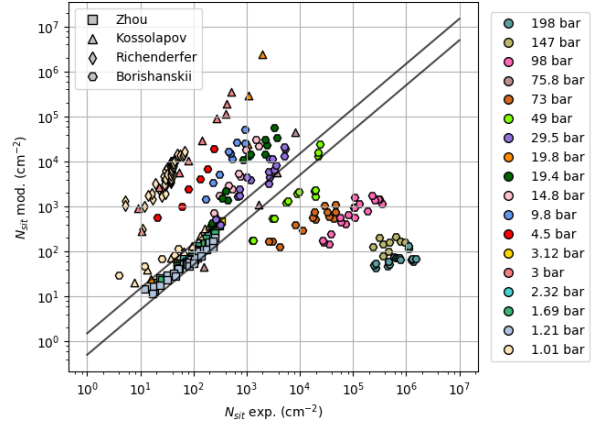


Figure 5.3: Model from Hibiki & Ishii

Figure 5.4: Model from Li *et al.*Figure 5.5: Model from Zhou *et al.*

In fact, Kossolapov has observed that each nucleation site has its own bubble nucleation frequency. Thus implying that some sites play a much greater role in wall nucleation compared to others. One can even consider that some nucleation sites can be neglected regarding their small impact on the whole phase change process.

In order to physically take into account this effect, Gilman considered a statistical approach, by assuming that nucleation site are randomly distributed over the heater surface (Complete Spatial Randomness). Then, considering that a nucleation site located under a bubble will be deactivated, one can express the number of sites actually contributing to bubble nucleation $N_{sit,a}$ as :

$$N_{sit,a} = (1 - \mathcal{P}) N_{sit}, \text{ with } \mathcal{P} = 1 - e^{-N_b \pi (D_b/2)^2} \quad (5.8)$$

where $N_b = t_g f N_{sit}$ is the actual average density of bubbles on the heater surface.

The resulting number of sites is a solution of the implicit equation on N_{sit} , which can be solved numerically or using the Lambert function (reciprocal of $w \rightarrow we^{-w}$).

Je vais détailler un peu plus cela avec des schémas clairs, ainsi qu'un exemple de comment cela pondère la densité de site totale, puisque cela permet d'éviter la divergence dans une loi telle que celle de Hibiki & Ishii à haute surchauffe pariétale

5.2.10 Nucleation Sites and Bubbles Interactions

5.2.10.1 Static suppression

If we suppose that the nucleation sites follow a homogeneous spatial Poisson process with an event density λ , we can express the probability of finding n sites within an area A as :

$$\mathcal{P}(N(A) = n) = \frac{(\lambda A)^n}{n!} e^{-\lambda A} \quad (5.9)$$

If we consider the actual number of bubble-generating sites N_b , those sites are holding a bubble over a fraction $t_g f$ of the nucleation cycles in average. Thus, the actual density of bubbles held by the sites is : $t_g f N_b$. To derive N_b from the value N_{sit} provided by NSD correlations, we have to evaluate the probability of nucleation site overlapping, which corresponds to a distance r lower than R_d between two bubbles.

$$\mathcal{P}(r \leq R_d) = 1 - \mathcal{P}(N(\pi R_d^2) = 0) \quad (5.10)$$

$$= 1 - e^{-N_b t_g f \pi R_d^2} = \mathcal{P} \quad (5.11)$$

This probability thus represents the proportion of bubble that can't be geometrically accommodated on the surface. We can then evaluate N_b from N_{sit} as :

$$N_b = (1 - \mathcal{P}) N_{sit} \quad (5.12)$$

$$\Leftrightarrow N_b t_g f \pi R_d^2 e^{N_b t_g f \pi R_d^2} = N_{sit} t_g f \pi R_d^2 \quad (5.13)$$

$$\Leftrightarrow N_b = \frac{\mathcal{V}(N_{sit} A)}{A} \quad \text{where } A = t_g f \pi R_d^2 \quad (5.14)$$

5.2.10.2 Static coalescence

Now that the actual number of bubble-generating sites have been identified, we can consider other interaction phenomena that can occur on the boiling surface. For instance, if two sites are simultaneously generating a bubble at a distance d between R_d and $2R_d$, the bubbles will coalesce while growing up to the detachment diameter. To estimate the probability of having a bubble on a site in this distance range, we consider the probability density function of the nearest-neighbour in the case of a homogeneous spatial Poisson process f with an event density λ .

$$f(r) = 2\lambda\pi r e^{-\lambda\pi r^2} \quad (5.15)$$

The considered probability of interaction is then :

$$\mathcal{P}(R_d \leq r \leq 2R_d) = \int_{R_d}^{2R_d} f(r) dr \quad (5.16)$$

$$= e^{-\lambda\pi R_d^2} - e^{-4\lambda\pi R_d^2} \quad (5.17)$$

$$= e^{-\lambda\pi R_d^2} \left[1 - \left(e^{-\lambda\pi R_d^2} \right)^3 \right] \quad (5.18)$$

$$= \mathcal{P}_{coal,st} \quad \text{with } \lambda = t_g f N_b \quad (5.19)$$

The density of bubble-generating sites that will lead to a static coalescence can then be estimated as :

$$N_{coal,st} = \mathcal{P}_{coal,st} N_b \quad (5.20)$$

If we suppose that coalescing bubbles will instantly lift-off due to the perturbation associated with the coalescence process, this yields an associated boiling flux :

$$\phi_{e,coal,st} = N_{coal,st} f \rho_V h_{LV} \frac{4}{3} \pi R_{coal,st}^3 \quad \text{where} \quad R_{coal,st} = \sqrt[3]{2} R_d \quad (5.21)$$

considering that the bubbles will merge approximately at $R = R_d$.

5.2.10.3 Sliding coalescence

Now that suppressed sites and sites that will lead to static coalescence have been identified, the remaining sites $N_{sl} = (1 - \mathcal{P}_{coal,st}) N_b$ will generate sliding bubbles. While sliding, a single bubble swipes an area :

$$A_{sl,1b} \approx l_{sl,1b} \frac{D_d + D_{lo}}{2} \quad (5.22)$$

In this area, there are an average number of bubble-generating sites $N_b A_{sl,1b}$ and an average number of growing bubbles on their sites $t_g f N_b A_{sl,1b}$

Two situations can happen from the sliding process :

- The bubble slides without coalescing
- The bubble coalesces while sliding with a bubble growing on its site and lifts-off

Following the same approach from the static suppression, we can estimate the probability of finding no growing bubble over the sliding surface :

$$\mathcal{P}(N(A_{sl,1b}) = 0) = e^{-N_b t_g f A_{sl,1b}} \quad (5.23)$$

Thus, if a sliding bubble among the N_{sl} does not encounter any growing bubble, the sites on its sliding area will be wiped and thus be quenched by cold liquid. This means that those sites will be suppressed due to the sliding of other bubbles over them.

Among the N_b bubble generating sites we can identify 4 categories of sites :

- Sites generating bubbles which will slide without encountering any growing bubble on their path :

$$N_{sl,NC} = N_{sl} e^{-f t_g N_b A_{sl,1b}}$$

- Sites generating bubbles that will coalesce with a growing bubble during sliding :

$$N_{sl,C} = N_{sl} \left(1 - e^{-f t_g N_b A_{sl,1b}} \right)$$

- Sites which will be suppressed by bubbles sliding without coalescing :

$$N_{sup,sl} = N_{sl,NC} N_b A_{sl,1b}$$

- Sites generating bubbles that will coalesce with a sliding bubble coming from upstream. Those bubbles are still in the growing phase up to detachment when they are coalescing with sliding bubbles. Therefore, there are equal to the number of sliding bubbles that will coalesce :

$$N_{g,C} = N_{sl,C}$$

This allows to finally write :

$$N_b = N_{sl,NC} + N_{sl,C} + N_{sup,sl} + N_{g,C} \quad (5.24)$$

$$= N_{sl} \left[2 - e^{-ft_g N_b A_{sl,1b}} (A_{sl,1b} N_b - 1) \right] \quad (5.25)$$

Which finally yields the total number of sliding bubbles :

$$N_{sl} = \frac{N_b}{2 - e^{-ft_g N_b A_{sl,1b}} (A_{sl,1b} N_b - 1)} \quad (5.26)$$

Part IV
TOWARDS THE INDUSTRIAL GEOMETRY

6

PROMOTEUR

6.1 BOILING FREON IN A TUBE WITH MIXING VANES : DEBORA-PROMOTEUR EXPERIMENTS

In this section, we simulate upward boiling flows of R12 in a vertical tube equipped with mixing vanes and compare the outlet void fraction profile predicted by NEPTUNE_CFD with measurements coming from the DEBORA-Promoteur experiment.

6.1.1 *Description of the experiment*

In 2003, the wish to investigate boiling flows in complex geometries similar to those in PWR fuel assembly lead CEA and EDF to modify the DEBORA facility to introduce mixing vanes (MV) within the tube. This mixing device has been designed to have the same geometric properties as the mixing vanes attached to rod bundle grids (Figure 6.1).

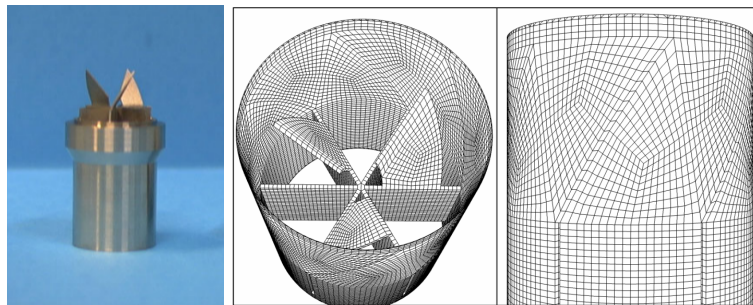


Figure 6.1: Picture of the mixing device (left) and its fine meshing (right).

Two series of measurements were conducted on this geometry :

- Campaign 4800 : measurements of α using two optical probes, mixing device placed $0.455m \approx 23.5D_h$ upstream the end of the heating length
- Campaign 5200 : measurements of α and $U_{G,z}$ using two optical probes, mixing device placed $0.192m \approx 10D_h$ upstream the end of the heating length

The goal of those tests was to observe the impact of the mixing device on the void fraction profile. The induced rotation is expected to gather the bubbles at the center of the tube and enhance condensation for highly subcooled cases. Those expectations are confirmed when looking at experimental α profiles on Figure 6.2. The strong differences compared to simple tube profiles could explain the gain on the CHF value in PWR thanks to the mixing grids. Cases are named following the same nomenclature as presented in Section 2.1.

6.1.2 NEPTUNE_CFD simulations of DEBORA-Promoteur cases

We simulated 3 cases for each position of the mixing device, covering different local thermodynamic quality near the vanes ($x_{eq,MV}$) :

- 48G3P26W23Te65 & 52G3P26W23Te65 with $x_{eq,MV} \approx -1\%$
- 48G3P26W23Te69 & 52G3P26W23Te69 with $x_{eq,MV} \approx 4\%$
- 48G3P26W23Te75 & 52G3P26W23Te75 with $x_{eq,MV} \approx 12\%$

Computations are conducted using two meshes for Te69 cases : a large one (M1) with 444 703 cells and a fine one (M2) with 3 487 627 cells. Results for void fraction profiles are shown on Figure 6.2.

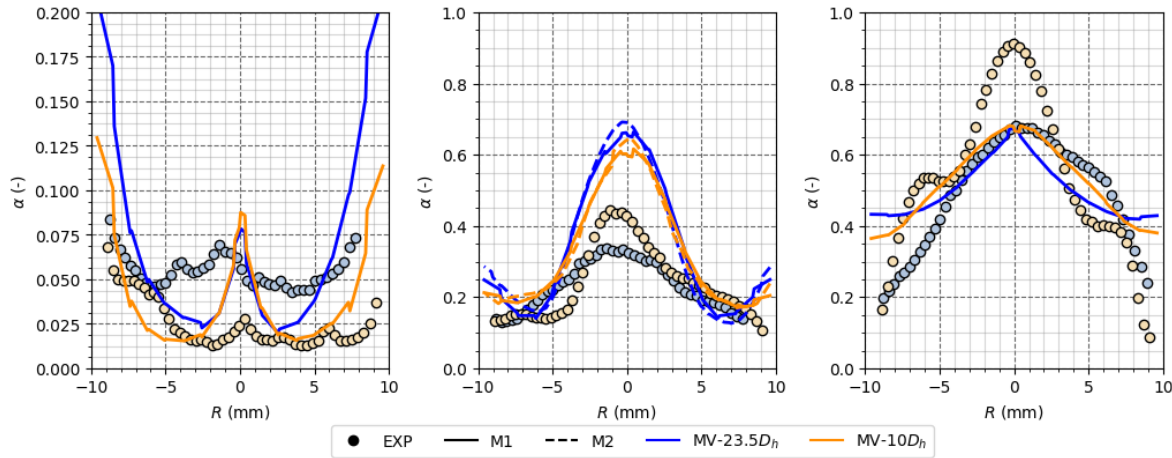


Figure 6.2: NCFD (lines) vs. Exp. (circles) - α profiles for two MV positions (23.5 D_h in blue, 10 D_h in orange) - $T_{in} = 65^\circ\text{C}$ (left), $T_{in} = 69^\circ\text{C}$ (middle), $T_{in} = 75^\circ\text{C}$ (right) - Simulations using two meshes M1 (coarse) and M2 (fine) for $T_{in} = 69^\circ\text{C}$.

Quantitatively speaking, it seems that NEPTUNE_CFD reproduces the effect of vapor accumulation at the center thanks to the pressure gradient generated by the swirl induced by the mixing vanes. The radial position of the core void fraction peak correctly matches the experimental one.

However, measured void fraction profiles are not predicted correctly. A particularly strong overestimation of the core void fraction is observed as well as close to the wall. The CMFD results tend to rapidly reach a core void fraction around 60% ($T_{in} = 69^\circ\text{C}$ cases) and then flattens with increasing temperature ($T_{in} = 75^\circ$ cases). This contradicts experimental observation where the void fraction profile globally rises when inlet temperature increases, except at the wall where no peak is observed due to bubble removing effect by the liquid's rotation. Moreover, the $T_{in} = 75^\circ$ case with MV at 10 D_h experimentally shows local α peaks at $R \approx \pm 6\text{mm}$ which remain currently unexplained and not reproduced by the simulations.

To investigate what could be a potential origin for the core void fraction peak overestimation, we present in Section 6.2 single-phase flow simulations in the MV geometry.

6.2 LIQUID WATER FLOW IN A TUBE WITH MIXING VANES : AGATE-PROMOTEUR EXPERIMENT

In this penultimate section, we briefly investigate single-phase flow within the same geometry as Section 6.1.

6.2.1 Description of the experiment

In 2003, using the same experimental geometry as DEBORA-Promoteur cases (Section 6.1), Laser Doppler Velocimetry (LDV) measurements of velocity and turbulent fluctuations for an adiabatic single-phase flow of water were conducted. The outlet pressure was around $P = 2$ bar with an inlet mass flux $G \approx 3000 \text{ kg/m}^2/\text{s}$. Measurements were conducted on 6 different diameters and repeated at various axial positions upstream and downstream the mixing vanes.

A first look at experimental measurements (Figure 6.3) shows that the vanes geometry induces significantly non-symmetric velocity profile. Moreover, we observe high turbulent fluctuations which maximum is located at the same radial position as the maximum radial velocity gradient.

6.2.2 NEPTUNE_CFD simulations of AGATE-Promoteur case

On Figure 6.3, we present some of the results obtained with NEPTUNE_CFD using the $R_{ij} - \varepsilon$ SSG turbulence model on the M2 mesh, along with a smooth wall law and a rough wall law (roughness $\epsilon = 0.01\text{mm}$). The turbulent fluctuations Root Mean Square (RMS) correspond, for instance, to $\sqrt{\langle u_x'^2 \rangle}$ for the x direction where u_i' represents the fluctuating part of the velocity along component i and $\langle \cdot \rangle$ the time-averaging operator. Subscripts R and A stand for radial and axial values ; U_0 is the average inlet velocity.

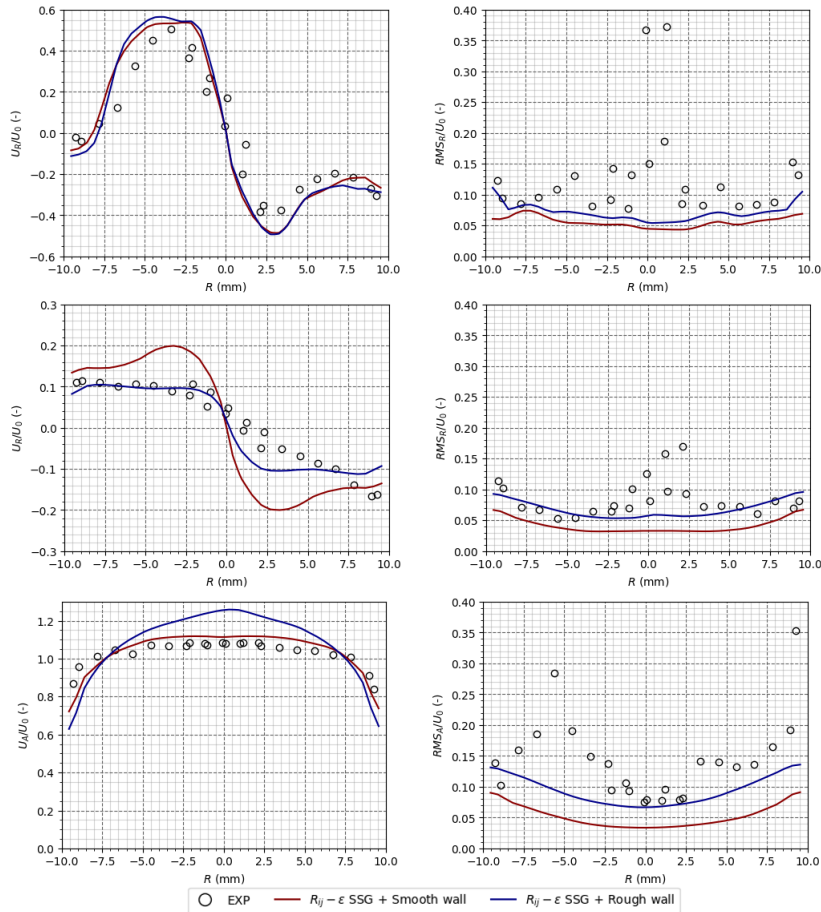


Figure 6.3: NCFD vs. Exp. - Top & Middle : Radial velocity and turbulent RMS ($z = 30\text{mm}$ & $z = 440\text{mm}$) - Bottom : Axial velocity and turbulent RMS ($z = 440\text{mm}$).

Non-symmetric radial velocity profiles close to the MV are quite well reproduced by the simulations. However, far downstream the MV, it appears that the fluid's rotation is overestimated by the model with a smooth wall approach, while applying a roughness helps to reduce the magnitude of the swirl. Moreover, the radial turbulent fluctuations are better estimated by the rough wall approach at $z = 440$ mm. On the other hand, it seems that the rough wall approach deteriorates the axial velocity profile compared to the experiment. As shown on the bottom part of Figure 6.3, the smooth wall simulation returns a flat velocity profile closer to the experiment than the rough wall one which overestimates the core velocity peak.

Both simulations globally underestimate the turbulent fluctuations, which can have a significant influence over the observed discrepancies on velocity profiles since turbulence plays a key role to homogenize the fluid flow.

Those results finally highlight the fact that simulation of such rotating flows may need a particular wall approach to better capture the induced swirl and its dissipation. Correct prediction of turbulent fluctuations would be of significant interest to ensure liquid velocity validation. Further investigations on boiling cases could possibly be improved by a roughness approach, which is the current correction used for two-phase wall laws (Subsection 1.1.6).

Part V
CONCLUSION

Part VI
APPENDIX

A

DETAILS ON THE BUBBLE FORCE BALANCE

Aliquam lectus. Vivamus leo. Quisque ornare tellus ullamcorper nulla. Mauris porttitor pharetra tortor. Sed fringilla justo sed mauris. Mauris tellus. Sed non leo. Nullam elementum, magna in cursus sodales, augue est scelerisque sapien, venenatis congue nulla arcu et pede. Ut suscipit enim vel sapien. Donec congue. Maecenas urna mi, suscipit in, placerat ut, vestibulum ut, massa. Fusce ultrices nulla et nisl. Etiam ac leo a risus tristique nonummy. Donec dignissim tincidunt nulla. Vestibulum rhoncus molestie odio. Sed lobortis, justo et pretium lobortis, mauris turpis condimentum augue, nec ultricies nibh arcu pretium enim. Nunc purus neque, placerat id, imperdiet sed, pellentesque nec, nisl. Vestibulum imperdiet neque non sem accumsan laoreet. In hac habitasse platea dictumst. Etiam condimentum facilisis libero. Suspendisse in elit quis nisl aliquam dapibus. Pellentesque auctor sapien. Sed egestas sapien nec lectus. Pellentesque vel dui vel neque bibendum viverra. Aliquam porttitor nisl nec pede. Proin mattis libero vel turpis. Donec rutrum mauris et libero. Proin euismod porta felis. Nam lobortis, metus quis elementum commodo, nunc lectus elementum mauris, eget vulputate ligula tellus eu neque. Vivamus eu dolor.

$$r_w = \frac{1}{2} (\sin(\theta_d) R + \sin(\theta_u) R) \quad (\text{A.1})$$

$$= \frac{R}{2} (\sin(\theta_s + d\theta) + \sin(\theta - d\theta)) \quad (\text{A.2})$$

$$= \frac{R}{2} \left[2\sin\left(\frac{\theta_s + d\theta + \theta_s - d\theta}{2}\right) \cos\left(\frac{\theta_s + d\theta - (\theta_s - d\theta)}{2}\right) \right] \quad (\text{A.3})$$

$$= R\sin(\theta_s) \cos(d\theta) \quad (\text{A.4})$$

$$\overline{F_{CP}} = \frac{2\sigma}{R_c} \frac{\pi d_w^2}{4} \overline{e_y} \quad (\text{A.5})$$

$$= \frac{2\sigma}{R} \frac{\pi 4R^2}{4} \sin^2(\theta) \cos^2(d\theta) \overline{e_\perp} \quad (\text{A.6})$$

$$= 2\sigma\pi R \underbrace{\sin^2(\theta) \cos^2(d\theta)}_{f_{cp}} \overline{e_\perp} \quad (\text{A.7})$$

$$= 2\pi R\sigma f_{cp}(\theta, d\theta) \overline{e_\perp} \quad (\text{A.8})$$

$$\overline{F_{CP}} \cdot \overline{e_\perp} = -d_w \sigma \frac{\pi}{\alpha_r - \alpha_u} (\cos(\alpha_a) - \cos(\alpha_r)) \quad (A.9)$$

$$= \pi 2R\sigma \frac{\sin(\alpha + d\alpha) + \sin(\alpha - d\alpha)}{2} \frac{\cos(\alpha + d\alpha) - \cos(\alpha - d\alpha)}{2d\alpha} \quad (A.10)$$

$$= 2\pi R\sigma \frac{2\sin(\alpha) \cos(d\alpha)}{2} \frac{(-2\sin(\alpha) \sin(d\alpha))}{2d\alpha} \quad (A.11)$$

$$= -2\pi R\sigma \sin^2(\alpha) \underbrace{\frac{\sin(2d\alpha)}{2d\alpha}}_{f_{s,\perp}} \quad (A.12)$$

$$= -2\pi R\sigma f_{s,\perp}(\alpha, d\alpha) \quad (A.13)$$

(A.14)

$$\overline{F_s} \cdot \overline{e_\parallel} = -1.215 d_w \sigma \frac{\pi(\alpha_r - \alpha_u)}{\pi^2 - (\alpha_r - \alpha_u)^2} (\sin(\alpha_r) + \sin(\alpha_u)) \quad (A.15)$$

$$= -1.215 d_w \sigma \frac{\pi 2d\alpha}{\pi^2 - 4d\alpha^2} (\sin(\alpha + d\alpha) + \sin(\alpha - d\alpha)) \quad (A.16)$$

$$= -1.215 2R\sigma \frac{\pi d\alpha}{\pi^2 - 4d\alpha^2} (\sin(\alpha + d\alpha) + \sin(\alpha - d\alpha))^2 \quad (A.17)$$

$$= -2\pi R\sigma \frac{1.215 d\alpha}{\pi^2 - 4d\alpha^2} 4\sin^2(\alpha) \cos^2(d\alpha) \quad (A.18)$$

$$= -2\pi R\sigma \underbrace{1.215 \frac{d\alpha}{(\frac{\pi}{2})^2 - d\alpha^2} \sin^2(\alpha) \cos^2(d\alpha)}_{f_{s,\parallel}} \quad (A.19)$$

$$= -2\pi R\sigma f_{s,\parallel}(\alpha, d\alpha) \quad (A.20)$$

A.1 APPENDIX SECTION TEST

Nulla in ipsum. Praesent eros nulla, congue vitae, euismod ut, commodo a, wisi. Pellentesque habitant morbi tristique senectus et netus et malesuada fames ac turpis egestas. Aenean nonummy magna non leo. Sed felis erat, ullamcorper in, dictum non, ultricies ut, lectus. Proin vel arcu a odio lobortis euismod. Vestibulum ante ipsum primis in faucibus orci luctus et ultrices posuere cubilia Curae; Proin ut est. Aliquam odio. Pellentesque massa turpis, cursus eu, euismod nec, tempor congue, nulla. Duis viverra gravida mauris. Cras tincidunt. Curabitur eros ligula, varius ut, pulvinar in, cursus faucibus, augue. Nulla mattis luctus nulla. Duis commodo velit at leo. Aliquam vulputate magna et leo. Nam vestibulum ullamcorper leo. Vestibulum condimentum rutrum mauris. Donec id mauris. Morbi molestie justo et pede. Vivamus eget turpis sed nisl cursus tempor. Curabitur mollis sapien condimentum nunc. In wisi nisl, malesuada at, dignissim sit amet, lobortis in, odio. Aenean consequat arcu a ante. Pellentesque porta elit sit amet orci. Etiam at turpis nec elit ultricies imperdiet. Nulla facilisi. In hac habitasse platea dictumst. Suspendisse viverra aliquam risus. Nullam pede justo, molestie nonummy, scelerisque eu, facilisis vel, arcu.

A.2 ANOTHER APPENDIX SECTION TEST

Curabitur tellus magna, porttitor a, commodo a, commodo in, tortor. Donec interdum. Praesent scelerisque. Maecenas posuere sodales odio. Vivamus metus lacus, varius quis, imperdiet quis, rhoncus a, turpis. Etiam ligula arcu, elementum a, venenatis quis, sollicitudin sed, metus. Donec nunc pede, tincidunt in, venenatis vitae, faucibus vel, nibh. Pellentesque wisi. Nullam malesuada. Morbi ut tellus ut pede tincidunt porta. Lorem ipsum dolor sit amet, consectetur adipiscing elit. Etiam congue neque id dolor.

LABITUR BONORUM PRI NO	QUE VISTA	HUMAN
fastidii ea ius	germano	demonstratea
suscipit instructior	titulo	personas
quaestio philosophia	facto	demonstrated

Table A.1: Autem usu id.

Donec et nisl at wisi luctus bibendum. Nam interdum tellus ac libero. Sed sem justo, laoreet vitae, fringilla at, adipiscing ut, nibh. Maecenas non sem quis tortor eleifend fermentum. Etiam id tortor ac mauris porta vulputate. Integer porta neque vitae massa. Maecenas tempus libero a libero posuere dictum. Vestibulum ante ipsum primis in faucibus orci luctus et ultrices posuere cubilia Curae; Aenean quis mauris sed elit commodo placerat. Class aptent taciti sociosqu ad litora torquent per conubia nostra, per inceptos hymenaeos. Vivamus rhoncus tincidunt libero. Etiam elementum pretium justo. Vivamus est. Morbi a tellus eget pede tristique commodo. Nulla nisl. Vestibulum sed nisl eu sapien cursus rutrum. There is also a useless Pascal listing below: [Listing A.1](#).

Listing A.1: A floating example (`listings` manual)

```
1 for i:=maxint downto 0 do
begin
{ do nothing }
end;
```

DECLARATION

Put your declaration here.

Paris, December 2022

Luc Favre

COLOPHON

This document was typeset using the typographical look-and-feel `classicthesis` developed by André Miede. The style was inspired by Robert Bringhurst's seminal book on typography "The Elements of Typographic Style". `classicthesis` is available for both L^AT_EX and L_YX:

<https://bitbucket.org/amiede/classicthesis/>

Happy users of `classicthesis` usually send a real postcard to the author, a collection of postcards received so far is featured here:

<http://postcards.miede.de/>